



UiT The Arctic University of Norway

Faculty of Science and Technology
Department of Mathematics and Statistics

Effects of feedbacks for an energy balance model on a circle

Synne Brynjulfsen

Master's thesis in applied physics and mathematics MAT-3941 06.22

Contents

1 Introduction	3
2 Energy balance model	4
2.1 Thermodynamic assumptions	5
2.2 A circle with continents	6
2.3 Specifications	8
2.3.1 Continents	8
2.3.2 Radiation distribution function S	9
2.3.3 Removing the dimension of temperature	9
2.3.4 Constants	10
2.3.5 Diffusive coefficient	11
3 Boundary formulation solution	12
3.1 Boundary conditions	12
3.2 Fundamental integral identity	14
3.3 Green's function	14
3.4 Integral identity and boundary equations	17
3.5 Segments and important angles	18
3.5.1 Continent edges	19
3.5.2 Ice and snow edges	19
3.6 Solution for one symmetric continent	20
3.7 Bifurcation diagram	24
3.7.1 Situations depending on solar constant Q	24
3.7.2 Branches of solutions	26
4 Pseudo-spectral solution	28
4.1 Finite Fourier transform	29
4.2 Discrete Fourier transform	31
4.3 Implementation	32
5 Finite difference solution	34
5.1 Continent symmetry	36
5.2 Pseudo spectral comparison	36
5.3 Artificial source test	37
6 Stability	38
6.1 One symmetric continent stability	40
7 Effects on bistability	44
7.1 Variation of continent parameters	44
7.1.1 Effects of size	46
7.1.2 Effects of position	47
7.2 Variation of radiation distribution function	49
7.2.1 North approximate shape	50
7.2.2 Effects of function width	51

8 Additional analysis tool AUTO-07p	55
8.1 Implementation	57
8.2 Albedo function sharpness	60
8.3 Stability of multiple snow zones solutions	62
9 Stability and feedback discussion	64
10 Symmetry breaking	66
11 Conclusion	67
A Appendix	70
A.1 Python DFT	70
A.2 Symmetric continent size variation	72
A.3 Continent of set size position variation	77
A.4 Multiple snow zones distribution	81
A.5 Multiple snow zones temperature distributions	84
A.6 Installation and basic use guide for AUTO-07p on Windows	87
A.6.1 Unix-like environment MSYS	87
A.6.2 AUTO file configuration	88
A.6.3 File manipulation	88
A.6.4 Running AUTO	90

1 Introduction

The goal of this thesis, following the project paper “An energy balance model on a circle”, is to investigate aspects of climate models at the lowest rung of the climate model hierarchy. These are the *energy balance models*. Such models were first introduced by Budyko [1] and Sellers [2] in 1969. We will however focus on a type of energy balance model that was introduced by North in 1975 [3, 4]. Characterised by diffusive heat transport, and having only one feedback mechanism, the polar ice sheet. The choice of absorption function also allows the model to be analytically soluble.

The derivation of the model will be based on the lecture notes by Per Kristen Jakobsen [5] [6] [7] [8], in which boundary formulation methods are applied to energy balance models for different domains. Including a circle, the focus of this thesis. Application on a circle gives a further simplified version to North’s spherical model. It is, as ever, important to thoroughly analyse the simpler models of the climate model hierarchy to better understand the more sophisticated, complex models. We also want to investigate how simple we can make the model while still retaining a satisfactory description of the phenomena of interest.

In the project leading up to this thesis a North type energy balance model for a circle was derived, and investigated for the case of no continents. As the model was symmetric, only the upper half circle was considered. For the time dependent case, a pseudo-spectral code based on Fourier modes was implemented, and was validated using artificial sources. For the stationary case, a boundary formulation for two ice edges was derived. Stationary solutions to the energy balance model were then found by solving the boundary equations using analytical and/or numerical methods. Bistability was observed and a bifurcation diagram was constructed. The pseudo-spectral code, along with a finite difference code, was used to test the stationary solutions for stability. As this forms the basis of our work in this thesis, there are several cases of reused derivations from the project paper presented as needed.

The current thesis will build on this and investigate topics that emerge from the introduction of *continents* to the circle model. The continents are given a separate feedback mechanism of a snow edge, adding the snow-albedo feedback to the ice-albedo feedback of the ocean. It is of interest how the introduction, placement and size of the continents influence the bistability of the system. The effects of different incoming radiation will also be considered.

We set out to find the relation between asymmetry in continent placement and dimensions of the bifurcation area. How large would the range of values with several possible states be if situated towards the poles versus the equator? In introducing asymmetry the whole circle must be considered in solving the model. Applying to a symmetric cases, would there exist solutions that break the north south reflection symmetry? In these pursuits, unexpected results led us to down additional paths of inquiry. In varying the incoming radiation function, additional areas of feedback appeared in the form of multiple disjoint snow intervals within one continent. How many intervals can exist depending on the func-

tion? And what are the stability properties of such solutions? Finally, the most important question came from studying the shapes and stability properties of the bifurcation diagram for different continent placements. The most striking feature of the original model is the catastrophic drop into an ice covered planet with a minor decrease in the solar constant. The additional feedback mechanism is tied to the number of possible solutions, and depending on the stability of these solutions, could the magnitude of the plunge be reduced? If there are stable states between the tipping point and the ice planet solution, there could be a more gradual step by step process. Examining this possible link between number of feedbacks and mitigating the temperature steady state drop off will be the focus of this thesis.

In centring the investigation around the bifurcation diagram, we set our focus mostly on stationary solutions. The boundary formulation method will be adapted to the new surfaces and continue to be our main method of solution. Additionally, the continuation and bifurcation software Auto-07p will be used to supplement the bistability analysis. To test the stability of the stationary solutions, a finite difference code for the energy balance model, able to work both with and without continents present, is designed. To validate the implementation we will be using artificial sources, and also compare it to the spectral code for the case of no continents.

2 Energy balance model

To derive our energy balance model, we first consider a general domain D in \mathbb{R}^3 . The model derivation is based on the lecture notes by Per Kristen Jakobsen [5][7]. At some point p at time t we assume three quantities are defined:

$$\begin{aligned} e(p, t) & \text{ energy density} \\ \mathbf{q}(p, t) & \text{ energy flux density} \\ h(p, t) & \text{ energy source density} \end{aligned} \tag{1}$$

For domain D with boundary S and with unit normal \mathbf{n} pointing outwards from D , we define two scalar quantities.

Total energy in D at t , for an infinitesimal element of volume, dV , as

$$E(t) = \int_D dV e(p, t). \tag{2}$$

Total injected/extracted energy to/from D at t as

$$H(t) = \int_D dV h(p, t). \tag{3}$$

And we have a total amount of energy flowing through an infinitesimal element of area, dA , of

$$\mathbf{q}(p, t) \cdot \mathbf{n} dA. \tag{4}$$

From these equations and interpretations, (2), (3) and (4), we have the identity

$$\frac{dE}{dt} = - \int_S dA \mathbf{q}(p, t) \cdot \mathbf{n} + H, \quad (5)$$

which states that the change in total energy in D in time must be equal to the total injected energy into D and energy flowing into D through the surface S, or the opposite. This energy balance law in integral form can be written in differential form using Gauss theorem

$$\begin{aligned} \frac{d}{dt} \int_D dV e(p, t) &= - \int_D dV \nabla \cdot \mathbf{q}(p, t) + \int_D dV h(p, t) \\ &\quad \downarrow \\ \int_D dV \{ \partial_t e(p, t) + \nabla \cdot \mathbf{q}(p, t) - h(p, t) \} &= 0 \end{aligned} \quad (6)$$

And since it is to hold for any domain D we have

$$\partial_t e(p, t) + \nabla \cdot \mathbf{q}(p, t) - h(p, t) = 0, \quad (7)$$

assuming e and h are bounded, and \mathbf{q} is continuously differentiable.

2.1 Thermodynamic assumptions

We will now use some common relations between e, \mathbf{q} and T for our energy balance model. We also introduce expressions relevant for our application in climate science, where we want to model the energy balance for earth or an exoplanet.

We assume the system is in local thermodynamic equilibrium, meaning sufficiently small parts of the system are in equilibrium, and its equation of state in an infinitesimal region around p can then be approximated as

$$e(p, t) = C(p)T(p, t), \quad (8)$$

where $C(p)$ is the heat capacity, and $T(p, t)$ the thermodynamic temperature (in Kelvin).

Since heat flows from high temperature points to low temperature points we have

$$\mathbf{q}(p, t) = -K(p)\nabla T, \quad K(p) > 0 \quad (9)$$

where $K(p)$ is the heat conductive parameter. Heat flows in the opposite direction of positive change in temperature, and the magnitude of the flux depends on the conductivity of the material.

Inserting (8) and (9) into the energy balance model (7), we have

$$C \partial_t T = \nabla \cdot (K \nabla T) + h \quad (10)$$

For our model we will transition to measuring temperature in *Celsius*, which is the most common temperature scale in climate science.

In the application of climate science we can write the source term, h , as

$$h = h_+(1 - a) + h_-, \quad (11)$$

where h_+ is the incident solar radiation, and h_- is thermal (typically heat) radiation outwards, and a is the albedo. The albedo expresses how reflective the material is, as it gives the fraction of incident radiation reflected back.

A simple common albedo model that we will use for our model is

$$a(T) = \begin{cases} a_1(p), & T(p) > -T_s(p) \\ a_2(p), & T(p) < -T_s(p) \end{cases} \quad (12)$$

where $T(p)$ is the temperature in Celsius at point p , and $T_s(p)$ is the absolute value of the temperature for the ice-water phase transition at p , which we know will be negative. $a_1(p)$ is the albedo for water, and $a_2(p)$ for ice.

The loss of energy in outward radiation, described by h_- , happens at some height in the atmosphere where scattering of infrared radiation by gases ends. The higher the height of the layer, the higher the surface temperature is. To model the complex atmospheric processes that determine the height of the layer, we let the amount of infrared radiation that is expelled into space be given as

$$h_- = A(p) + B(p)T(p), \quad A, B > 0, \quad (13)$$

where $T(p)$ is the surface temperature. This is an empirical formula where outgoing radiation is determined by surface temperature. A and B are typically assumed constant. For incoming radiation, described by h_+ , we let

$$h_+ = QS(p), \quad (14)$$

where Q is the solar(earth)/stellar(exoplanet) constant, the absolute size of the radiation, and $S(p)$ describes how solar/stellar radiation is distributed.

Inserting (11), with (12), (13) and (14), into the energy balance model (10) we get

$$C\partial_t T = \nabla \cdot (K\nabla T) - BT + QS(p)(1 - a(T)) - A. \quad (15)$$

This is a highly nonlinear PDE, containing a step function dependent on T . Yet, it is important to note that the model (15) is linear as long as we are not crossing the critical value of $-T_s$. This is a property we will make use of in trying to find an analytic solution of the model.

2.2 A circle with continents

We will be working with a circle as our region, and need to express the energy balance model in appropriate coordinates. A visual representation of the model

is shown in figure [1](#). In general we have the following formulas, using metric coefficients.

The square of the element of length for a chosen set of local coordinates becomes

$$dl^2 = g_{ij}dx_i dx_j \quad (16)$$

where g_{ij} are the metric coefficients of the space, with respect to $\{x_i\}$, the chosen local coordinates (note Einstein summation). We let $\{e_i\}$ be the unit vectors of the local coordinate system, and a basis to the vector fields tangent to the coordinate curves on the surface we are mapping to.

The square matrix of metric coefficients is denoted $\{g_{ij}\}$, its inverse $\{g^{ij}\}$, and the determinant of the matrix $|g|$.

With this, we can express the formulas for the gradient of a scalar function φ as

$$(\nabla\varphi)_i = g^{ij}\partial_{x_j}\varphi, \quad (17)$$

and the divergence of a vector field $\varphi = \varphi_i e_i$ as

$$\nabla \cdot \varphi = \frac{1}{\sqrt{|g|}}\partial_{x_i}(\sqrt{|g|}\varphi_i). \quad (18)$$

We are deriving a model for a circle, that we chose to be of radius R with angle θ , where $\theta = 0$ is the substellar point(closest to the sun). For this circle in the x, z plane we get

$$dl^2 = dx^2 + dz^2 = (-R\sin(\theta)d\theta)^2 + (R\cos(\theta)d\theta)^2 = R^2d\theta^2 \quad (19)$$

And we have a single metric coefficient $g_{\theta\theta} = R^2 \implies |g| = R^2$. We can use [\(17\)](#) and [\(18\)](#) to find an expression for the Laplace Beltrami operator, $\nabla \cdot (K\nabla T)$, on the circle

$$\nabla\varphi(\theta) = \frac{1}{R^2}\partial_\theta\varphi E_\theta = \frac{1}{R}\partial_\theta\varphi e_\theta \quad (20)$$

$$\nabla \cdot \varphi = \frac{1}{R}\partial_\theta(R\varphi_\theta) \quad (21)$$

where $E_\theta = R e_\theta$ is the unnormalized basis vector in θ direction and e_θ is the unit vector in θ direction. Then for a function $\varphi(\theta)$ and constant C we get

$$\nabla \cdot (C\nabla\varphi(\theta)) = \nabla \cdot (C\frac{1}{R}\partial_\theta\varphi e_\theta) = \frac{1}{R}\partial_\theta(C\frac{1}{R}R\partial_\theta\varphi) = \frac{1}{R}\partial_\theta(C\partial_\theta\varphi) \quad (22)$$

Using [\(22\)](#) in the energy balance model [\(15\)](#) we get the one dimensional model for the circle

$$C\partial_t T - \frac{1}{R}\partial_\theta(K\partial_\theta T) + BT = QS(\theta)(1 - a(\theta)) - A. \quad (23)$$

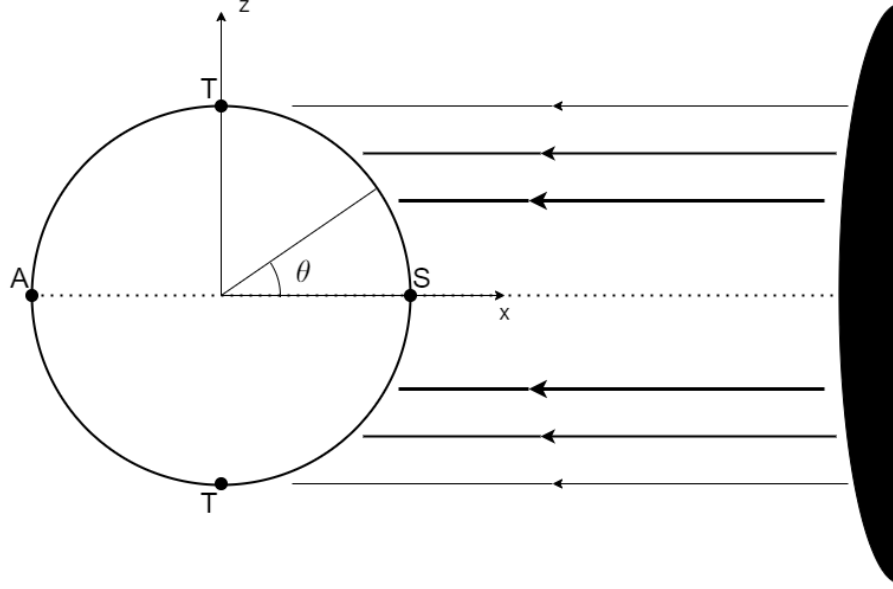


Figure 1: The circle which is the region for the energy balance model, (23). S is the substellar point, A the antistellar point, and T the terminators.

2.3 Specifications

2.3.1 Continents

We will consider the case where there are continents, which entails that the heat conductivity, $K(\theta)$, is not constant over the entire circle. Instead the circle will consist of regions of different heat conductivity. The land mass will have a different conductivity from the ocean, that will depend on geographical factors. Assuming each land region has a constant conductivity, also assumed for the water/ice, we have for a region i

$$K(\theta) = K_i, \quad \text{in region } i \quad (24)$$

Where K_i is a constant value. The ocean region is defined to be region 0, and the subsequent regions 1,2... are different continents. We will also have a different albedo for the continents and ocean, which in the same way will be assumed constant for each continent/ocean. Unlike the ocean, we will not assume transition to ice within the continents, but instead consider a coverage of snow. For this transition the transitional temperature T_s is different, and we will set

$$T_s(\theta) = \begin{cases} T_{s0} = 10^\circ C, & \text{for sea - ice} \\ T_{s1} = 0^\circ C, & \text{for land - snow} \end{cases} \quad (25)$$

giving the new formula for the albedo $a_i(T)$ on the continents

$$a_i(T) = \begin{cases} a_{ci}, & T > 0^\circ C \\ a_S, & T < 0^\circ C \end{cases}, \quad i = 1, 2, \dots \quad (26)$$

where a_{ci} is the albedo for a continent $i=1,2,\dots$, in addition to

$$a_0(T) = \begin{cases} a_W, & T > -10^\circ C \\ a_I, & T < -10^\circ C \end{cases} \quad (27)$$

for the ocean. Consequently, a_W is the water albedo, a_I the ice albedo, and a_S the snow albedo.

The energy balance model for the circle (23) then takes the form

$$C\partial_t T - D_i\partial_{\theta\theta}T + BT = QS(\theta)(1 - a_i(T)) - A, \quad (28)$$

where we have defined the constant $D_i = \frac{K_i}{R}$, the thermal diffusivity, and albedo a_i for each region i .

With the changing diffusive constant D and albedo function for different regions, there is now a discontinuity in the region boundaries. We are not just changing the source term (which is discontinuous within regions at critical temperature as well) but also the rate of diffusion, giving a different operator. This will cause the temperature distribution to not be smooth, as it does not have a continuous derivative across these boundaries.

2.3.2 Radiation distribution function S

Our planet is tidally locked, it does not rotate around its axis, as it is modelled as a circle. It is in essence a 1D line, and it would not make sense to include a higher dimensional component for a simple model.

With this we will use a reflection symmetric radiation distribution function that has decreasing intensity with distance from $\theta = 0$, the substellar point, and no incoming radiation for the half of the sphere around the antistellar point

$$S(\theta) = S(-\theta) \\ S(\theta) = \begin{cases} 1 - \sin\theta, & 0 \leq \theta \leq \pi/2 \\ 0, & \pi/2 \leq \theta \leq \pi \end{cases} \quad (29)$$

This is a type of distribution function that has been used to model tidally locked exoplanets, for instance by Checlair, Menou and Abbot [9]. In reality the incoming radiation from the sun is time dependent, and changes based on the solar cycle among other effects. In our model we use a time averaged constant.

2.3.3 Removing the dimension of temperature

To simplify working with our model we can write it in a spatially dimensionless form. Temperature for the model (28) has the dimension Celsius, and if we let $T_{s0} = 10^\circ C$ be our scale for temperature

$$T = T_{s0}T', \quad (30)$$

where T' is a dimensionless number, we can rewrite the model in terms of T' . For a completely dimensionless form, we would also have to remove the scale for time and use t' , where $t = 1st'$. But since we will mostly be considering the stationary case, where time does not come into play, this will not be of importance.

Dividing (28) by $T_{s0} = 10^\circ C$ and D_i we get for each region

$$\gamma_i \partial_t T' - \partial_{\theta\theta} T' + \beta_i T' = \eta_i S(\theta)(1 - a'_i(T')) - \alpha_i, \quad (31)$$

with scaled parameters

$$\gamma_i = \frac{C}{D_i}, \quad \beta_i = \frac{B}{D_i}, \quad \eta_i = \frac{Q}{D_i T_{s0}}, \quad \alpha_i = \frac{A}{D_i T_{s0}}. \quad (32)$$

The albedo $a_i(T)$ becomes

$$a'_i(T') = \begin{cases} a_{ci}, & T' > 0 \\ a_S, & T' < 0 \end{cases}, \quad i = 1, 2, \dots \quad (33)$$

and

$$a'_0(T') = \begin{cases} a_W, & T' > -1 \\ a_I, & T' < -1 \end{cases} \quad (34)$$

in both cases. For further use of the model, primes will be dropped.

In each region the calculations will be the same, with only a difference of constants between regions.

2.3.4 Constants

We assume constant values for A and B, using the values

$$\begin{aligned} A &= 192.2 \\ B &= 3.85 \end{aligned} \quad (35)$$

We also assume a constant heat capacity $C(\theta) = C$. It will then have the same value for different temperatures, and will be the same for water and ice. We will use

$$C = 13.2 \quad (36)$$

And for the albedo we have

$$\begin{aligned} a_W &= 0.38, \\ a_I &= 0.60, \\ a_S &= 0.60, \\ a_{c1} &= 0.60, \end{aligned} \quad (37)$$

for water, ice, snow, and the first continent respectively.

We will as in North's model we set the critical temperature to be

$$T_{s0} = 10^\circ C, \quad (38)$$

for the water-ice transition. Meaning the water region transitions to ice for temperatures below $-T_{s0}$. And equivalently

$$T_{s1} = 0^\circ C, \quad (39)$$

is chosen for land-snow.

All units are SI units, except temperature.

2.3.5 Diffusive coefficient

As was done by North [3][4], the value for the diffusive coefficient was found empirically by fitting the current ice edge position and solar constant for earth (current for North, value of $\theta = \arcsin 0.95 \approx 1.25$ and $Q = 1338W/m^2$), and best approximated temperature distribution.

North also discussed many ways to calculate different models for the diffusivity [4]. Including having a different diffusivity for the ice and water regions. North considers the possibility that the heat transport by the ocean is suppressed, and proposes that the diffusion can be modelled as

$$D = D_a + D_b h(\theta, \theta_f),$$

$$h(\theta, \theta_f) = \begin{cases} 1, & \theta < \theta_f \\ 0, & \theta > \theta_f \end{cases}, \quad (40)$$

where θ_f is the ice edge, and that in accordance with the fraction of energy carried by the oceans, D_b should be about 30% of the sum ($D_a + D_b$). We then have

$$\begin{aligned} D_{water} &= D_a + D_b & \theta < \theta_f, \\ D_{ice} &= D_a & \theta > \theta_f, \\ D_{ice} &= 0.7 * D_{water}, \end{aligned} \quad (41)$$

We will not assume a different diffusivity for ice and water in this thesis, but we will use this logic for continents. Continents were introduced as having different conductivity, and thus diffusivity, from water. According to Sellers data [2], the main sources of meridional heat transport are ocean currents, water vapour in air, and air currents. And a continent should, depending on the geological factors, suppress these methods of transport to a degree.

For the first continent, with $i = 1$, a desert biome will be assumed. As a desert has similar qualities to arctic regions, being arid and having an extremely barren terrain, it can be assumed to suppress heat transport to the same degree as North reasoned for ice. The values we will use for the constant D_i is then

$$\begin{aligned} D_0 &= 2.11 \\ D_1 &= 0.7 * 2.11 \end{aligned} \quad (42)$$

where D_0 is the diffusivity for the water region, and D_1 for the continent. For additional continents, $i = 2, 3, \dots$, other choices of biomes can be made, and the degree of heat transport suppression could be adjusted according to assessed moisture levels.

3 Boundary formulation solution

The energy balance model (28) is linear as long as we do not cross the constant critical value thresholds given by $T_s(\theta)$, equation (25). We will now take advantage of this fact to actually be able to find analytical solutions to the model. The piece wise linearity makes it very well suited for *boundary formulations*. We thus employ Green's functions and derive the boundary formulation for the case of continents and both ice and snow edges on the water and land sections, respectively, and will focus on finding the **stationary** solutions of the model. In the stationary case

$$\partial_t T = 0, \quad (43)$$

which gives the model

$$-D_i \partial_{\theta\theta} T + BT = QS(\theta)(1 - a_i(T)) - A, \quad (44)$$

and in spatially dimensionless form

$$-\partial_{\theta\theta} T + \beta_i T = \eta_i S(\theta)(1 - a_i(T)) - \alpha_i. \quad (45)$$

We also define

$$h_i(\theta) = \eta_i S(\theta)(1 - a_i(T)) - \alpha_i, \quad (46)$$

with functions and parameters defined in section 2.3. With this, the first step is to derive the fundamental integral identity for L. Then, find a Green's function and its properties. Applying the integral identity using the Green's function and the solution of our boundary value problem, the equation (45) with boundary conditions, we can then get an expression for the solution that relates values of the solution inside the domain to its values on the boundaries.

When we have solved the boundary equations for the stationary solutions we will investigate for bistability, and if present, how the placing of the continents and their size influence the bistability of the system.

3.1 Boundary conditions

Since we have a model for a closed circle, we must have the boundary condition

$$T(\theta) = T(\theta + 2\pi). \quad (47)$$

This condition will always hold for our circular model. To derive the boundary formulation we need to know more values the unknown function takes at said boundaries. We will return briefly to the first basic energy balance law we deduced.

For the stationary case (5) becomes

$$\int_S dA \mathbf{q} \cdot \mathbf{n} = H = \int_V dV h(p, t) \quad (48)$$

For a small surface section S_ϵ we get

$$\lim_{\epsilon \rightarrow 0} \int_{S_\epsilon} dA \mathbf{q} \cdot \mathbf{n} \rightarrow 0 \quad (49)$$

assuming h is smooth and bounded. Applying this around the boundary $\theta = \pm\pi$ for the circle we get, using (9), the condition

$$(\mathbf{q}_+ - \mathbf{q}_-) \cdot \mathbf{n} = (-KT_\theta(\pi)e_\theta + KT_\theta(-\pi)e_\theta) \cdot \mathbf{n} = 0 \quad (50)$$

where \mathbf{q}_+ is the value infinitesimally above the boundary ($+\pi$), and \mathbf{q}_- below, with $\mathbf{n} = -e_\theta$ in this case. The resulting boundary condition is then

$$T_\theta(\pi) = T_\theta(-\pi). \quad (51)$$

Applying at a continent border, θ_{ci} , we also get

$$\begin{aligned} K_+ T_\theta(\theta_{c+}) &= K_- T_\theta(\theta_{c-}) & (V) \\ \Downarrow & & \\ D_+ T_\theta(\theta_{c+}) &= D_- T_\theta(\theta_{c-}) & (V), \end{aligned} \quad (52)$$

where $+$ denotes the value infinitesimally above the boundary, and $-$ below. The derivatives from above and below are then proportional by a constant determined by the difference in the diffusive coefficient D .

For a symmetric surface, either with no continents or with symmetric placement of continents, the equation (45) and the condition of the boundary are both symmetric. It would then be reasonable to be able to restrict to a **symmetric** solution.

$$T(\theta) = T(-\theta) \quad (53)$$

This also gives another condition

$$\begin{aligned} T_\theta(\theta) &= T_\theta(-\theta) \\ \Downarrow & & \\ T_\theta(0) &= -T_\theta(0) & (54) \\ \Downarrow & & \\ T_\theta(0) &= 0 \end{aligned}$$

For the solution to be continuously differentiable at the boundary at least two times, such that we get a classical solution we must also have

$$T_\theta(\pi) = T_\theta(-\pi) = 0 \quad (55)$$

which ensures that $T_\theta(\theta)$ is smooth at the boundary.

Now we can proceed with finding the stationary solution using a boundary formulation.

3.2 Fundamental integral identity

First we derive an integral identity for $L_i = -\partial_{\theta\theta} + \beta_i$ on the interval $[\theta_0, \theta_1]$. For the derivation we drop the i subscript, the process is the same for all sections. Letting ϕ and ψ be smooth functions defined on the interval, and using integration by parts we have

$$\begin{aligned} \int_{\theta_0}^{\theta_1} d\theta L\phi\psi &= \int_{\theta_0}^{\theta_1} d\theta(-\phi_{\theta\theta} + \beta\phi)\psi \\ &= -\phi_{\theta}\psi|_{\theta_0}^{\theta_1} + \int_{\theta_0}^{\theta_1} d\theta\phi_{\theta}\psi_{\theta} + \int_{\theta_0}^{\theta_1} d\theta\beta\phi\psi \\ &= -\phi_{\theta}\psi|_{\theta_0}^{\theta_1} + \left(\phi\psi_{\theta}|_{\theta_0}^{\theta_1} - \int_{\theta_0}^{\theta_1} d\theta\phi\psi_{\theta\theta}\right) + \int_{\theta_0}^{\theta_1} d\theta\beta\phi\psi, \end{aligned} \quad (56)$$

which gives the integral identity

$$\int_{\theta_0}^{\theta_1} d\theta\{L\phi\psi - \phi L\psi\} = (\phi\psi_{\theta} - \phi_{\theta}\psi)|_{\theta_0}^{\theta_1}. \quad (57)$$

3.3 Green's function

A Green's function for L , is a function that satisfies

$$LK(p, \xi) = \delta_{\xi}(p) \quad (58)$$

for a point p , where $\delta_{\xi}(p)$ is the delta function at point ξ . The Dirac delta function is defined in such a way that

$$\int_C dl \delta_{\xi} = 1 \quad (59)$$

if $\xi \in C$, else wise the integral is 0. In polar coordinates we get

$$\int_{-\pi}^{\pi} d\theta R\delta_{\xi}(\theta) = 1 \quad (60)$$

In terms of the standard Dirac delta in 1D this Dirac delta is

$$\delta_{\xi}(\theta) = \frac{1}{R}\delta(\theta - \xi). \quad (61)$$

Since it is dependent on R it is a dimensional quantity, and we have to find the Green's function for the dimensional form of the energy balance equation for the stationary case [\(44\)](#). A Green's function $K(\theta, \xi)$ for the dimensional $\mathcal{L} = -D\partial_{\theta\theta} + B$ satisfies

$$\begin{aligned} -D\partial_{\theta\theta}K(\theta, \xi) + BK(\theta, \xi) &= \delta_{\xi}(\theta) \\ \Downarrow \\ -DK_{\theta\theta}(\theta, \xi) + BK(\theta, \xi) &= \frac{1}{R}\delta(\theta - \xi) \end{aligned} \quad (62)$$

Letting \bar{K} be the dimension of the Green's function we can express the dimensionless form with K' , $K = \bar{K}K'$ as

$$-K'_{\theta\theta}(\theta, \xi) + \beta K'(\theta, \xi) = \gamma \delta(\theta - \xi) \quad (63)$$

with dimensionless parameters

$$\beta = \frac{BR^2}{K_0}, \quad \gamma = \frac{R}{K_0\bar{K}}, \quad (64)$$

we can choose a Green's function such that $\gamma = 1 \Rightarrow \bar{K} = R/K_0$. And dropping the prime the dimensionless Green's function solves

$$\mathcal{L}K(\theta, \xi) = -K_{\theta\theta}(\theta, \xi) + \beta K(\theta, \xi) = \delta(\theta - \xi) \quad (65)$$

From the properties of the Dirac delta function, for $\theta \neq \xi$ we have the equation

$$-K_{\theta\theta}(\theta, \xi) + \beta K(\theta, \xi) = 0, \quad \theta \neq \xi \quad (66)$$

Integrating over a small interval $I_\epsilon = (\xi - \epsilon, \xi + \epsilon)$

$$\begin{aligned} \int_{\xi-\epsilon}^{\xi+\epsilon} d\theta \{-K_{\theta\theta}(\theta, \xi) + \beta K(\theta, \xi)\} &= \int_{\xi-\epsilon}^{\xi+\epsilon} d\theta \delta(\theta - \xi) = 1 \\ &\Downarrow \\ -K_\theta(\xi + \epsilon, \xi) + K_\theta(\xi - \epsilon, \xi) + \int_{\xi-\epsilon}^{\xi+\epsilon} d\theta \beta K(\theta, \xi) &= 1 \end{aligned} \quad (67)$$

The delta function integrating to 1 holds because it is concentrated infinitesimally close to $x = \xi$. Taking the limit when $\epsilon \rightarrow 0$ we get

$$K_\theta^+(\xi, \xi) - K_\theta^-(\xi, \xi) = -1 \quad (68)$$

assuming $K(x; \xi)$ is continuous in θ and ξ , where

$$K_\theta^{+/-}(\xi; \xi) = \lim_{\epsilon \rightarrow 0} K_\theta(\xi \pm \epsilon; \xi) \quad (69)$$

and since we postulate that $K(x; \xi)$ is continuous at $\theta = \xi$ we also have

$$K^+(\xi; \xi) - K^-(\xi; \xi) = 0. \quad (70)$$

Solving the equation (66) we find the general solution

$$K(\theta, \xi) = \begin{cases} a(\xi) \cosh(\sqrt{\beta}\theta) + b(\xi) \sinh(\sqrt{\beta}\theta), & \theta > \xi \\ c(\xi) \cosh(\sqrt{\beta}\theta) + d(\xi) \sinh(\sqrt{\beta}\theta), & \theta < \xi \end{cases} \quad (71)$$

as $\theta \neq \xi$, and it can have different solutions on either side. Applying (68) and (70)

$$\begin{aligned}
& a(\xi) \sinh(\sqrt{\beta}\xi) + b(\xi) \cosh(\sqrt{\beta}\xi) \\
& -c(\xi) \sinh(\sqrt{\beta}\xi) - d(\xi) \cosh(\sqrt{\beta}\xi) = -\frac{1}{\sqrt{\beta}} \\
& a(\xi) \cosh(\sqrt{\beta}\xi) + b(\xi) \sinh(\sqrt{\beta}\xi) \\
& -c(\xi) \cosh(\sqrt{\beta}\xi) - d(\xi) \sinh(\sqrt{\beta}\xi) = 0 \tag{72} \\
& \quad \Downarrow \\
& c(\xi) = a(\xi) - \frac{1}{\sqrt{\beta}} \sinh(\sqrt{\beta}\xi) \\
& d(\xi) = b(\xi) + \frac{1}{\sqrt{\beta}} \cosh(\sqrt{\beta}\xi)
\end{aligned}$$

which gives

$$K(\theta, \xi) = \begin{cases} a(\xi) \cosh(\sqrt{\beta}\theta) + b(\xi) \sinh(\sqrt{\beta}\theta), & \theta > \xi \\ a(\xi) \cosh(\sqrt{\beta}\theta) - \frac{1}{\sqrt{\beta}} \sinh(\sqrt{\beta}\xi) \cosh(\sqrt{\beta}\theta) \\ + b(\xi) \sinh(\sqrt{\beta}\theta) + \frac{1}{\sqrt{\beta}} \cosh(\sqrt{\beta}\xi) \sinh(\sqrt{\beta}\theta), & \theta < \xi \end{cases} \tag{73}$$

Using the identity

$$\sinh(x + y) = \sinh(x) \cosh(y) + \cosh(x) \sinh(y) \tag{74}$$

we have

$$K(\theta, \xi) = \begin{cases} a(\xi) \cosh(\sqrt{\beta}\theta) + b(\xi) \sinh(\sqrt{\beta}\theta), & \theta > \xi \\ a(\xi) \cosh(\sqrt{\beta}\theta) + b(\xi) \sinh(\sqrt{\beta}\theta) + \frac{1}{\sqrt{\beta}} \sinh(\sqrt{\beta}(\theta - \xi)), & \theta < \xi \end{cases} \tag{75}$$

where $a(\xi)$ and $b(\xi)$ are arbitrary. With this it makes sense to choose

$$\begin{aligned}
a(\xi) &= -\frac{1}{2\sqrt{\beta}} \sinh(-\sqrt{\beta}\xi) \\
b(\xi) &= -\frac{1}{2\sqrt{\beta}} \cosh(-\sqrt{\beta}\xi) \tag{76}
\end{aligned}$$

which by applying (74) again means

$$\begin{aligned}
& -\frac{1}{2\sqrt{\beta}} \sinh(\sqrt{\beta}(\theta - \xi)), & \theta > \xi \\
-\frac{1}{2\sqrt{\beta}} \sinh(\sqrt{\beta}(\theta - \xi)) + \frac{1}{\sqrt{\beta}} \sinh(\sqrt{\beta}(\theta - \xi)), & \theta < \xi \\
& \Downarrow \\
& -\frac{1}{2\sqrt{\beta}} \sinh(\sqrt{\beta}(\theta - \xi)), & \theta > \xi \\
& \frac{1}{2\sqrt{\beta}} \sinh(\sqrt{\beta}(\theta - \xi)), & \theta < \xi
\end{aligned} \tag{77}$$

and finally we have the Green's function

$$K(\theta, \xi) = \begin{cases} -\frac{1}{2\sqrt{\beta}} \sinh(\sqrt{\beta}(\theta - \xi)), & \theta > \xi \\ \frac{1}{2\sqrt{\beta}} \sinh(\sqrt{\beta}(\theta - \xi)), & \theta < \xi \end{cases}. \tag{78}$$

Inserting the section dependent constants again it becomes

$$K_i(\theta, \xi) = \begin{cases} -\frac{1}{2\sqrt{\beta_i}} \sinh(\sqrt{\beta_i}(\theta - \xi)), & \theta > \xi \\ \frac{1}{2\sqrt{\beta_i}} \sinh(\sqrt{\beta_i}(\theta - \xi)), & \theta < \xi \end{cases}. \tag{79}$$

The Green's function is dependent on β_i , and is thus different for each region, but the difference is only in scaling.

3.4 Integral identity and boundary equations

We now apply the integral identity using a Green's function for L and the solution of the boundary value problem. Inserting $\psi = T(\theta)$ and $\phi = K_i(\theta, \xi)$ into (57) and using $L_i T = h_i(\theta)$ gives

$$\begin{aligned}
& \int_{\theta_0}^{\theta_1} d\theta \{L_i K_i(\theta, \xi) T(\theta) - K_i(\theta, \xi) h_i(\theta)\} \\
& = (K_i(\theta, \xi) T_\theta(\theta) - K_{i\theta}(\theta, \xi) T(\theta))|_{\theta_0}^{\theta_1},
\end{aligned} \tag{80}$$

and using that $K_i(\theta, \xi)$ is a Green's function for L_i we have

$$\begin{aligned}
& \int_{\theta_0}^{\theta_1} d\theta \{\delta(\theta - \xi) T(\theta) - K_i(\theta, \xi) h_i(\theta)\} \\
& = (K_i(\theta, \xi) T_\theta(\theta) - K_{i\theta}(\theta, \xi) T(\theta))|_{\theta_0}^{\theta_1} \\
& \Downarrow \\
T(\xi) & = \int_{\theta_0}^{\theta_1} d\theta K_i(\theta, \xi) h_i(\theta) + (K_i(\theta, \xi) T_\theta(\theta) - K_{i\theta}(\theta, \xi) T(\theta))|_{\theta_0}^{\theta_1},
\end{aligned} \tag{81}$$

If we let ξ approach the boundaries at $[\theta_0, \theta_1]$ we get expressions for the boundary values $T(\theta_0)$ and $T(\theta_1)$.

$\xi \rightarrow \theta_0$

$$T(\theta_0) = \int_{\theta_0}^{\theta_1} d\theta K_i^+(\theta, \theta_0) h_i(\theta) + K_i(\theta_1, \theta_0) T_\theta(\theta_1) - K_{i\theta}(\theta_1, \theta_0) T(\theta_1) - K_i^-(\theta_0, \theta_0) T_\theta(\theta_0) + K_{i\theta}^-(\theta_0, \theta_0) T(\theta_0) \quad (82)$$

$\xi \rightarrow \theta_1$

$$T(\theta_1) = \int_{\theta_0}^{\theta_1} d\theta K_i^-(\theta, \theta_1) h_i(\theta) + K_i^+(\theta_1, \theta_1) T_\theta(\theta_1) - K_{i\theta}^+(\theta_1, \theta_1) T(\theta_1) - K_i(\theta_0, \theta_1) T_\theta(\theta_0) + K_{i\theta}(\theta_0, \theta_1) T(\theta_0) \quad (83)$$

With these equations we have just derived we can find the solutions $T(\xi)$ for different intervals $[\theta_0, \theta_1]$ using known values for $T(\theta)$, $T_\theta(\theta)$ and the Green's function.

The two equations (82) and (83) are the general forms of the **boundary equations** we can get for each segment of curve $C_j = [\theta_0, \theta_1]$, $j = 0, 1, 2, \dots$ where the model is linear. We get two equations for each segment, which are used to solve for the unknown values.

The equation (81) is the general **integral identity**, which can be used to find the solution, $T(\xi)$, for each segment of curve C_j by inserting the solutions of the boundary equations.

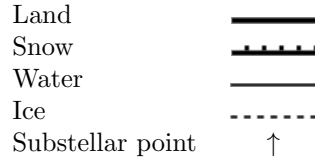
Combining the solutions for the different segments gives the total solution temperature distribution.

3.5 Segments and important angles

We must split the circle into intervals with constant values for albedo a and diffusivity D in order to solve the boundary formulations for T , and combine the intervals to find the total solution.

When we have symmetry we only consider the interval $[0, \pi]$ only, as we assume a symmetric solution around $\pi = 0$. Without continents, which is naturally symmetric, we only have to split into a **water interval** and an **ice interval**. With the introduction of one continent, there are 4 intervals to consider if we still have symmetry, and 8 without. The four being **land, snow, water, ice** for one half-circle, and 8 being the doubled amount for the whole circle. It should also be possible to have several disjoint intervals of snow and ice depending on the circumstances.

To more easily grasp the situations we introduce the following representations for the areas



The split into different segments happens at two different types of *important angles*. For any given case, the number of segments C_j is decided by the number of these angles. The first type of important angles is the continent edge positions, of which we get two additional for every continent included. The second, and most important for the calculations, is the positions at the critical phase transitional temperature (25).

3.5.1 Continent edges

We must split into different intervals for the different regions i where the constants change values. The *edges of the continents*, which will be labeled $\theta_{cib}, \theta_{cia}$ for continent i , are non-continuous points with temperature values that are unknown. The edges however are known, as we choose the placements of the continents.

For a continent spanning interval $[\theta_{cib}, \theta_{cia}]$ within an ocean interval $[\theta_0, \theta_1]$ we would get the three segments of curve C_j

$$\begin{aligned}
 C_0 &= [\theta_0, \theta_{cib}], \\
 C_1 &= [\theta_{cib}, \theta_{cia}], \\
 C_2 &= [\theta_{cia}, \theta_1].
 \end{aligned}
 \tag{84}$$



to consider. For each region the constants are different, we have to insert the i value of the region into the equations (82), (83) and (81) when solving. For these C_j we would have $i=0$ for C_0 and C_2 , and $i=1, 2, \dots$ for C_1 depending on the continent. We find the boundary equations for each interval, the segments (84) yielding 6 equations in total.

3.5.2 Ice and snow edges

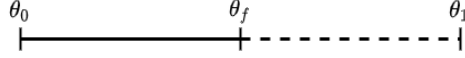
We must also consider the situation with ice edges and snow edges within the ocean regions and land regions respectively. The positions of the *ice and snow edges* are determined by the critical temperatures for phase transition, and are unknowns.

With an ice edge, denoted θ_f , within the ocean interval, $\theta_f \in [\theta_0, \theta_1]$, there are two intervals to consider. They will have different $h_0(\theta)$ functions because of the different albedos from $a(T)$. As the ice edge position is determined by

$$T(\theta_f) = -1, \tag{85}$$

we have this as a known boundary value, but the angle θ_f itself is unknown. Within the ocean interval we would get the segments of curve

$$\begin{aligned} C_0 &= [\theta_0, \theta_f], \\ C_1 &= [\theta_f, \theta_1]. \end{aligned} \tag{86}$$

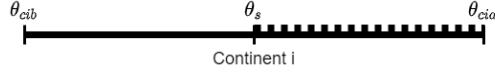


Equivalently, we have for a snow edge, denoted θ_s , within a continent, $\theta_s \in [\theta_{cib}, \theta_{cia}]$, two intervals with different $h_i(\theta)$, $i=1,2,\dots$, functions. We have known boundary value

$$T(\theta_s) = 0, \tag{87}$$

where the angle θ_s is unknown. Within the continent interval we would get the segments of curve C_j

$$\begin{aligned} C_0 &= [\theta_{cib}, \theta_s], \\ C_1 &= [\theta_s, \theta_{cia}]. \end{aligned} \tag{88}$$



Depending on the situation and planet surface we are considering we can have one or several edges within a continent or ocean interval.

Since the angles θ_f and θ_s are unknown, and the equations (82), (83) and (81) depend on them in non-linear ways, solving for them is *much harder* than solving for unknown values of $T(\theta)$ and $T_\theta(\theta)$. The more of these critical temperature positions we have, the more segments we will have to split the circle into, and the harder it will be to solve the resulting system.

3.6 Solution for one symmetric continent

With one continent which is centred around $\pi = 0$, meaning we have symmetry, and considering the case where we have one ice edge and one snow edge, we get 4 intervals on the upper half circle. Since there is only one continent, and we have symmetry, we denote the position of the continent edge simply as θ_c . Subscript $i = 1$ for land/snow and $i = 0$ for water/ice is dropped to reduce clutter.

We apply (81) for $\theta_s \in [0, \theta_c]$, $\theta_f \in [\theta_c, \pi]$, and using the conditions (52), (54), (55) and (85), (87) we get

Land interval $[0, \theta_s]$, with $h_l(\theta) = h_1(\theta)$ where $a(T) = a_{c1}$

$$T(\xi) = \int_0^{\theta_s} d\theta K(\theta, \xi) h_l(\theta) + K(\theta_s, \xi) T_\theta(\theta_s) - K_\theta(\theta_s, \xi) T(\theta_s) - K(0, \xi) T_\theta(0) + K_\theta(0, \xi) T(0)$$

$$\Downarrow$$

$$T(\xi) = \int_0^{\theta_s} d\theta K(\theta, \xi) h_l(\theta) + K(\theta_s, \xi) T_\theta(\theta_s) + K_\theta(0, \xi) T(0)$$

$\xi \rightarrow 0$

$$T(0) = \int_0^{\theta_s} d\theta K(\theta, 0) h_l(\theta) + K(\theta_s, 0) T_\theta(\theta_s) + K_\theta^-(0, 0) T(0)$$

$\xi \rightarrow \theta_s$

$$T(\theta_s) = 0 = \int_0^{\theta_s} d\theta K(\theta, \theta_s) h_l(\theta) + K^+(\theta_s, \theta_s) T_\theta(\theta_s) + K_\theta(0, \theta_s) T(0)$$

Snow interval $[\theta_s, \theta_c]$, with $h_s(\theta) = h_1(\theta)$ where $a(T) = a_s$

$$T(\xi) = \int_{\theta_s}^{\theta_c} d\theta K(\theta, \xi) h_s(\theta) + K(\theta_c, \xi) T_\theta(\theta_c) - K_\theta(\theta_c, \xi) T(\theta_c) - K(\theta_s, \xi) T_\theta(\theta_s) + K_\theta(\theta_s, \xi) T(\theta_s)$$

$$\Downarrow$$

$$T(\xi) = \int_{\theta_s}^{\theta_c} d\theta K(\theta, \xi) h_s(\theta) + K(\theta_c, \xi) T_\theta(\theta_c) - K_\theta(\theta_c, \xi) T(\theta_c) - K(\theta_s, \xi) T_\theta(\theta_s)$$

$\xi \rightarrow \theta_s$

$$T(\theta_s) = 0 = \int_{\theta_s}^{\theta_c} d\theta K(\theta, \theta_s) h_s(\theta) + K(\theta_c, \theta_s) T_\theta(\theta_c) - K_\theta(\theta_c, \theta_s) T(\theta_c) - K^-(\theta_s, \theta_s) T_\theta(\theta_s)$$

$\xi \rightarrow \theta_c$

$$T(\theta_c) = \int_{\theta_s}^{\theta_c} d\theta K(\theta, \theta_c) h_s(\theta) + K^+(\theta_c, \theta_c) T_\theta(\theta_c) - K_\theta^+(\theta_c, \theta_c) T(\theta_c) - K(\theta_s, \theta_c) T_\theta(\theta_s)$$

Water interval $[\theta_c, \theta_f]$, with $h_w(\theta) = h_0(\theta)$ where $a(T) = a_w$

$$T(\xi) = \int_{\theta_c}^{\theta_f} d\theta K(\theta, \xi) h_w(\theta) + K(\theta_f, \xi) T_\theta(\theta_f) - K_\theta(\theta_f, \xi) T(\theta_f) - K(\theta_c, \xi) T_\theta(\theta_c) + K_\theta(\theta_c, \xi) T(\theta_c)$$

$\xi \rightarrow \theta_c$

$$T(\theta_c) = \int_{\theta_c}^{\theta_f} d\theta K(\theta, \theta_c) h_w(\theta) + K(\theta_f, \theta_c) T_\theta(\theta_f) + K_\theta(\theta_f, \theta_c) - K^-(\theta_c, \theta_c) T_\theta(\theta_c) + K_\theta^-(\theta_c, \theta_c) T(\theta_c) \quad (96)$$

$\xi \rightarrow \theta_f$

$$T(\theta_f) = -1 = \int_{\theta_c}^{\theta_f} d\theta K(\theta, \theta_f) h_w(\theta) + K^+(\theta_f, \theta_f) T_\theta(\theta_f) + K_\theta^+(\theta_f, \theta_f) - K(\theta_c, \theta_f) T_\theta(\theta_c) + K_\theta(\theta_c, \theta_f) T(\theta_c) \quad (97)$$

Ice interval $[\theta_f, \pi]$, with $h_i(\theta) = h_0(\theta)$ where $a(T) = a_i$

$$T(\xi) = \int_{\theta_f}^{\pi} d\theta K(\theta, \xi) h_i(\theta) + K(\pi, \xi) T_\theta(\pi) - K_\theta(\pi, \xi) T(\pi) - K(\theta_f, \xi) T_\theta(\theta_f) + K_\theta(\theta_f, \xi) T(\theta_f) \quad (98)$$

\Downarrow

$$T(\xi) = \int_{\theta_f}^{\pi} d\theta K(\theta, \xi) h_i(\theta) - K_\theta(\pi, \xi) T(\pi) - K(\theta_f, \xi) T_\theta(\theta_f) - K_\theta(\theta_f, \xi)$$

$\xi \rightarrow \theta_f$

$$T(\theta_f) = -1 = \int_{\theta_f}^{\pi} d\theta K(\theta, \theta_f) h_i(\theta) - K_\theta(\pi, \theta_f) T(\pi) - K^-(\theta_f, \theta_f) T_\theta(\theta_f) - K_\theta^-(\theta_f, \theta_f) \quad (99)$$

$\xi \rightarrow \pi$

$$T(\pi) = \int_{\theta_f}^{\pi} d\theta K(\theta, \pi) h_i(\theta) - K_\theta^+(\pi, \pi) T(\pi) - K(\theta_f, \pi) T_\theta(\theta_f) - K_\theta(\theta_f, \pi) \quad (100)$$

This gives 8 equations, (90), (91), (93), (94), (96), (97), (99) and (100), for the 8 unknowns $T(0)$, $T(\pi)$, $T_\theta(\theta_f)$, θ_f , $T(\theta_c)$, $T_\theta(\theta_c)$, $T_\theta(\theta_s)$ and θ_s . The situation can be represented visually as



Using the reasoning for the condition (54) $T_\theta(\theta_f)$ and $T_\theta(\theta_s)$ are the same approaching from both sides (adjacent intervals), while the condition on $T_\theta(\theta_c)$ is given by (52). For all Green's functions evaluated at the boundaries, the upper boundary has $\theta > \xi$ and takes the corresponding value from the formula (79) and equivalently the lower boundary has $\theta < \xi$. The integrals over the segments are split around the undefined value at ξ

$$\int_{-l}^u = \int_{-l}^\xi + \int_\xi^u. \quad (101)$$

where u and l are the upper and lower boundaries.

As the eight boundary equations are non-linear in θ_s and θ_f , but linear in the other unknown values of $T(\theta)$ and $T_\theta(\theta)$, we first express the other unknowns in terms of θ_s and θ_f . Substituting these into two of the equations we are reduced to a system of two equations we must solve for θ_s and θ_f on the form

$$\begin{aligned} F(\theta_s, \theta_f) &= 0, \\ G(\theta_s, \theta_f) &= 0, \end{aligned} \quad (102)$$

which is then solved for θ_s and θ_f for a given solar/stellar constant Q . To get a solution we must first set the size of the continent, determined by the position of θ_c . As a default value we choose

$$\theta_c = \frac{\pi}{8}, \quad (103)$$

which gives a continent of size $l = \pi/4$, symmetric around $\pi = 0$.

Solving for the unknowns and using (89), (92), (95) and (98) we get solutions for $T(\xi)$ each interval, which together gives the temperature distribution for the upper half-circle.

Mathematica was used to analytically solve the 8 equations for the 6 unknowns $T(0)$, $T(\pi)$, $T_\theta(\theta_f)$, $T(\theta_c)$, $T_\theta(\theta_c)$ and $T_\theta(\theta_s)$, then substitute into two equations for a system (102), which could then be solved for θ_s and θ_f for a given Q . While it could be possible to solve (102) analytically, it becomes very complex and time consuming. At a situation with one edge, θ_s or θ_f , it is feasible, but at two edges and above it must be solved numerically.

The system (102) solved for the value $Q = 800$ is shown in figure 2

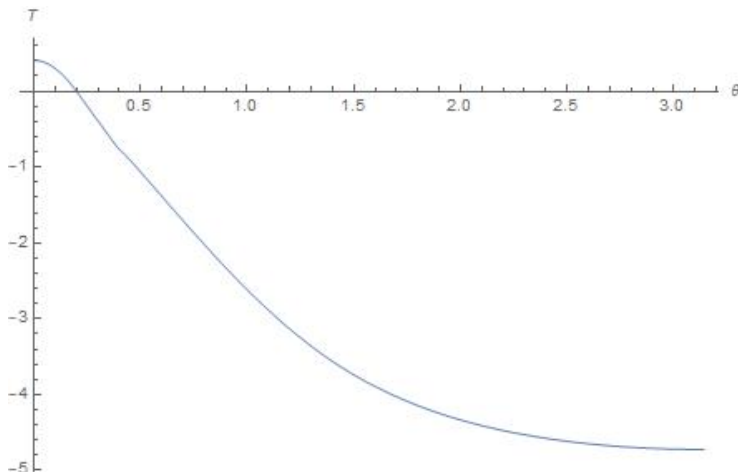


Figure 2: The temperature distribution for $Q = 800$.

3.7 Bifurcation diagram

Now we will consider how the solution changes for different values of Q . Depending on the value, the planet will get hotter or colder and the situation will change accordingly.

We derived the boundary formulation for the case of an ice edge and a snow edge on the upper half circle, and symmetry around $\pi = 0$, but for certain values of Q it will be too warm for a ice/snow edge to exist. Whether it is the snow or ice that disappears first depends on the parameters. There will also be values of Q where it will be warm enough that neither edge can exist, or cold enough that the whole planet is covered in ice and snow. Short hand notation **L** = **Land**, **S** = **Snow**, **W** = **Water**, **I** = **Ice** will be used to show the order of areas for these situations.

Generally, the temperature $T(\theta)$ decreases from the substellar point towards the antistellar point, and we expect

$$T(\pi) < T(\theta) < T(0) \quad \forall \theta \in (0, \pi). \quad (104)$$

This was already assumed for the area distribution of the previous solution. We can then find the values of Q that determine the transitions to these different situations as follows.

3.7.1 Situations depending on solar constant Q

For the **waterworld**, and **snowball** situations we can assume that the lowest Q that gives a waterworld, $T(\theta) \geq 0 \quad \forall \theta \in (0, \theta_c)$ and $T(\theta) \geq -1 \quad \forall \theta \in (\theta_c, \pi)$, is the solution where

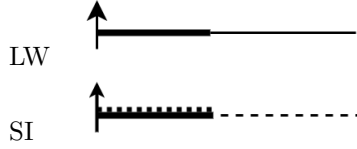
$$T(\pi) = -1, \quad (105)$$

and the highest Q that gives a snowball, $T(\theta) < 0 \quad \forall \theta \in (0, \theta_c)$ and $T(\theta) < -1 \quad \forall \theta \in (\theta_c, \pi)$, is the solution where either

$$T(0) = 0, T(\theta_c) < -1 \quad \text{or} \quad T(\theta_c) = -1, T(0) < 0. \quad (106)$$

We find the boundary equations for the segments

$$\begin{aligned} C_0 &= [0, \theta_c], & a_1(T) &= a_{c1}/a_s, \\ C_1 &= [\theta_c, \pi], & a_0(T) &= a_w/a_i, \end{aligned} \quad (107)$$



by using the general expressions (82) and (83), with the appropriate albedo values. Then we solve for the values of Q using *Mathematica*. The waterworld value will be denoted Q_w , and the snowball value Q_i .

Other possible situations that follow from assumption (104) is the **ice cap** situation, $T(\theta) \geq 0 \quad \forall \theta \in (0, \theta_c)$ and $T(\pi) < -1$, with boundary equations for segments and constant albedos

$$\begin{aligned} C_0 &= [0, \theta_c], & a_1(T) &= a_{c1}, \\ C_1 &= [\theta_c, \theta_f], & a_0(T) &= a_w, \\ C_2 &= [\theta_f, \pi], & a_0(T) &= a_i, \end{aligned} \quad (108)$$



the **ice cover** situation, $T(\theta) < -1 \quad \forall \theta \in (\theta_c, \pi)$ and $T(0) \geq 0$, with boundary equations for segments and constant albedos

$$\begin{aligned} C_0 &= [0, \theta_s], & a_1(T) &= a_{c1}, \\ C_1 &= [\theta_s, \theta_c], & a_1(T) &= a_s, \\ C_2 &= [\theta_c, \pi], & a_0(T) &= a_i, \end{aligned} \quad (109)$$



and the **snow cover** situation, $T(\theta) < 0 \quad \forall \theta \in (0, \theta_c)$ and $T(\theta_c) \geq -1$, with boundary equations for segments and constant albedos

$$\begin{aligned} C_0 &= [0, \theta_c], & a_1(T) &= a_s, \\ C_1 &= [\theta_c, \theta_f], & a_0(T) &= a_w, \\ C_2 &= [\theta_f, \pi], & a_0(T) &= a_i. \end{aligned} \quad (110)$$



For these situations we will, by the same process as with two angles, reduce the equations, but now down to a single function on the form

$$F(\theta_s/\theta_f) = 0. \quad (111)$$

Solving for each situation we can investigate which values of Q there exists a solution, and with this we can find possible bifurcations.

3.7.2 Branches of solutions

Analysing the areas with solutions for the different situations, we find several overlaps. One value of Q can therefore correspond to several different solution branches in these areas of overlap, and we have a bifurcation. Figure 4 shows a representation of the different situations.

For our chosen constants, we get for the **waterworld** and **snowball** boundaries

$$\begin{aligned} Q_w &\approx 11593.9, \\ Q_i &\approx 1083.28. \end{aligned} \quad (112)$$

where $T(\theta_c) = -1, T(0) < 0$ was the limiting case for Q_i . By investigating the system for θ_s and θ_f (102) it was found that there is *one solution* for

$$Q_a < Q < Q_b, \quad (113)$$

where

$$\begin{aligned} Q_a &\approx 734.29, \\ Q_b &\approx 1073.54. \end{aligned} \quad (114)$$

For the **ice cap** situation the θ_f function on the form (111) had *one solution* for

$$Q_a < Q < Q_w. \quad (115)$$

For the **ice cover** situation the θ_s function on the form (111) had *no solutions*. And finally for the **snow cover** situation the θ_f function on the form (111) had *two solutions* for

$$Q_c < Q < Q_b, \quad (116)$$

and *one solution* for

$$Q_b < Q < Q_i, \quad (117)$$

else wise *no solutions*. The value Q_c is the point where the solution curve folds. To find an explicit value for Q_c , we can use the fact that in this point we must have

$$F(\theta_f) = 0, \quad F'(\theta_f) = 0. \quad (118)$$

Using this we can solve for Q_c and θ_f , and the resulting value was found to be

$$Q_c \approx 1058.04. \quad (119)$$

These results are condensed in the bifurcation diagram in figure 3, plotted in *Mathematica*, which shows the temperature $T(0)$ at the substellar point as a function of the solar/stellar constant Q . The temperature $T(0)$ continues to increase/decrease with increasing/decreasing Q with a steady rate outside the interval shown in the graph.

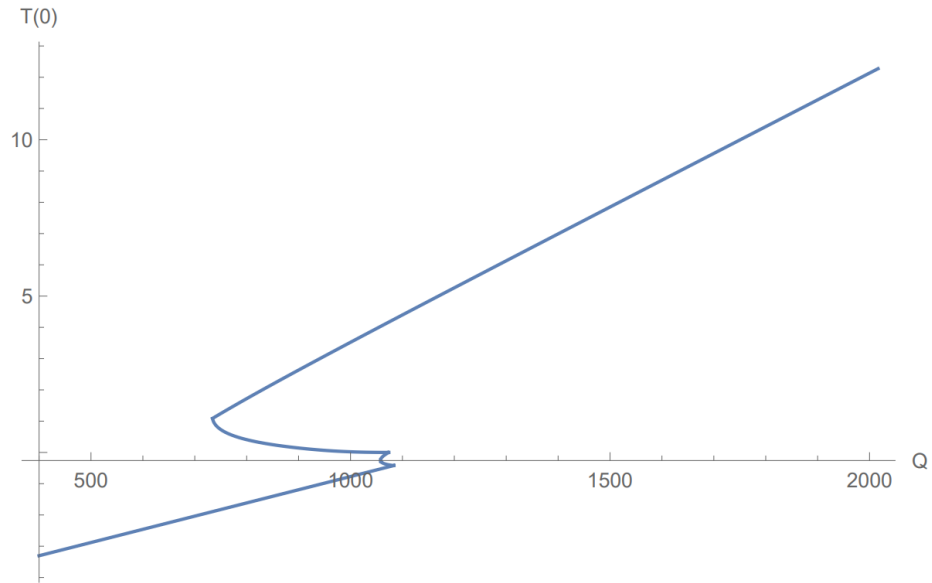


Figure 3: The bifurcation diagram, showing $T(0)$ as a function of Q . Result from *Mathematica*.

For the values of $T(0) < -0.42$ we have the snowball situation, between $T(0) = -0.42$ and $T(0) = 1.09$ are the ice and snow edge, and snow cover (two fold) solutions. Above is the ice cap solution, transitioning into the waterworld situation at much higher values of Q . The area $Q_a < Q < Q_c$ has three possible solution branches for the same value of Q , and the short zone $Q_c < Q < Q_b$ as many as 5 possible branches.

From the corresponding values of θ_f we can see that in the section $Q_a < Q < Q_i$ we have a large icecap, and for $Q_i < Q$ we have a smaller icecap that shrinks with increasing Q , transitioning into the waterworld situation. The snow edge first appears at around $T(0) = 1$, and moves from $\theta_s = \theta_c$ towards $\theta_s = 0$ with decreasing $T(0)$.

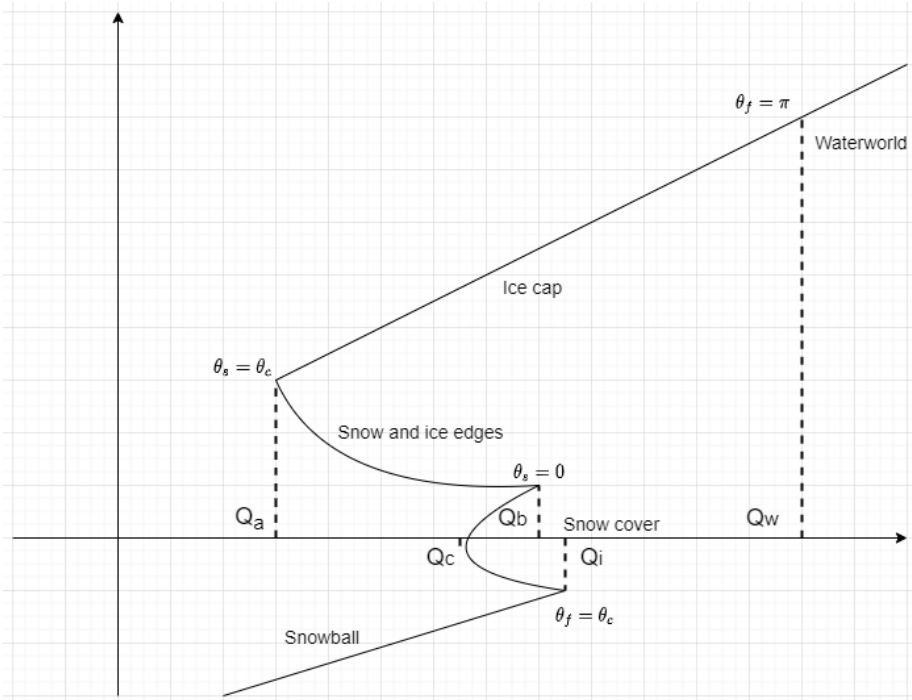


Figure 4: Drawn figure of the bifurcation diagram, showing $T(0)$ as a function of Q for the different areas. (Comprehensive recreation. Not to scale.)

The values of Q shown in the figure are given in (112), (114) and (119). The ice edge reaches $\theta_f = \pi/2$ at $Q \approx 2016.37$. This suggests the ice edge recedes more rapidly for the areas close to the substellar point with increasing Q , and then slows down as the icecap gets smaller, and the incoming radiation required to heat the entire planet is so large that the substellar point will have temperatures in the hundreds of Celsius. This is a result of the tidally locked model, and would not be realistic for a rotating planet like the earth. Having found expressions for the stationary solutions, we can now check their stability by reintroducing the time dependency, which we will do in the following sections.

4 Pseudo-spectral solution

To find solutions to the model that are **time dependent**, the first solution method that will be explored is a pseudo-spectral method based on Fourier modes.

We are considering the case of *no continents*, $K(\theta) = K_0 \implies \Gamma_i = \Gamma_0$ and $a(T) = a_0(T)$ (subscript will be suppressed), and using the spatially dimension-

less model that now has the form

$$\gamma \partial_t T - \partial_{\theta\theta} T + \beta T = \eta S(\theta)(1 - a(T)) - \alpha, \quad (120)$$

with functions and parameters defined in section [2.3](#). Our first step in solving this inhomogenous partial differential equation(PDE) is to apply the *finite Fourier transform*. The solutions of the problem, T , are expressed as a series of eigenfunctions of the spatial part of the differential operator defining the equation, with time dependent coefficients. The PDE is converted into an infinite set of coupled ordinary differential equations(ODEs), that is used to solve for the Fourier coefficients of the series. But, for our case, the albedo term presents a challenge. As it is a step function in T , it makes the right hand side (r.h.s.) of the equation highly non-linear and hard to evaluate in spectral form. We cannot solve for the coefficients analytically.

To work around this, we can solve the ODEs using a numerical ODE solver. We can then update the r.h.s. term for each iteration, by *transforming back* from spectral domain to the description using T , evaluating it, and transforming again.

In summary, we solve recursively for $T(\theta, t)$, transforming back and forth from the spectral representation for each step, starting from an initial value.

We will then use an artificial source test to validate the implementation.

4.1 Finite Fourier transform

The spatial part of the differential operator, denoted L , for our PDE [\(120\)](#) is given by

$$LT = -\partial_{\theta\theta} T + \beta T \quad (121)$$

The complete set of eigenfunctions for the spatial part of L , are the solutions of the eigenvalue problem

$$LT = \lambda T \quad (122)$$

Using the definition for L we get

$$\partial_{\theta\theta} T = (\beta - \lambda)T. \quad (123)$$

Depending on the value of lambda we get different solutions. The eigenfunction solution if $\lambda < \beta$ is

$$T(\theta) = ae^{\sqrt{\beta-\lambda}\theta} + be^{-\sqrt{\beta-\lambda}\theta}, \quad (124)$$

if $\lambda > \beta$

$$T(\theta) = ae^{i\sqrt{\lambda-\beta}\theta} + be^{-i\sqrt{\lambda-\beta}\theta} \quad (125)$$

and if $\lambda = \beta$

$$T(\theta) = a\theta + b, \quad (126)$$

where a and b are arbitrary constants. Using the periodic boundary condition (47) that T must satisfy, we get for $\lambda < \beta$

$$\begin{aligned}
T(\theta + 2\pi) &= ae^{\sqrt{\beta-\lambda}\theta} e^{\sqrt{\beta-\lambda}2\pi} + be^{-\sqrt{\beta-\lambda}\theta} e^{-\sqrt{\beta-\lambda}2\pi} \\
T(\theta) &= ae^{\sqrt{\beta-\lambda}\theta} + be^{-\sqrt{\beta-\lambda}\theta} \\
&\Downarrow \\
e^{\sqrt{\beta-\lambda}2\pi} &= e^{-\sqrt{\beta-\lambda}2\pi} = 1 \Rightarrow \sqrt{\beta-\lambda} = ik, \quad k = 1, 2, \dots
\end{aligned} \tag{127}$$

But $\beta \in \mathbb{R}$ and $\lambda < \beta$, so we must have a, b = 0.

For $\lambda > \beta$

$$\begin{aligned}
T(\theta + 2\pi) &= ae^{i\sqrt{\lambda-\beta}\theta} e^{i\sqrt{\lambda-\beta}2\pi} + be^{-i\sqrt{\lambda-\beta}\theta} e^{-i\sqrt{\lambda-\beta}2\pi} = \\
T(\theta) &= ae^{i\sqrt{\lambda-\beta}\theta} + be^{-i\sqrt{\lambda-\beta}\theta} \\
&\Downarrow \\
e^{i\sqrt{\lambda-\beta}2\pi} &= e^{-i\sqrt{\lambda-\beta}2\pi} = 1 \Rightarrow \sqrt{\lambda-\beta} = k, \quad k = 1, 2, \dots
\end{aligned} \tag{128}$$

and for $\lambda = \beta$

$$\begin{aligned}
T(\theta + 2\pi) &= a\theta + b \\
T(\theta) &= a(\theta + 2\pi) + b = a\theta + 2\pi a + b \\
&\Downarrow \\
2\pi a + b &= a + b \Rightarrow a = 0
\end{aligned} \tag{129}$$

(a, b = 0 gives a zero eigenfunction, and lambda are not eigenvalues.) This gives us an equation for λ

$$\begin{aligned}
k^2 &= \lambda - \beta \\
&\Updownarrow \\
\lambda_k &= k^2 + \beta, \quad k = 0, 1, 2, \dots
\end{aligned} \tag{130}$$

and we now have the eigenfunction

$$T_k(\theta) = ce^{ik\theta}, \quad k \in \mathbb{Z}, \tag{131}$$

where c is a constant, all the three solutions are contained in variation of k in (131). Choosing the inner product

$$(f, g) = \int_C f(\theta)g^*(\theta) d\theta \tag{132}$$

where C is the circle. We then have

$$(T_k, T_k) = \int_C c^2 d\theta = 2\pi c^2 \tag{133}$$

and we can find the normalised eigenfunction T_k , with $(T_k, T_k) = 1$, as

$$T_k = \sqrt{\frac{1}{2\pi}} e^{ik\theta}. \quad (134)$$

We can express the solution T using the inverse finite Fourier transform

$$T = \sum_k C_k T_k, \quad (135)$$

where the coefficients are defined by the finite Fourier transform

$$C_k = (T, T_k). \quad (136)$$

To find the coefficient we multiply the equation (120) with T_k and integrate over the circle

$$\gamma \partial_t C_k + \lambda_k C_k = D_k, \quad (137)$$

where we have defined

$$\begin{aligned} D_k &= (h(T), T_k), \\ h(T) &= \eta S(\theta)(1 - a(T)) - \alpha. \end{aligned} \quad (138)$$

4.2 Discrete Fourier transform

To use the method numerically, we would like to use the fast Fourier transform (FFT). FFT is an algorithm that computes the discrete Fourier transform (DFT) of a sequence of numbers. But since we are using a *pseudo*-spectral method, where we have to evaluate in both spectral form and description by T , and interchange between the two, we must have congruence between the DFT used numerically and the analytic finite Fourier transform.

Writing out the finite FT (136) and inverse finite FT (135) we get

$$\begin{aligned} C_k &= \frac{1}{\sqrt{2\pi}} \int_C T(\theta) e^{-ik\theta} \\ T &= \frac{1}{\sqrt{2\pi}} \sum_{k=-\infty}^{\infty} C_k e^{ik\theta} \end{aligned} \quad (139)$$

using the midpoint rule for integrals, with $2N$ intervals of length $\Delta\theta$ and midpoint $\theta_j = j\Delta\theta$ for the j th sub interval, we can approximate

$$C_k \approx \frac{1}{\sqrt{2\pi}} \sum_{j=-N}^{N-1} T(\theta_j) e^{-i\lambda_k \theta_j} \Delta\theta, \quad (140)$$

where $\lambda_k = k\Delta\lambda$ denotes steps in spectral domain, and we note that $\Delta\lambda = 1$ per definition of our eigenvectors, and we have $\Delta\theta = \frac{2\pi}{2N} = \frac{\pi}{N}$. Evaluating T

on this grid, and truncating the sum with the same bounds, we get

$$T(\theta_j) \approx \frac{1}{\sqrt{2\pi}} \sum_{k=-N}^{N-1} C_k e^{i\lambda_k \theta_j}. \quad (141)$$

We then have the approximated, discrete, truncated finite Fourier transforms as

$$\begin{aligned} C_k &\approx \frac{\Delta\theta}{\sqrt{2\pi}} \sum_{j=-N}^{N-1} T_j e^{-i\pi \frac{kj}{N}}, \quad k = -N, \dots, N-1 \\ T_j &\approx \frac{\Delta\lambda}{\sqrt{2\pi}} \sum_{k=-N}^{N-1} C_k e^{i\pi \frac{kj}{N}}, \quad j = -N, \dots, N-1 \end{aligned} \quad (142)$$

where $T_j \equiv T(\theta_j)$. For generality we will now consider the notation of the equivalent and similarly derived discretized truncated Fourier transform (the different signs of the exponents are interchangeable letting k run from N to $-N$ instead, and $-k \rightarrow l$)

$$\begin{aligned} F_l &= \frac{\Delta x}{\sqrt{2\pi}} \sum_{j=-N}^{N-1} f_j e^{i\pi \frac{jl}{N}}, \quad l = -N, \dots, N-1 \quad (DFT) \\ f_j &= \frac{\Delta\lambda}{\sqrt{2\pi}} \sum_{l=-N}^{N-1} F_l e^{-i\pi \frac{jl}{N}}, \quad j = -N, \dots, N-1 \quad (IDFT) \end{aligned} \quad (143)$$

In general we have the relation

$$\Delta x \Delta \lambda = \pi / N \quad (144)$$

if we want to avoid aliasing. This comes from letting $2\Delta x = p_{min} = \frac{2\pi}{\Delta\lambda}$, where $2\Delta x$ is the shortest detectable period on the grid, and p_{min} the shortest period $f(x)$ can have.

4.3 Implementation

The transformed version of the PDE (137) with the value of λ_k (130) gives

$$\partial_t C_k = \frac{1}{\gamma} (D_k - (k^2 + \beta)C_k), \quad k = 0, 1, 2, \dots \quad (145)$$

With this, an iterative method can be used to numerically solve the differential equation, and find an approximate solution $C_k(t)$. When we have found the Fourier coefficients $C_k(t)$, we can use the inverse Fourier transform to get

the solution $T(\theta, t)$ of the original PDE (120). The transformations derived in section A.1 must also be applied for implementation in python. We define

$$\begin{aligned} f(\theta) &= T(\theta, 0) \\ F_k(\lambda) &= C_k(0) \end{aligned} \quad (146)$$

where $F_k(\lambda)$ is the finite Fourier transform of $f(\theta)$, to make (145) an initial value problem.

The method that was used to solve the equation numerically was the ode integration solver from Python's `scipy` library. Setting the solar constant to be $Q = 1338$, and choosing the initial function

$$f(\theta) = 0 \quad (147)$$

we get the pseudo-spectral solution shown in figure 5, for $T(\theta, t)$ up to $t = 7$.

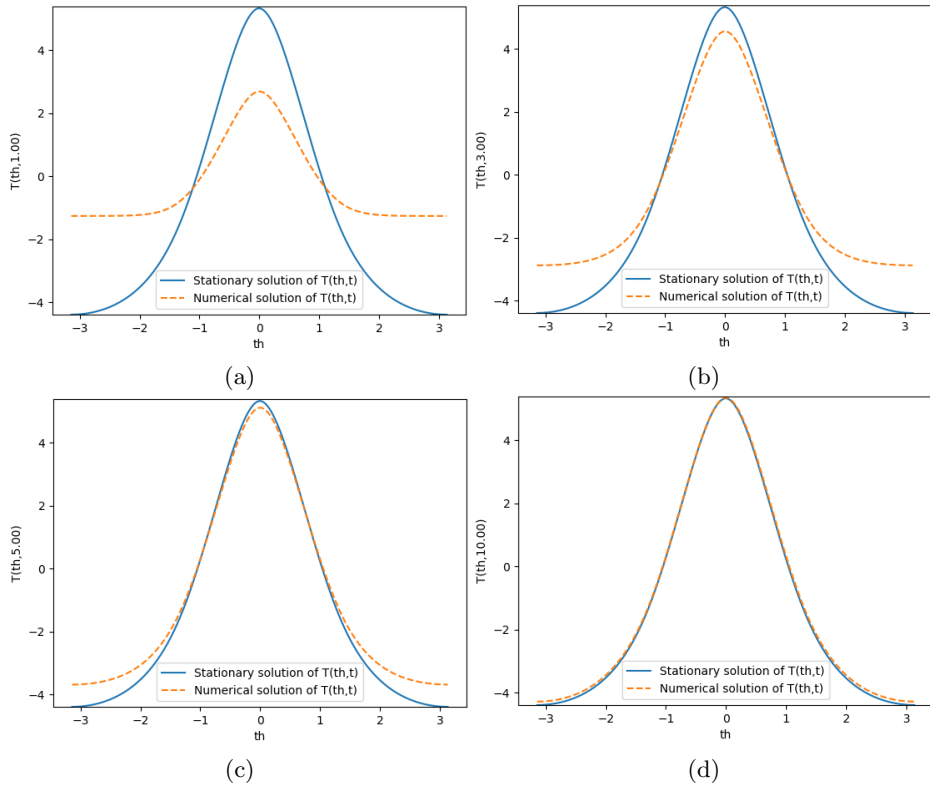


Figure 5: The numerical solution for $T(\theta, t)$ for the energy balance model (120) with initial value (147), and the stationary solution at $Q = 1338$ at (a) $t = 1$. (b) $t = 3$. (c) $t = 5$. (d) $t = 10$.

We can see the temperature spikes around the substellar point, while it drops rapidly towards the poles, at $\pm\pi/2$, and evens out further towards the antistellar point. The spike in temperature at the substellar point then rounds more out over time, and the area around the antistellar point cools further. This seems to be logical considering that the sun/star heats the closest point most strongly, and that the heat is spreading and evening out over time.

At $t > 5$ the distribution settles more slowly into a seemingly stationary state. Using what we found in the previous section, the value of $Q = 1338$ should only have one possible stationary solution. Plotting this ice edge stationary solution (no continents) alongside the pseudo spectral solution we see this seems to be what the distribution is converging towards.

The ice edge position is situated around ± 1.04 radians when the change starts to slow. This follows expectations considering the diffusive constant was fitted to give an ice edge $\theta = 0.95$, and an approximately realistic distribution, with $Q = 1338$ but for one continent present. For no continent the diffusivity is higher, and the edge further out.

5 Finite difference solution

The second method for finding **time dependent** solutions to the model (28) that will be considered is a finite difference algorithm. This will allow us to solve for time dependent solutions, and to examine how the stationary solutions change in time if disturbed from their time independent state. As such, we can test the stability of the stationary solutions.

The finite difference method is based on replacing derivatives in differential equations with discrete approximations, and evaluating on a grid to produce a system of equations. These equations can then be solved to find approximations of the exact values.

Considering the time dependent version of the energy balance model

$$\gamma_i \partial_t T - \partial_{\theta\theta} T + \beta_i T = h_i(T) = \eta_i S(\theta)(1 - a_i(T)) - \alpha_i, \quad (148)$$

with the boundary conditions that were found in section 3, we discrete the boundary value problem on a uniform grid

$$\begin{aligned} \theta_j &= d\theta j, & j &= 0, \dots, N \\ t_n &= kn, & n &= 0, \dots, T \end{aligned} \quad (149)$$

Where h is the step length in space, and k in time. The grid becomes (θ_j, t_n) .

The derivatives are replaced by approximation formulas. The derivative in time, $\partial_t T$, by the forward difference formula

$$T_t = \frac{T_j^{n+1} - T_j^n}{k} \quad (150)$$

and the second derivative in space by the centred difference formula

$$T_{\theta\theta} = \frac{T_{j-1}^n - 2T_j^n + T_{j+1}^n}{d\theta^2} \quad (151)$$

When substituted into the energy balance model (148) we get:

$$\gamma_i \frac{T_j^{n+1} - T_j^n}{k} - \frac{T_{j-1}^n - 2T_j^n + T_{j+1}^n}{d\theta^2} + \beta_i T_j^n = h_{ij}^n \quad (152)$$

$$T_j^{n+1} = (\gamma_i - 2s - k\beta_i) \frac{1}{\gamma_i} T_j^n + \frac{s}{\gamma_i} (T_{j-1}^n + T_{j+1}^n) + \frac{k}{\gamma_i} h_{ij}^n, \quad s = \frac{k}{d\theta^2} \quad (153)$$

For the boundaries we can use the centre difference, which requires the introduction of the *ghost points* T_{-1}^n and T_{N+1}^n .

We must also consider the continent edges θ_{ci} , where the temperature function is continuous, but not continuously differentiable. Using the boundary condition (52) we can find an expression binding the solution on either side of the edge. Using the backward difference below the edge, and the forward difference above, we get for the *upper* edge of a continent i

$$D_i \left(\frac{T_{N_i-2}^n - 4T_{N_i-1}^n + 3T_{N_i}^n}{2d\theta} \right) = D_0 \left(\frac{-3T_{N_i}^n + 4T_{N_i+1}^n - T_{N_i+2}^n}{2d\theta} \right) \quad (154)$$

$$T_{N_i}^n = \frac{1}{3(D_i + D_0)} (D_i(4T_{N_i-1}^n - T_{N_i-2}^n) + D_0(4T_{N_i+1}^n - T_{N_i+2}^n)) \quad (155)$$

where $T_{N_i}^n$ is the point approximately at θ_{ci} , labeled with a and b for upper and lower edge when applicable. For the *lower* edge, the diffusivity is switched $D_0 \leftrightarrow D_i$. It is also possible to split into two schemes bound by this point exactly defined at θ_{ci} , with a jointly non-uniform grid.

The numerical scheme is then

$$\begin{aligned} T_j^{n+1} &= (\gamma_i - 2s - k\beta_i) \frac{1}{\gamma_i} T_j^n + \frac{s}{\gamma_i} (T_{j-1}^n + T_{j+1}^n) + \frac{k}{\gamma_i} h_{ij}^n \\ j &= \{0, \dots, N\} \setminus \{N_i\} \\ T_{N_i}^n &= \frac{1}{3(D_i + D_0)} (D_i(4T_{N_i-1}^n - T_{N_i-2}^n) + D_0(4T_{N_i+1}^n - T_{N_i+2}^n)) \\ D_0 &\leftrightarrow D_i \text{ for lower edge of continent i} \end{aligned} \quad (156)$$

For use of the finite difference algorithm, it is assumed that the functions change gradually. But this is not fulfilled for the function $H_i(T)$, being a step functions in T . To fix this problem, we can instead use an approximated step function that is smooth but steep. A function that works for our purposes is for example

$$a_i(T) = \frac{a_1 + a_2}{2} + \frac{a_1 - a_2}{2} \tanh(100(T + \frac{T_s}{T_{s0}})). \quad (157)$$

for a region i with $T_s = T_{s1}$ we then have $\tanh(100T)$, and for the water region $i = 0$ we have $\tanh(100(T + 1))$. We still have to change at the boundaries of regions.

5.1 Continent symmetry

When we have symmetry we can restrict to only considering the **upper half circle**. When this is the case we have $\theta_0 = 0$, $\theta_N = \pi$ and thus $d\theta = \frac{\pi-0}{N} = \frac{\pi}{N}$. For the ghost points, the boundary conditions (55) and (54) gives

$$\frac{T_1^n - T_{-1}^n}{2d\theta} = 0 \quad \Leftrightarrow \quad T_{-1}^n = T_1^n, \quad (158)$$

$$\frac{T_{N+1}^n - T_{N-1}^n}{2d\theta} = 0 \quad \Leftrightarrow \quad T_{N+1}^n = T_{N-1}^n. \quad (159)$$

If we do not have symmetry, or instead want to consider the **whole circle**, then $\theta_0 = -\pi$, $\theta_N = \pi$ and $d\theta = \frac{\pi-(-\pi)}{N} = \frac{2\pi}{N}$.

For the ghost points we use the periodic condition (47), and all points must satisfy

$$T_j^n = T_{j+N}^n. \quad (160)$$

5.2 Pseudo spectral comparison

Since we have two methods of finding the time dependent solution, we can now see if they agree. Considering again the case of no continents, with the value $Q = 1338$ and initial value (147) (as was done in section 4.3), we get the result shown in figure 6. The plot shows the resulting distribution when $t = 10$ has been reached, and since the case is symmetric we show only the upper half-circle for a closer look.

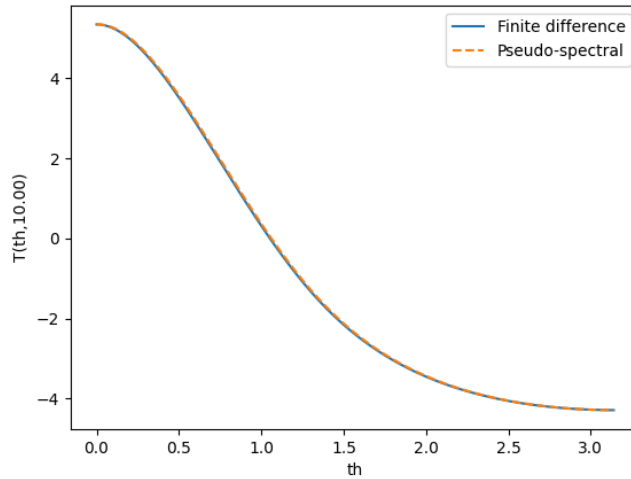


Figure 6: The numerical solution for $T(\theta, t)$ for the energy balance model (120) with no continents, with initial value (147) and $Q = 1338$ at $t = 10$.

As both the time dependent solutions seem to agree, it gives more validity to both methods derivation and implementation.

5.3 Artificial source test

To verify our implementation we will use an artificial source test. A solution that satisfies the boundary conditions is for example

$$T(\theta, t) = \cos(\theta) \left(1 + \frac{1}{1+t}\right) \quad (161)$$

Inserting into the partial differential equation we find the artificial source function that corresponds to assuming this solution

$$\gamma_i \partial_t T - \partial_{\theta\theta} T + \beta_i T = \rho(\theta, t) \quad (162)$$

$$\begin{aligned} \rho(\theta, t) &= -\gamma_i \cos(\theta) \frac{1}{(1+t)^2} + \cos(\theta) \left(1 + \frac{1}{1+t}\right) + \beta_i \cos(\theta) \left(1 + \frac{1}{1+t}\right) \\ &= \left(-\frac{\gamma_i}{(1+t)^2} + (1 + \beta_i) \left(1 + \frac{1}{1+t}\right) \right) \cos(\theta) \\ &= \left(-\frac{\gamma_i}{(1+t)^2} + (1 + \beta_i) \left(\frac{2+t}{1+t}\right) \right) \cos(\theta) \end{aligned} \quad (163)$$

Comparing the chosen solution to the finite difference solution over time, but with the right hand side now being set as (163), will give an idea of the accuracy of the implementation.

With the artificial source (163) we get the comparisons shown in figure 7 between the chosen function (161) and the numerical solution of (162) for $T(\theta, 10)$. The result shows a close approximation to the exact function, and validates our implementation. The finite difference solution should therefore give a good approximation for the time dependent case of the energy balance model (120). Since the pseudo spectral implementation was shown in 5.2 to agree with the finite difference implementation, this also further validates the pseudo spectral implementation.

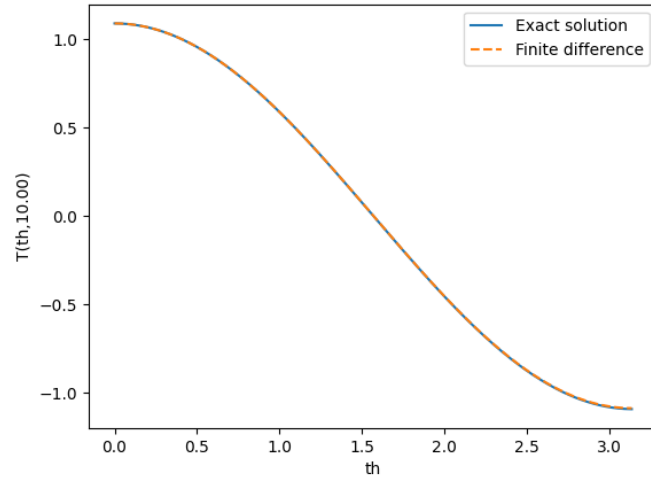


Figure 7: The the exact solution (161), *blue*, and numerical solution for $T(\theta, t)$ for the equation (162), *orange*, at $t = 10$.

6 Stability

Since we have found more than one possible stationary solution for the same values of Q , it is important to examine the stability of these solutions, as it can determine which of the states the system is inclined to occupy.

The stationary solutions found in section 3 are by definition time invariant, and should not change over time. To give some base line credibility to both our stationary solutions and the finite difference implementation, we can run the code for an amount of time and see if it behaves as expected. Considering the case $Q = 1338$ again with the solutions that were found in section 3.6 we get the result in figure 8 for time $t = 10$.

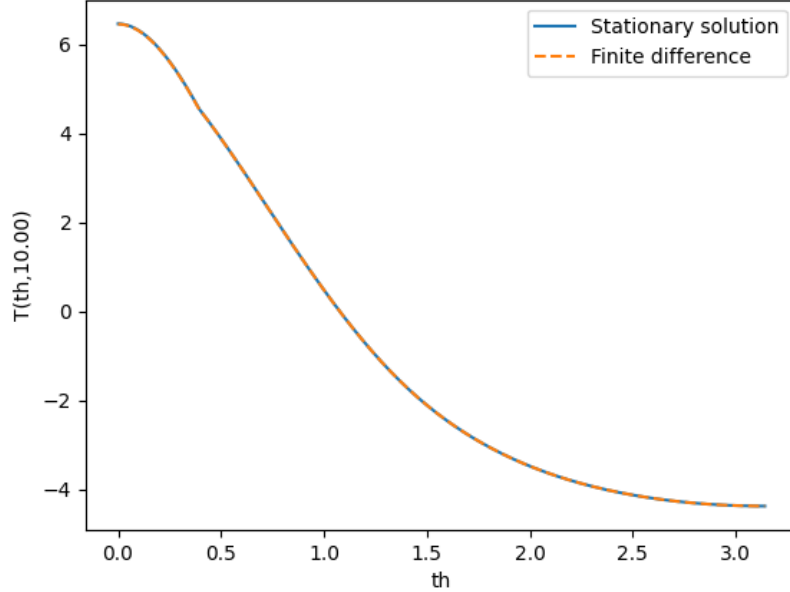


Figure 8: The the stationary solution for the case of one symmetric continent with $Q = 1338$, $\theta_c = \pi/4$, *blue*, and numerical solution for $T(\theta, t)$, *orange*, at $t = 10$.

We can see the time dependent solution overlaps closely with the stationary solution, which gives more validity to both derivations and implementations.

Now we introduce a small perturbation to the stationary solutions. Letting $T_0(\theta)$ denote a stationary solution, we have the initial temperature function

$$T(\theta, 0) = T_0(\theta) + \delta T(\theta). \quad (164)$$

The perturbation was chosen to be

$$\delta T(\theta) = \pm \epsilon \cos \theta, \quad (165)$$

where ϵ is a small number, set to be $\epsilon = 0.1$ in general. With this function the total change is zero over the interval, but the substellar and antistellar temperatures are perturbed positively or negatively. Examining the development over time after the perturbation, we can either see the temperature relax into the original stationary state, or change to some different state. In the latter case we can conclude that the stationary solution is unstable. For most situations the planet can be in the stationary solutions appear to be stable. But where there are multiple possible states for the same Q , things get more complicated.

We note that the stability results we perceive in this analysis is on a certain timescale. The radiation distribution function is averaged over long timescales, to be independent of time, but would on a shorter timescale have fluctuations. It is also impossible to know if the states are truly stable further into the future, on a larger timescale. This is a limitation built into our model.

6.1 One symmetric continent stability

We will now apply this method to the one continent solution from sections 3.6 and 3.7. Examining the solutions a value of $Q = 1065 \in (Q_c, Q_b)$ where there are 5 possible solutions, for both cases of the perturbation (165) positive and negative sign and $\epsilon = 0.1, 0.01$, we get the results shown in figures 9, 10, 11, 12, and 13. The colour coding for the different situations will be as follows

SI	snowball	Purple
SWI2	snow cover (lower $T(0)$ branch)	Cyan
SWI1	snow cover (upper $T(0)$ branch)	Cyan
LSWI	ice and snow edge	Green
LWI	ice cap	Red

Positive $\epsilon = 0.1$ perturbation is shown unless another choice yields a different conclusion. The first graphs shows the stationary solutions against the finite difference solutions for the perturbation, and the second graphs show the difference between the finite difference solutions and the stationary solutions over time (norm of difference).

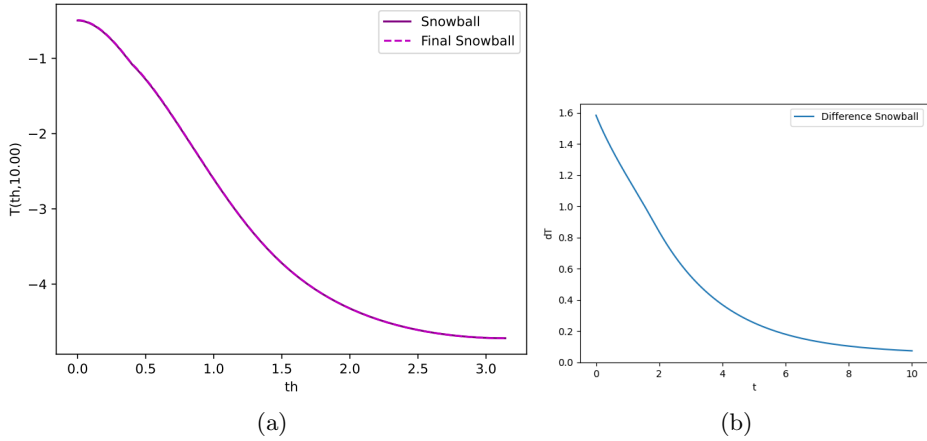


Figure 9: (a) Snowball stationary solution SI, *line*, finite difference solution ($+\epsilon = 0.1$ perturbation), *dotted line*, for $t=10$. (b) Difference between solutions.

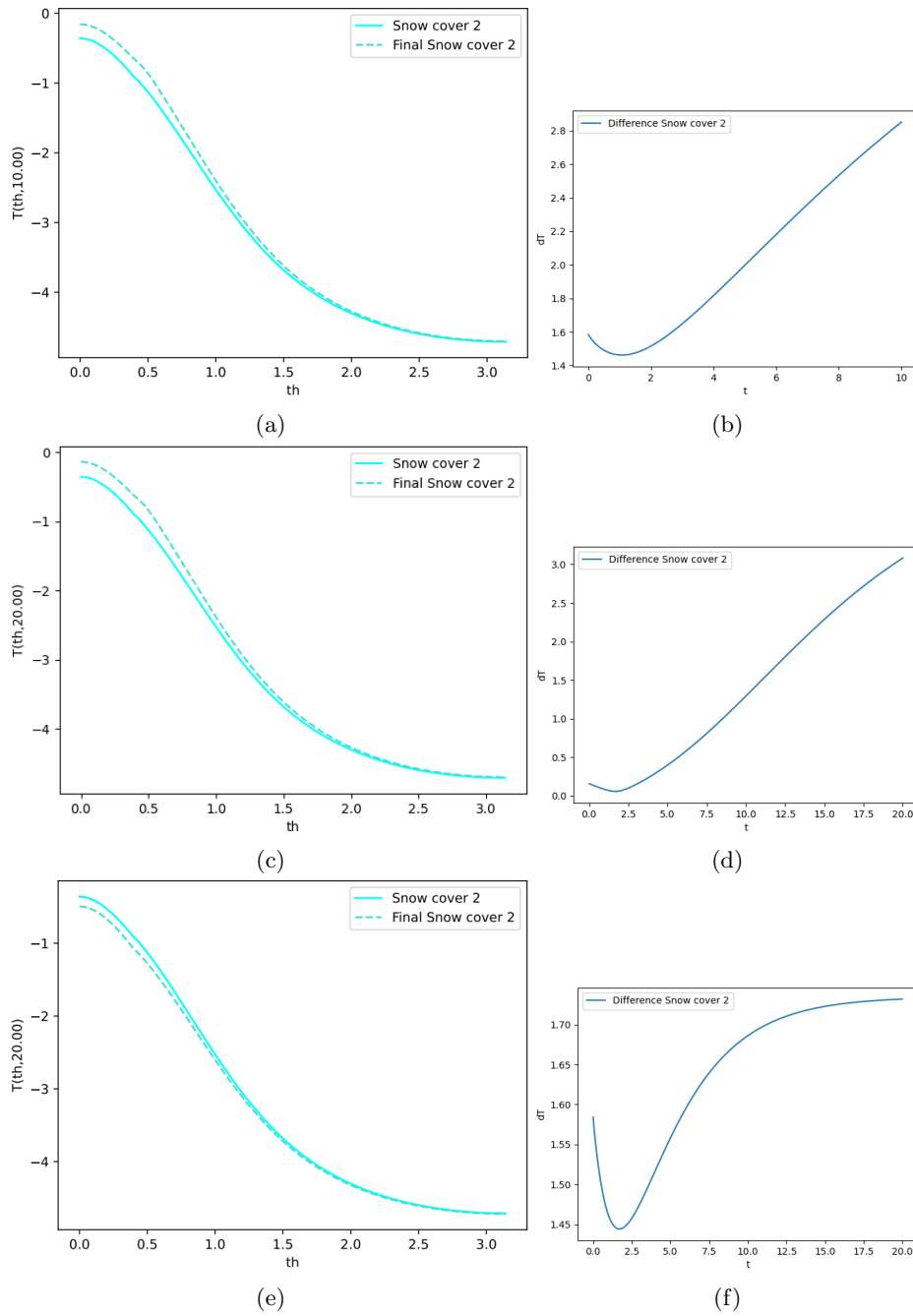


Figure 10: Lower snow cover stationary solution SWI2, *line*, finite difference solution, *dotted line* for (a) $+\epsilon = 0.1$ perturbation, $t=10$. (c) $-\epsilon = -0.01$ perturbation, $t=20$. (e) $-\epsilon = -0.1$ perturbation, $t=20$. (b,d,f) Difference between solutions.

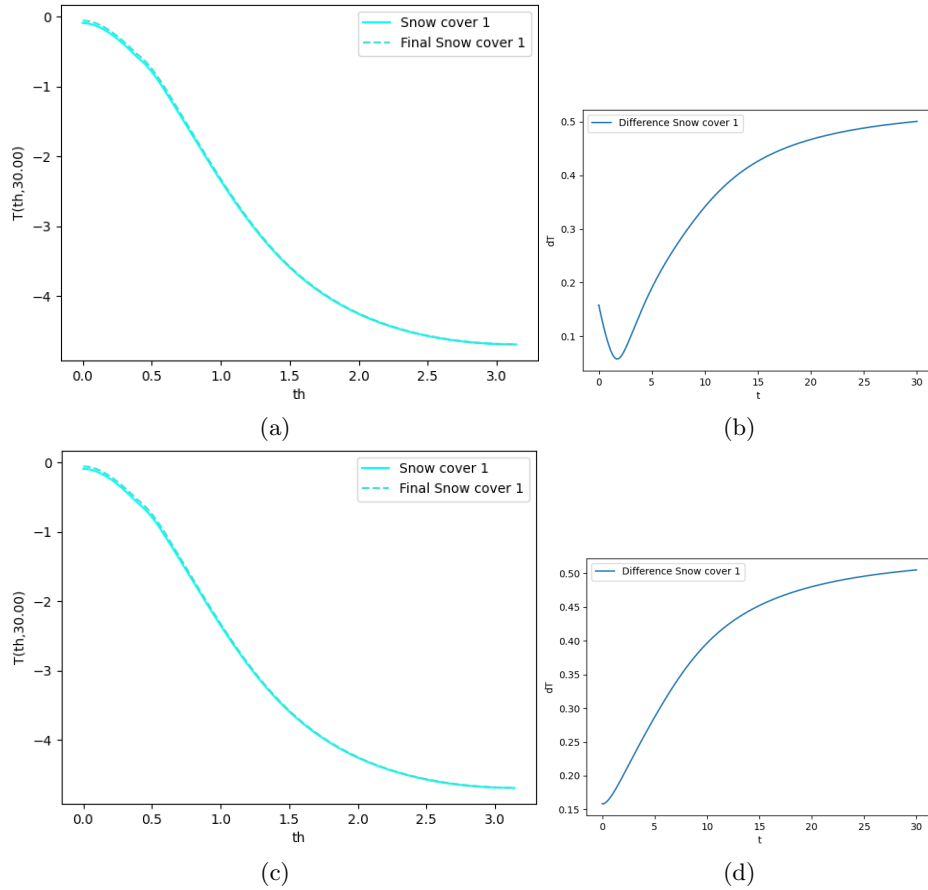


Figure 11: (a) Upper snow cover stationary solution SWI1, *line*, finite difference solution ($+\epsilon = 0.01$ perturbation), *dotted line*, for $t=30$. (c) $-\epsilon = -0.01$ perturbation, $t=30$. (b,d) Difference between solutions.

The snowball and ice cap solutions seem to settle back to the stationary solutions for both the positive and negative perturbation, but for the snow and ice edge (LSWI) and snow cover (SWI) solutions we can observe the difference from the stationary solutions grow. We can conclude that the LSWI and SWI2 solutions are *unstable*, while the snowball and ice edge solutions appear to be *stable*. But we need to consider SWI1 more closely, as behaves stable in that it settles into a solution (flattening difference curve), but not at the value of the calculated stationary solution. The norm of difference is large, and much larger than the initial perturbed stationary solution.

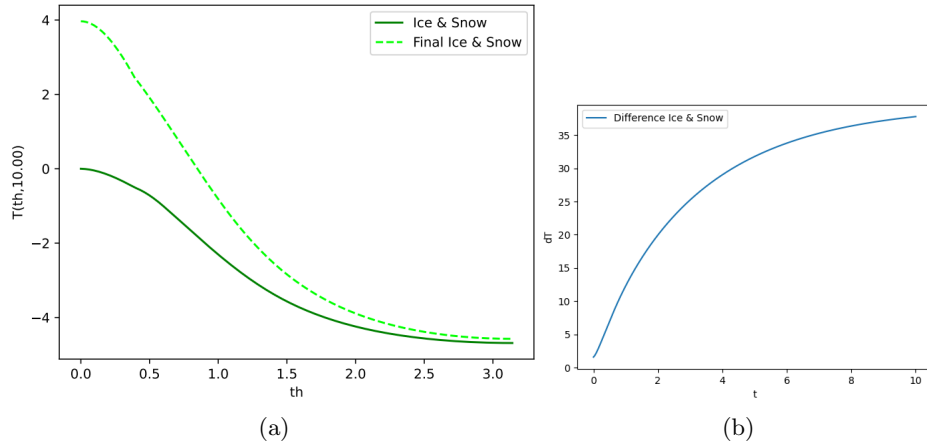


Figure 12: (a) Snow and ice edge stationary solution LSWI, *line*, finite difference solution ($+\epsilon = 0.1$ perturbation), *dotted line*, for $t=10$. (b) Difference between solutions.

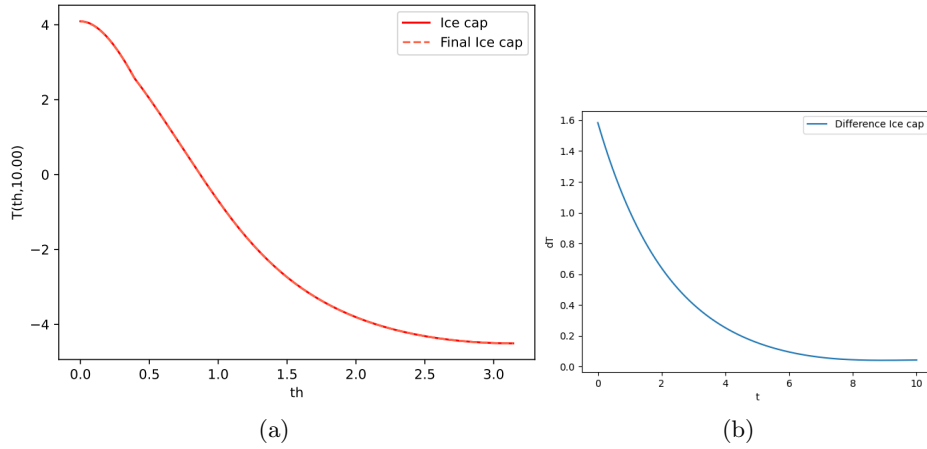


Figure 13: (a) Ice edge stationary solution LWI, *line*, finite difference solution ($+\epsilon = 0.1$ perturbation), *dotted line*, for $t=10$. (b) Difference between solutions.

Some of the growing difference curves flatten out over time. Comparing the end result to the other stationary solutions we can see that the solution most likely settles into another stationary state. The shape of the LSWI solution suggests it transitions into the ice cap solution. In the same way, the SWI2 solution seems to transition to the snowball solution with a large enough negative perturbation. But with positive perturbation, the change is more gradual and

does not settle. At least not at a rate as fast as for the other solution. This is probably because it "falls into" the other states above but does not settle and is further drifting again.

The *upper* snow cover solution does seem to settle into a stationary state as well, but it is not the stationary solution or any other solution. Yet it is very close. This is probably because of the approximation made in the finite difference code. There will always be some numerical error but this larger discrepancy can be explained by the `tanh` approximation for albedo function, which we will see later has a strong effect on areas with sharp folds. Using the tool *Auto-07p* to find the approximated stationary solution, we find that the slightly different stationary state seen here *is* in fact the stationary solution for the approximated problem, with a substellar temperature of $T(0) \approx -0.0583$ instead of the analytic $T(0) \approx -0.0923$. The SWI1 then appears to be stable for small perturbations.

The unstable middle solutions will in general, depending on the perturbation direction, transition to one of the seemingly stationary outer solutions. The rate of change depending on the proximity to other solutions, stable and unstable. We can use this method to check the stability in other cases going forwards. Having *bistability* where only the upper and lower lines are stable in a folded area is generally what we expect, but for the short interval $Q_c < Q < Q_b$ we seem to have *tristability*, due to the stable behaviour of the SWI1 solution. This suggests there could, for a different configuration, exist a middle step between the ice cap and snowball situations.

7 Effects on bistability

7.1 Variation of continent parameters

With the stationary solution found in section 3 we can now investigate how the **placement** of the continents and their **size** influences the bistability of the system which was shown in section 5. Using the case of one symmetric continent considered in section 3.6 and 3.7 as a starting off point, we will vary the position of the continents edges and solve in the same way to find the bifurcation diagram. What we will measure as the influence on bistability is the dimensions of the bifurcation area. Figure 14 is an illustration of this, using the original diagram 3.

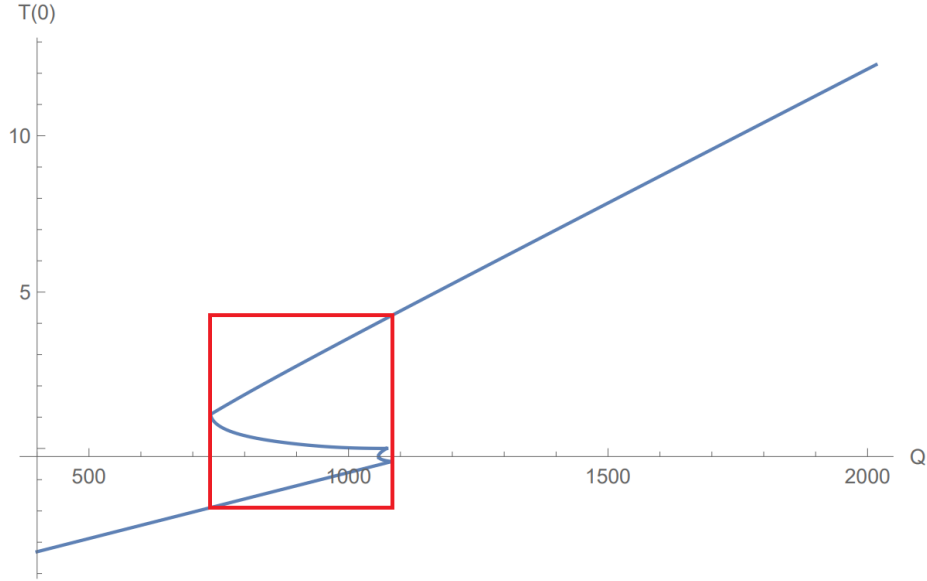


Figure 14: The bifurcation area for the case of section [3.6](#) and [3.7](#), enclosed by a red box.

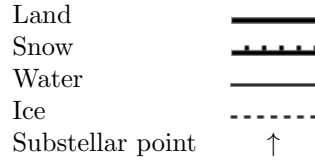
The area of interest is the red box, and its *height* and *width* will be measured for a different continent. In general we define for the upper and lower edge of the continent

$$\begin{aligned}\theta_{c1} &= +\frac{l}{2} + \epsilon, \\ \theta_{c0} &= -\frac{l}{2} + \epsilon,\end{aligned}\tag{166}$$

where l is the size of the continent and ϵ the shift of the centre from the substellar point. Both in radians. Note that when only l is varied we can use the previously derived equations, one symmetric continent with a new θ_c , but when ϵ is varied we have to consider the *non-symmetric* case. We will have the same intervals as before, but must also add the segments of the lower half circle. There will also be a different range of possible situations, especially with a high ϵ . The full circle case corresponding to the one in section [3.6](#) would have the following segments C_j

$$\{-\pi, \theta_f], [\theta_f, \theta_{c0}], [\theta_{c0}, \theta_{s0}], [\theta_{s0}, 0], [0, \theta_{s1}], [\theta_{s1}, \theta_{c1}], [\theta_{c1}, \theta_f], [\theta_f, \pi]\},\tag{167}$$

which are intervals of **Ice**, **Water**, **Snow**, **Land**, **Land**, **Snow**, **Water**, **Ice**. Representing the areas as before



We can show (167) visually as



The double land interval can be considered one interval $[\theta_{s0}, \theta_{s1}]$. As our radiation distribution function (29) is a piecewise function it can also be useful to keep a split around 0 the during computation.

When solving the equations for the non-symmetric case we cannot use the symmetric boundary conditions in section 3.1, but will use the *conditions* (47), (51), (52) and (85), (87). Using these intervals and conditions with the general formulae (82), (83) we get the *equations*, and with solved equations and the general integral identity (81) we get the *solutions*.

7.1.1 Effects of size

Letting only the **size** of the continent vary, we can use the *symmetric* solution derived in section 3.6 and 3.7. We set

$$\theta_c = \frac{l}{2}, \quad l \in (0, 2) \tag{168}$$

Examining the bifurcation diagram for different lengths, we get the dimensions shown in figures 15 and 16.

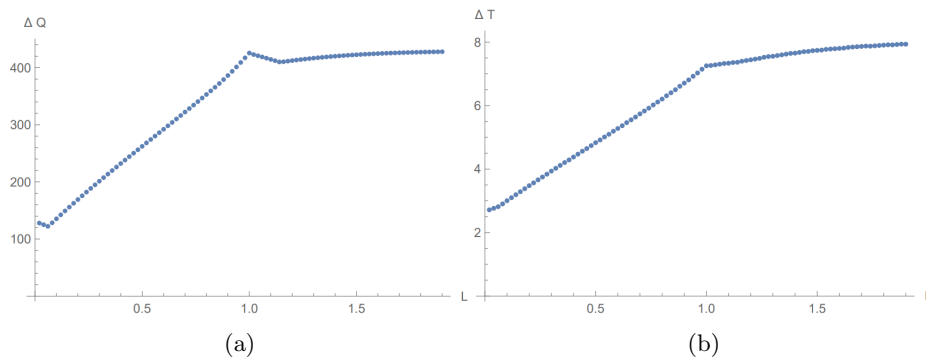


Figure 15: The dimensions of the bifurcation area for a symmetric continent with **size** given by (168). (a) Width ΔQ . (b) Height ΔT .

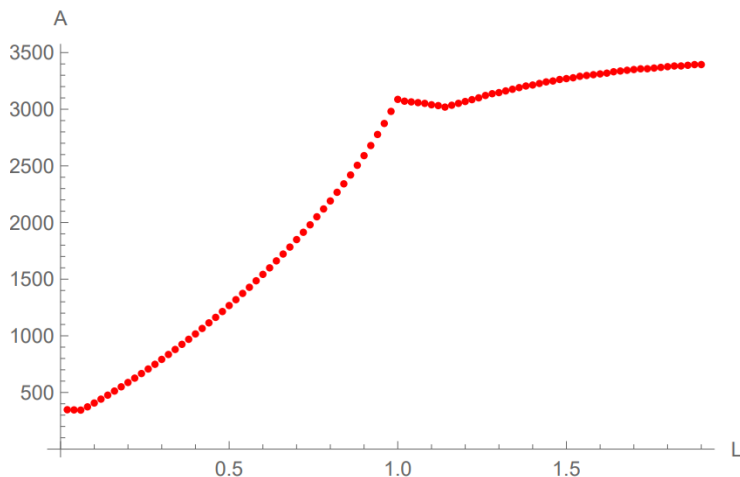


Figure 16: The area of the red box $A = \Delta Q \Delta T$ for a symmetric continent with size given by (168).

Both the height and the width of the area of bifurcation increases with the size of the continent, first in a seemingly linear way. The area increase in the same area is thus more quadratic. Interestingly, the size $l = 1$ seems to be a big turning point. Examining the form and components of the bifurcation diagram hints as to why this happens. A collection of the bifurcation diagrams can be found in appendix [A.2](#).

At a size of about $l = 1$ the **snow cover** situation ceases to have any solution. Instead, the previously solution-less **ice cover** situation now has a solution. This would mean the continent at that point is so large that with cooling the ice edge reaches the continent edge before the snow edge reaches the substellar point. While below it was the opposite. The other situations also vary between having one and two solutions in ranges of Q where solutions exist. The the ice and snow edge solution, for instance, has two solutions for a small interval of Q values when l passes around $l = 0.9$.

These kinds of shifts change which situation has its solutions at the outermost values of Q in the area, and result in the sudden shifts in width we observe. As for the slower increase after $l = 1$, this seems to be because the diagram has less folds, and approaches the form observed for no continents ($l = 0$). It becomes in essence a waterworld only with a lower diffusivity, and continent size is no longer affects the size significantly.

7.1.2 Effects of position

Letting only the **position** of the continent vary, we must use the *non-symmetric* solution. Using the short hand notation **L** = **Land**, **S** = **Snow**, **W** = **Water**, **I** = **Ice**, the new situations to consider, in addition to the ones found for the symmetric case, are illustrated in table [\(I\)](#).

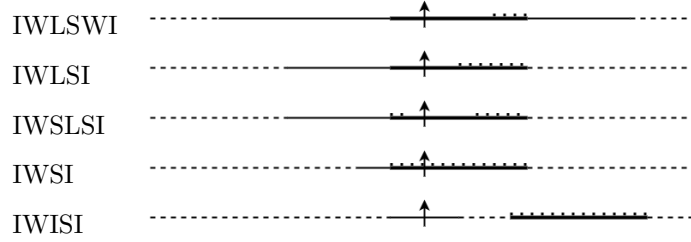


Table 1: Possible situations for a shifted continent.

The situation has solutions depending on the magnitude of the shift ϵ . The case IWSLSI is relevant for a minor shift, and IWLSI takes its place when the shift is increased further. IWISI becomes relevant when the shift brings it closer to the pole. We will consider the original size (103) used in section 3.6.

$$\begin{aligned}\theta_{c1} &= +\frac{\pi}{8} + \epsilon, \\ \theta_{c0} &= -\frac{\pi}{8} + \epsilon.\end{aligned}\tag{169}$$

Examining the bifurcation diagram for increasing continental shift ϵ , we get the dimensions shown in figures 17 and 18.

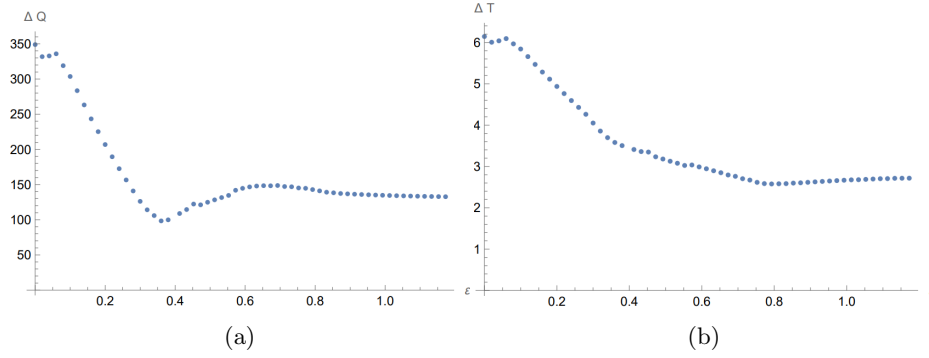


Figure 17: The dimensions of the bifurcation area for a continent of size $\theta_c = \pi/8$ with **position** given by (169). (a) Width ΔQ . (b) Height ΔT .

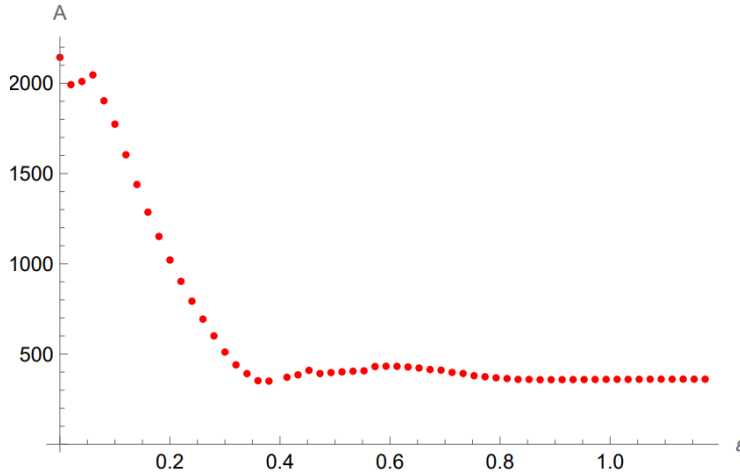


Figure 18: The area of the red box $A = \Delta Q \Delta T$ for a continent of size $\theta_c = \pi/8$ with **position** given by (169).

Both the width and height of the area decreases rapidly with increasing position, with a slight increase of width when $\epsilon \approx 0.4$ which is when the continent no longer connects with the substellar point. The area flattens out past this point. A collection of the bifurcation diagrams can be found in appendix [A.3](#). The bifurcation area grows with increasing continent **size** and gets smaller with increasing **position**. From this we conclude that the bifurcation area is largest with $\epsilon \approx 0$ and $l \gtrsim 1$, a large continent around the equator.

7.2 Variation of radiation distribution function

In the previous section it was discovered that the bifurcation area was smaller the further the **position** of the continent was from the substellar point, and larger the bigger the **size** of the continent, with diminishing returns and less folds beyond $l \approx 1$. Based on this result, we will now consider a continent of size $l = 1$ around the substellar point, or

$$\begin{aligned} \theta_{c1} &= +\frac{1}{2}, \\ \theta_{c0} &= -\frac{1}{2}, \end{aligned} \tag{170}$$

to maximise the area of interest while keeping the continent small enough to give unique effects, not just a planet with lower diffusivity. To further investigate this case we will try to vary a different element.

In section [2.3](#) we defined the radiation distribution function [\(29\)](#), which is a "tent" shaped piece-wise function with a sharp peak and rapid decline. For a planet like earth that rotates, it would be appropriate to model the function as much flatter, as the incoming radiation is distributed along the circle at the

given longitude instead of a point. The function used by North was based on the second Legendre polynomial, and determined by astronomical calculations. We now want to examine what happens if we flatten the distribution for our circle model, and approach what is used for a rotating planet instead of tidal locking.

To investigate the effects of steepness of the curve a new function $S(\theta)$ is introduced

$$S(\theta) = e^{-c\theta^2}. \tag{171}$$

The Gaussian function has a rounded peak, and the constant c can be varied to adjust its width. We will first try a slope of similar shape to North's.

7.2.1 North approximate shape

Using the value $c = 1/2$, we get a slope with approximately the same shape as North's function for $\theta \in (0, \pi/2)$. Finding the bifurcation diagram by the method of sections [3.6](#) and [3.7](#) we get the result shown in figure [19](#).

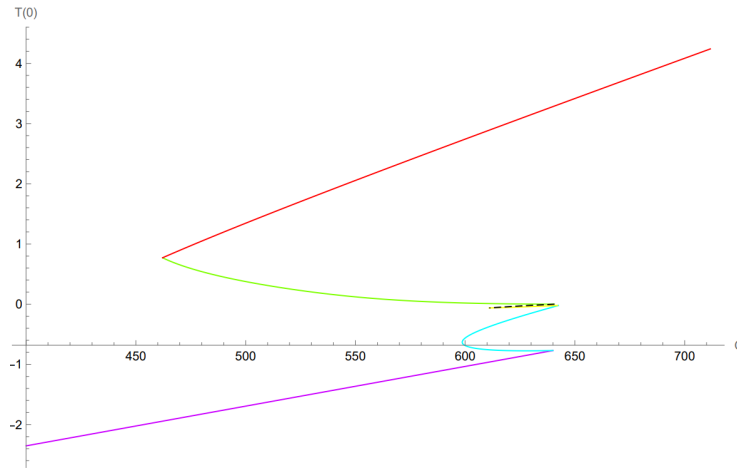


Figure 19: The bifurcation diagram for one symmetric continent with a North-like radiation distribution function, [\(171\)](#) with $c=1/2$.

The color coding is as follows:

LWI	ice cap	Red
LSWI	ice + snow edge	Green
SLSWI	two snow zones	Black –
SLWI	ice + snow edge (var.)	Yellow
SWI	snow cover	Cyan
LSI	ice cover	Blue
SI	snowball	Purple

Table 2: Possible situations for a function [\(171\)](#) with $c=1/2$.

This bifurcation diagram looks quite similar to the one found with the tent $S(\theta)$ function and $l = \pi/4$ seen in figure 3, but a new fold has appeared. A closer look can be seen in figure 20.

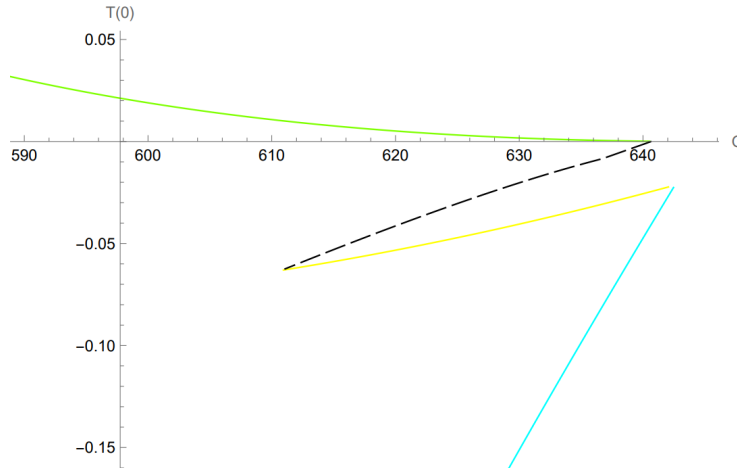
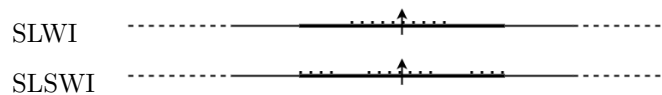


Figure 20: A segment of the bifurcation diagram in figure 19.

Among the new lines is a version of the ice and snow edge solution, but with snow in the *interior* of the continent (yellow). It seems the broader radiation distribution allows the land closest to the ocean to absorb more heat, as there is more incoming radiation further from the peak, and also receive more from the ocean due to its higher heat diffusivity. We can thus no longer assume condition (104) of an absolute decrease of temperature, for this and further cases. It is then more difficult to calculate transitional values of Q between situations, as we have to determine the peak of the temperature distribution.



Even more interesting is the other new possibility, which is a case of *several* disjoint areas of snow within one continent. More than just encroaching from one or both edges, we get interchanging intervals. Such a possibility logically follows the situation of the internal snow area, but adds a whole new layer of intrigue. And most certainly, of complication.

7.2.2 Effects of function width

Inspired by the discoveries of several snow zones, we further increase the width of the Gaussian (171). We consider the value $c = 1/10$, and solve to find the bifurcation diagram once again. Keeping in mind the results of the previous

calculation, we expect the possible situations we have to solve for get increasingly difficult. If we first consider only the cases we have seen before we get the result shown in figure 21.

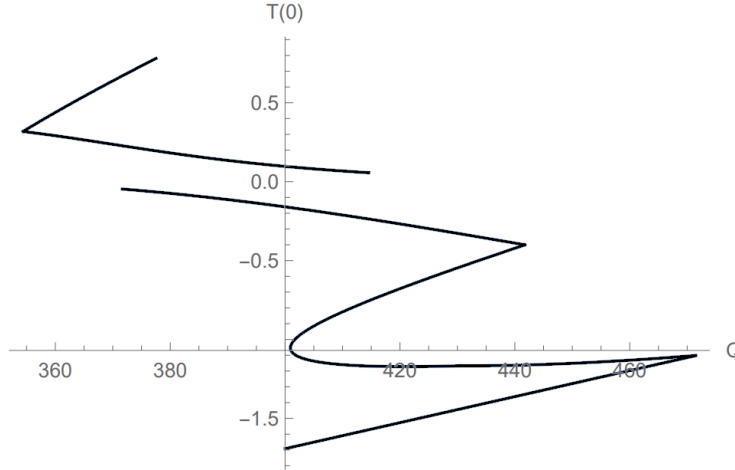
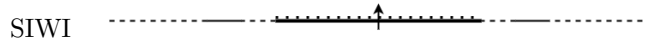


Figure 21: The incomplete bifurcation diagram for one symmetric continent with radiation distribution function (171) with $c=1/10$.

The cases that are present are the same ones seen in table 2, only excluding the double snow zone (SLSWI), and with the addition of a solution with ice close to the continent (SIWI). This new addition suggests the peak temperature can now also be situated outside the continent entirely.



Examining the plot, we can see that the rounded snow cover portion (Formerly cyan) has grown larger. And the line that was the snow and ice edge solution (green) has split into two, with a large void in between. These two lines being the LSWI and SLWI solutions, inner and outer snow area. By the same logic as the previous case, this void is probably bridged by one or several cases of multiple snow zone solutions.

Trying to find solutions for the case of two snow edges, both with snow at the substellar point as before (SLSWI) and with land (LSLWI), then with three edges, and so on, we get the result in figure 22.

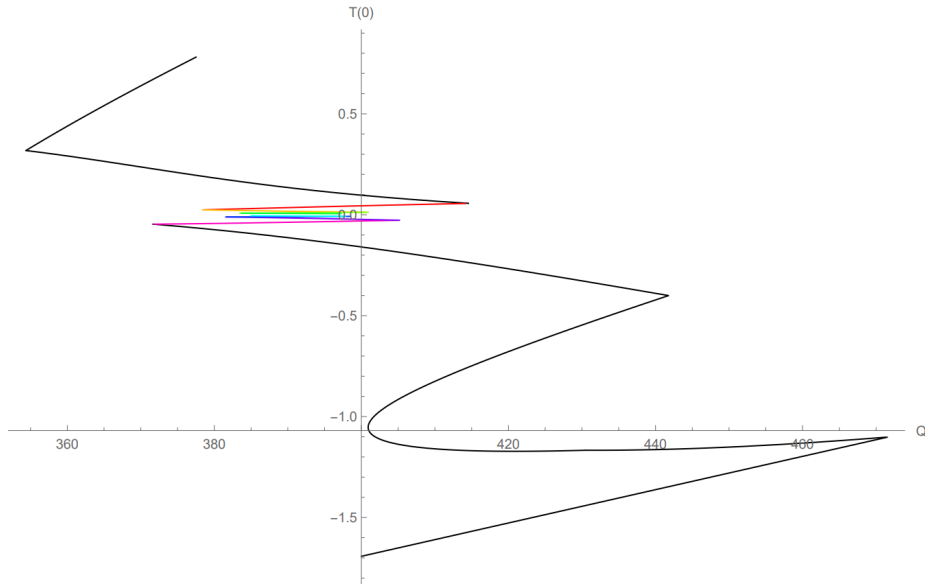


Figure 22: The bifurcation diagram for one symmetric continent with radiation distribution function (171) with $c=1/10$.

The colourful area contains the multiple snow zone solutions. The colour coding is as follows:

LSLWI		Red
LSLSWI		Yellow
LSLSLWI		Lime
LSLSLSWI		Green
SLSLSLWI		Cyan
SLSLSWI		Blue
SLSLWI		Purple
SLSWI		Magenta

Table 3: Multiple snow zone situations for a function (171) with $c=1/10$.

A closer look can be seen in figure 23.

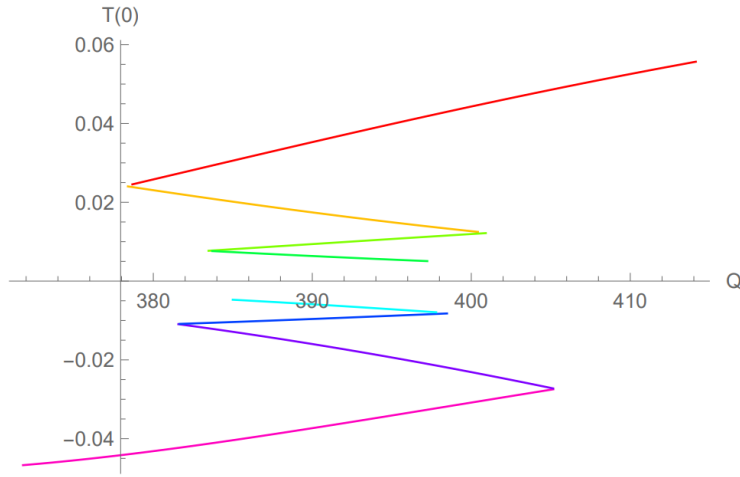


Figure 23: A segment of the bifurcation diagram in figure [22](#)

At a glance the dense, rapidly varying area looks like an error in computation. Even at the heights of 10 (5 on upper half circle) snow edges, 11 intervals on the continents, the bifurcation diagram is not complete. There could be just a couple more situations, or there could be an infinite amount. The calculations get more and more complicated as the number of unknown angles θ_s with a non-linear dependence increases. Before trying to find successive situations we will analyse the distribution of the snow zones.

Where the edges are situated in relation to each other, and the lengths of the land and snow intervals, is presented in figures [24](#) and [25](#), for the values of Q where a solution exists. We denote the snow edges $\theta_{s0}, \theta_{s1}, \dots$, on the upper half circle. The plots are the cases with the most edges (LSLSLSWI, SLSLSLWI). Plots for the other cases can be seen in appendix [A.4](#).

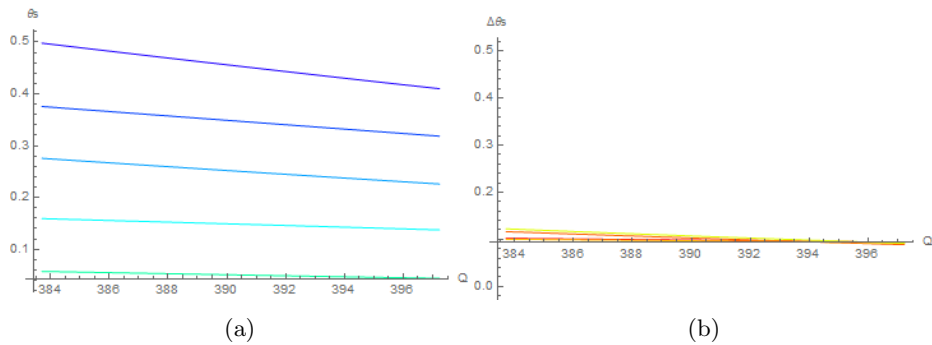


Figure 24: The angles $\theta_{s0}, \theta_{s1}, \dots$, in blues, and the differences $\theta_{s1} - \theta_{s0}, \dots$, in reds, for LSLSLSWI.

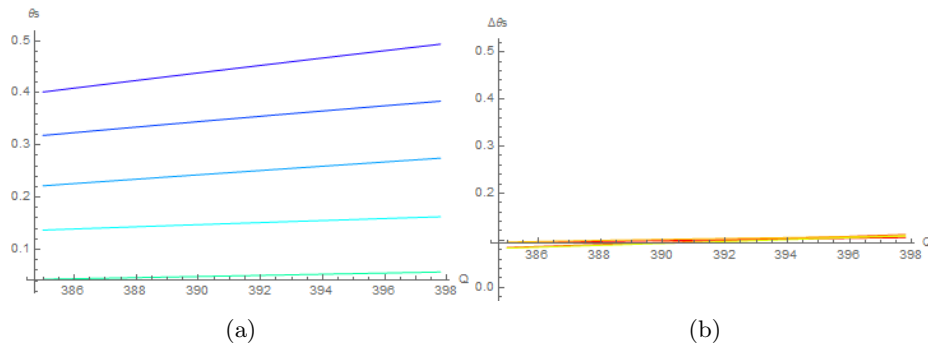


Figure 25: The angles $\theta_{s0}, \theta_{s1}, \dots$, in blues, and the differences $\theta_{s1} - \theta_{s0}, \dots$, in reds, for SLSLSLWI.

The snow edges for the solutions with *land* at the substellar point move closer to 0 with increasing Q . And, judging from the overlapping and approximately constant differences, the size of the snow/land intervals both remains the same for the different values of Q , and is of equal size to each other. The solutions with *snow* at the substellar point behaves in the same way, but in the opposite direction. The distribution of the zones is reminiscent of a waveform, with a set wavelength. Considering that the temperature is above zero for land and below for snow, that is precisely how the temperature distribution looks inside the continent. Temperature distributions are included in appendix [A.5](#). To further investigate this phenomenon, applying another method could be useful. The complicated computations along with a lack of confirmation of correctness makes solving for further situations less useful. Not to mention the stability testing of said solutions.

8 Additional analysis tool AUTO-07p

To proceed in our analysis of the multiple snow zones solutions we will use the *Continuation and bifurcation software for ordinary differential equations AUTO-07p*. A guide on how to install and run AUTO is included in appendix [A.6](#).

The energy balance model [\(28\)](#) is a partial differential equation, which AUTO has some methods of analysis for. But as the name suggests, it is both more suited to and more thorough at examining ordinary differential equations. To work around this, we can use a finite difference approximation as we did for the time dependent solution in section [5](#). Except now we only need to apply it to the **spatial** derivative.

The second derivative in space will as before be replaced by the centred difference

formula, but we will increase to the fourth order

$$T_{\theta\theta} = \frac{-T_{j-2}^n + 16T_{j-1}^n - 30T_j^n + 16T_{j+1}^n - T_{j+2}^n}{12d\theta^2}. \quad (172)$$

We do this because the computations will get very heavy, and to get any kinds of useful results we need a high level of accuracy. When substituted into the energy balance model (148) we get:

$$\gamma_i \partial_t T_j - \frac{-T_{j-2} + 16T_{j-1} - 30T_j + 16T_{j+1} - T_{j+2}}{12d\theta^2} + \beta_i T_j = h_{ij} \quad (173)$$

$$\partial_t T_j = \frac{1}{12\gamma_i d\theta^2} (-T_{j-2} + 16T_{j-1} - 30T_j + 16T_{j+1} - T_{j+2}) - \frac{\beta_i}{\gamma_i} T_j + \frac{1}{\gamma_i} h_{ij}^n \quad (174)$$

For the boundaries we use the fourth order centre difference, which requires the introduction of the *ghost points* T_{-1}^n , T_{-2}^n and T_{N+1}^n , T_{N+2}^n . Using the symmetry, we get when considering only the **half circle**

$$T_{-1}^n = T_1^n, \quad T_{-2}^n = T_2^n, \quad T_{N+1}^n = T_{N-1}^n, \quad T_{N+2}^n = T_{N-2}^n, \quad (175)$$

and the **full circle**

$$T_{-1}^n = T_{N-1}^n, \quad T_{-2}^n = T_{N-2}^n, \quad T_{N+1}^n = T_1^n, \quad T_{N+2}^n = T_2^n. \quad (176)$$

We must also update the expression binding the solutions on either side of the continent edge. Using the backward difference below the edge and the forward difference above, in the fourth order, we get for the upper edge of the continent

$$\begin{aligned} & D_1 \left(\frac{3T_{N_1-4}^n - 16T_{N_1-3}^n + 36T_{N_1-2}^n - 48T_{N_1-1}^n + 25T_{N_1}^n}{12d\theta} \right) \\ & = D_0 \left(\frac{-25T_{N_1}^n + 48T_{N_1+1}^n - 36T_{N_1+2}^n + 16T_{N_1+3}^n - 3T_{N_1+4}^n}{12d\theta} \right), \end{aligned} \quad (177)$$

$$\begin{aligned} T_{N_1}^n &= \frac{1}{25(D_1 + D_0)} (D_1(-3T_{N_1-4}^n + 16T_{N_1-3}^n - 36T_{N_1-2}^n + 48T_{N_1-1}^n) \\ &\quad + D_0(48T_{N_1+1}^n - 36T_{N_1+2}^n + 16T_{N_1+3}^n - 3T_{N_1+4}^n)). \end{aligned} \quad (178)$$

Of course, there is now the issue of the point $T_{N_1-1}^n$ depending on $T_{N_1+1}^n$, and $T_{N_1+1}^n$ depending on $T_{N_1-1}^n$. Crossing the threshold where the second derivative does not exist. We therefore use a custom stencil for sampled points for these two cases [10]. For $T_{N_1-1}^n$ we use a backward difference with +1 one point

$$T_{\theta\theta} = \frac{T_{N_1-5}^n - 6T_{N_1-4}^n + 14T_{N_1-3}^n - 4T_{N_1-2}^n - 15T_{N_1-1}^n + 10T_{N_1}^n}{12d\theta^2}, \quad (179)$$

and for $T_{N_1+1}^n$ we use a forward difference with -1 one point

$$T_{\theta\theta} = \frac{10T_{N_1}^n - 15T_{N_1+1}^n - 4T_{N_1+2}^n + 14T_{N_1+3}^n - 6T_{N_1+4}^n + T_{N_1+5}^n}{12d\theta^2}. \quad (180)$$

Both are of fourth order. For the **full circle** case we would have to do this for both the upper edge N_{1a} , and the lower edge N_{1b} . And as before, diffusivity is switched for the lower edge, $D_0 \leftrightarrow D_1$.

The ODE version of our PDE is then

$$\begin{aligned}
\partial_t T_j &= \frac{1}{12\gamma_i d\theta^2} (-T_{j-2} + 16T_{j-1} - 30T_j + 16T_{j+1} - T_{j+2}) - \frac{\beta_i}{\gamma_i} T_j + \frac{1}{\gamma_i} h_{ij}^n \\
\partial_t T_{N_1-1} &= \frac{1}{12\gamma_i d\theta^2} (T_{N_1-5}^n - 6T_{N_1-4}^n + 14T_{N_1-3}^n - 4T_{N_1-2}^n - 15T_{N_1-1}^n + 10T_{N_1}^n) \\
&\quad - \frac{\beta_i}{\gamma_i} T_j + \frac{1}{\gamma_i} h_{ij}^n \\
T_{N_1}^n &= \frac{1}{25(D_1 + D_0)} (D_1(-3T_{N_1-4}^n + 16T_{N_1-3}^n - 36T_{N_1-2}^n + 48T_{N_1-1}^n) \\
&\quad + D_0(48T_{N_1+1}^n - 36T_{N_1+2}^n + 16T_{N_1+3}^n - 3T_{N_1+4}^n)) \\
\partial_t T_{N_1+1} &= \frac{1}{12\gamma_i d\theta^2} (10T_{N_1}^n - 15T_{N_1+1}^n - 4T_{N_1+2}^n + 14T_{N_1+3}^n - 6T_{N_1+4}^n + T_{N_1+5}^n) \\
&\quad - \frac{\beta_i}{\gamma_i} T_j + \frac{1}{\gamma_i} h_{ij}^n \\
T_{-1}^n &= T_1^n \\
T_{N+1}^n &= T_{N-1}^n
\end{aligned} \tag{181}$$

for considering the **upper half circle**. This is the case we will by default be considering to maximise accuracy.

8.1 Implementation

The solutions found with AUTO continue the investigation of the case of one symmetric continent with $l = 1$ and $S(\theta)$ given by (171) with $c = 1/10$.

The first tests with auto was done with the original second order finite difference, but by switching to fourth order the computation was much faster. This is specifically since the fourth order accuracy let us use a larger DS (pseudo-arclength stepsize) in AUTO, while still being able follow the solution families. The results were still the same, so the figures presented will be from both cases. Letting AUTO generate the bifurcation diagram for us, we get for different amounts of points N the results in figures 26 and 27. The $N = 400$ case is shown side by side with the *Mathematica* solution in figure 28. From the new scaling of Q in AUTO, the substellar temperature $T(0)$ is plotted as a function of

$$q = \frac{\eta_i}{\gamma_i} = \frac{Q}{CT_0}, \tag{182}$$

a scaled Q. You will notice that some of the plots look very *messy*. This is a quirk of AUTO, where numerical errors can be interpreted as folds, resulting in an overabundance of labels.

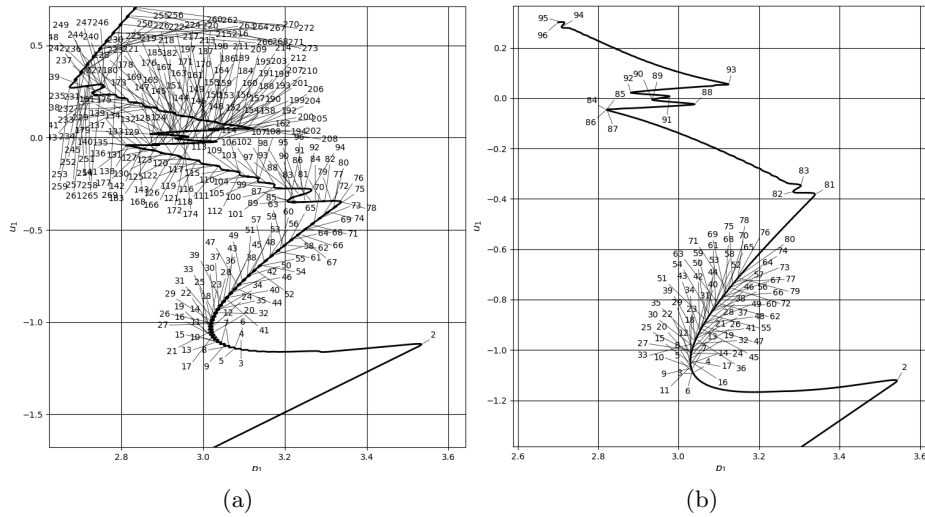


Figure 26: The AUTO bifurcation diagram for (a) $N = 100$. (b) $N = 200$.

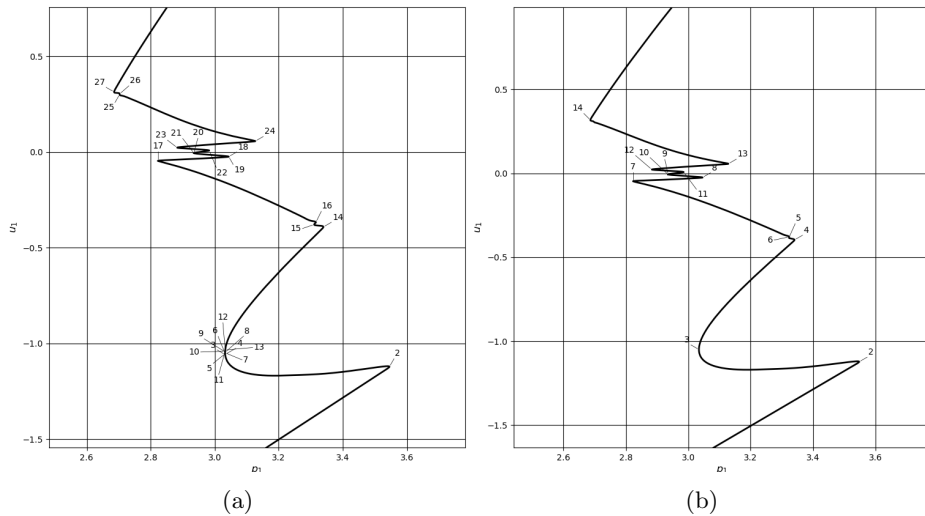


Figure 27: The AUTO bifurcation diagram for (a) $N = 300$. (b) $N = 400$.

The second thing we notice is that the shape of the bifurcation closely resembles what we saw in section [7.2.2](#), and we have gotten verification that the possible numerical *error* that was observed seems to be actual stationary solutions! We will now see what we can gather about this specific part of the diagram by using AUTO.

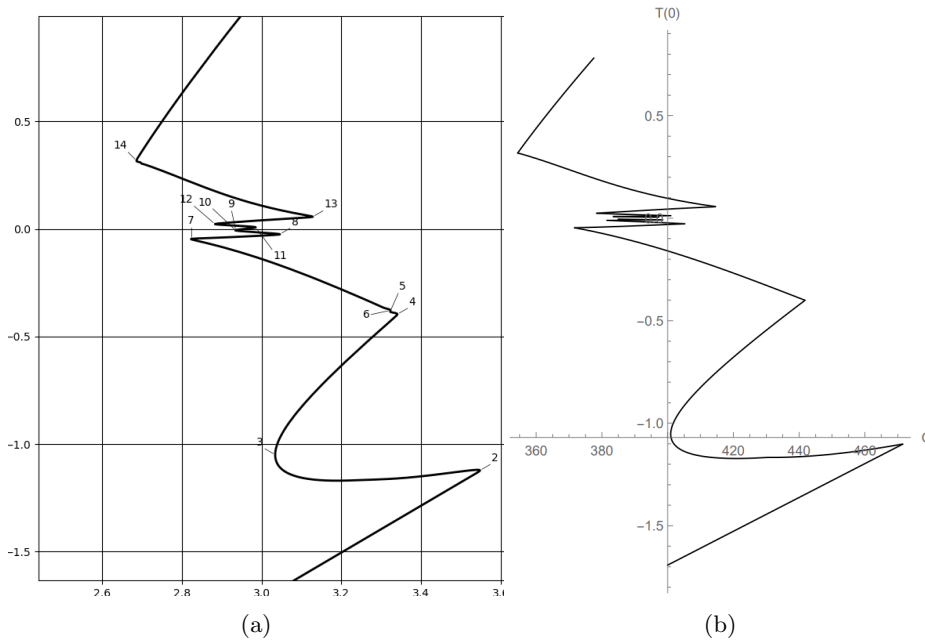


Figure 28: (a) The AUTO bifurcation diagram for $N = 400$. (b) The *Mathematica* solution. For comparison $q = Q/132$, (182).

The smaller the number of grid points, or resolution, the more jagged the bifurcation diagram becomes. The labels denote folds, so for the low resolution cases the plots get pretty messy with fold labels. Seeing as the labels disappear with increasing resolution, we can attribute them to numerical errors in computation. At the highest resolution there is still some probable error to be seen at labels 4,5,6, which will presumably disappear with a further increase. Note that the lack of continuation from points 96 in $N = 200$ is simply a termination of calculation to shorten the duration, which will henceforth be used for the more heavy cases.

Even still, all the cases shown show the same number of multiple ice edge solutions. Five lines sandwiched between the two *one-snow-zone* solutions. The $N = 400$ case has about 64 sample points inside the continent, and should definitely be able to capture a wavelength with 3 peaks and more. If resolution does nothing, something else must have a part in determining the amount. We need to consider the hyperbolic tangent function for the albedo (157) that we are using in our finite difference approximation. We could try increasing the sharpness of the hyperbolic tangent approximation to be closer to the step function.

8.2 Albedo function sharpness

Letting c_{\tanh} denote the constant which was formerly set to 100 in the hyperbolic tangent function for the albedo (157), we now try the case of

$$c_{\tanh} = 200 \tag{183}$$

Running AUTO again for the case of $N = 300$ we get the result shown in figure 29. With a close up of the multiple snow zone area in figure 30, compared to the Mathematica solution in figure 31. The obvious mess lets us know that the sharpness of the hyperbolic tangent function also makes the diagram more jagged. We would require an even higher number of discretization points to make this case smooth.

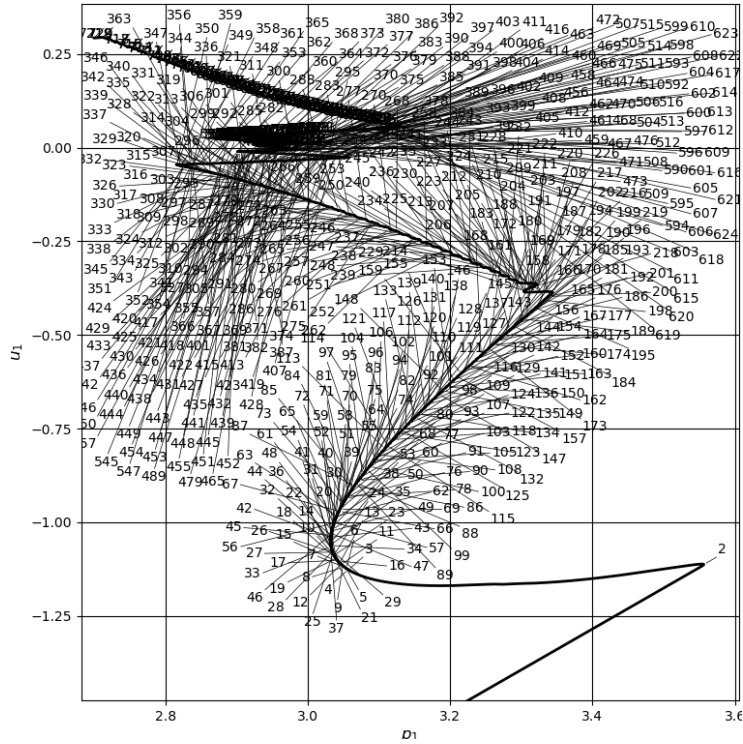


Figure 29: The AUTO bifurcation diagram for $N = 300$, $c_{\tanh} = 200$.

We can see that now there are more folds visible, counting 7 lines in between. Presumably, increasing c_{\tanh} further would gradually reveal more and more folds. Using the exact step function makes it very hard for AUTO to detect the sudden sharp turns of the bifurcation diagram, the DS has to be so small that even getting past the first fold becomes a big hurdle.

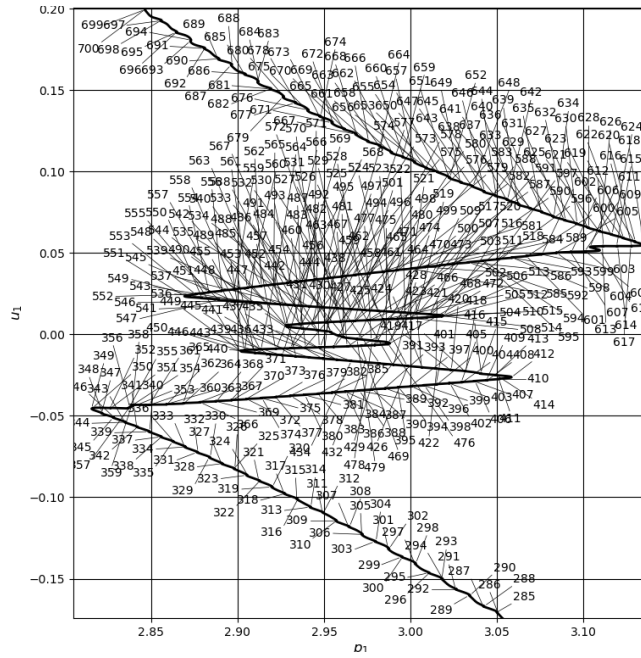


Figure 30: The multiple snow zone solutions for $N = 300$, $c_{\tanh} = 200$.

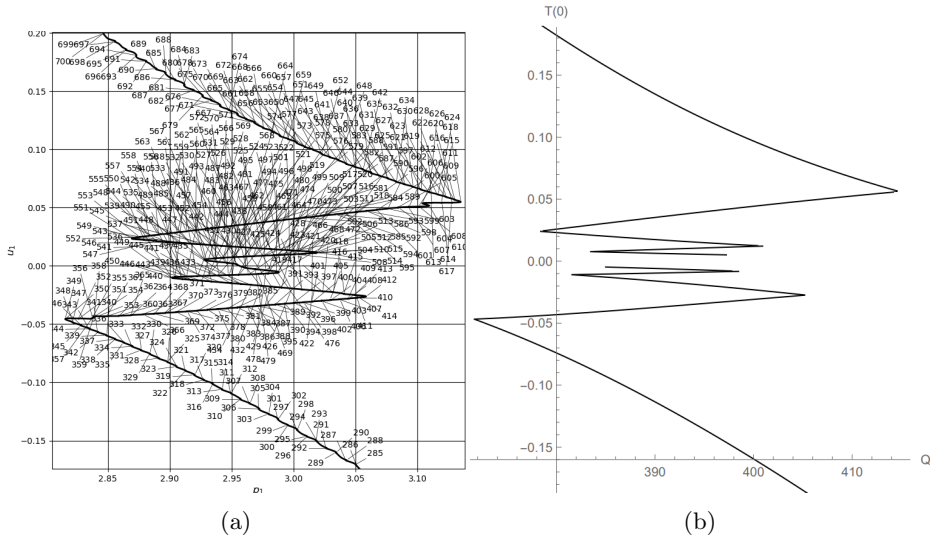


Figure 31: (a) The AUTO bifurcation diagram for $N = 400$. (b) The *Mathematica* solution. For comparison $q = Q/132$, [\[182\]](#).

One thing we can conclude from this investigation is that an exact step function seems to be a requirement for the full, possibly infinite, range of analytic solutions to appear. At least, the sharpness of the jump in albedo must be sufficiently sharp for any folds beyond just a couple of snow intervals to appear. On an actual planet like earth, we would assume that there will be at least a certain gradient in the transition. This could mean that these states are even less likely to appear naturally than the other states previously found unstable. AUTO provides a stability analysis for the points in the diagram, which we will consult to confirm the bistability.

8.3 Stability of multiple snow zones solutions

In AUTO, the *sign* of PT, the point number, in the `fort.7` file is used to indicate stability. The sign `-` is stable, and `+` is unstable. Investigating the files for each run we can then determine which solutions are stable. To read the file, pay attention to

- PT, `-` if stable, `+` if unstable
- LAB, figure fold labels
- $U(1)$, substellar temperature, plotted against q in the bifurcation diagrams
- $PAR(1)$, scaled Q value, q (182).

Excerpts of the `fort.7` file for $N = 400$ with $c_{tanh} = 100$, at transitions between `+` and `-`, can be seen in figure 32 and 33. A plot of the stable and unstable zones based on the `fort.7` data is shown in figure 34. The areas the labels refer to can be seen in figure 28.

	PT	TY	LAB	PAR(1)	L2-NORM	U(1)	
(a)	0	0	0	0.0000000000E+000	9.9844198227E+001	-4.9922099113E+000	
	1	-1	9	1	9.9842217894E+001	-4.9920993497E+000	
	1	-2	0	0	9.9840733310E+001	-4.9920162675E+000	
	1	-3	0	0			
(b)	1	-6990	2	2	3.5473258948E+000	3.2107989034E+001	-1.1223906928E+000
	1	6991	0	0	3.5472389495E+000	3.2102545544E+001	-1.1217486566E+000
	1	6992	0	0	3.5469281656E+000	3.2099036485E+001	-1.1211323699E+000
(c)	1	7797	2	3	3.0341988754E+000	3.4093578604E+001	-1.0495398169E+000
	1	-7798	0	0	3.0342001344E+000	3.4086933699E+001	-1.0491918971E+000
	1	-7799	0	0	3.0342038024E+000	3.4080277069E+001	-1.0488429560E+000

Figure 32: The `fort.7` file for $N = 400$, $c_{tanh} = 100$, at the (a) $Q = 0$ area. (b) transition at label LAB=2. (c) transition at label LAB=3.

1	-9608	2	4	3.3402426552E+000	2.1229139755E+001	-3.9657917924E-001
1	9609	0	0	3.3401871090E+000	2.1227453817E+001	-3.9579771886E-001
1	9610	0	0	3.3399856851E+000	2.1228759510E+001	-3.9497489733E-001

(a)

1	9660	2	5	3.3224193057E+000	2.1579354450E+001	-3.8334680269E-001
1	-9661	0	0	3.3224529900E+000	2.1575844537E+001	-3.8263062842E-001
1	-9662	0	0	3.3225284956E+000	2.1571574527E+001	-3.8197164045E-001
1	-9663	0	0	3.3226227659E+000	2.1566981219E+001	-3.8134089498E-001
1	-9664	0	0	3.3227221427E+000	2.1562313471E+001	-3.8071652125E-001
1	-9665	0	0	3.3228151075E+000	2.1557777868E+001	-3.8007884796E-001
1	-9666	0	0	3.3228873327E+000	2.1553632398E+001	-3.7940592396E-001
1	-9667	2	6	3.3229149543E+000	2.1550593673E+001	-3.7874461252E-001
1	9668	0	0	3.3228617944E+000	2.1548871147E+001	-3.7792717264E-001

(b)

1	3097	2	14	2.6866442924E+000	3.5303705853E+001	3.1727190195E-001
1	-3098	0	0	2.6866444672E+000	3.5303316752E+001	3.1733426635E-001
1	-3099	0	0	2.6866449822E+000	3.5302923579E+001	3.1739644975E-001

(c)

Figure 33: The fort.7 file for $N = 400$, $c_{tanh} = 100$, at the (d) transition at label LAB=4. (e) transition at labels LAB=5,6. (f) transition at label LAB=14.

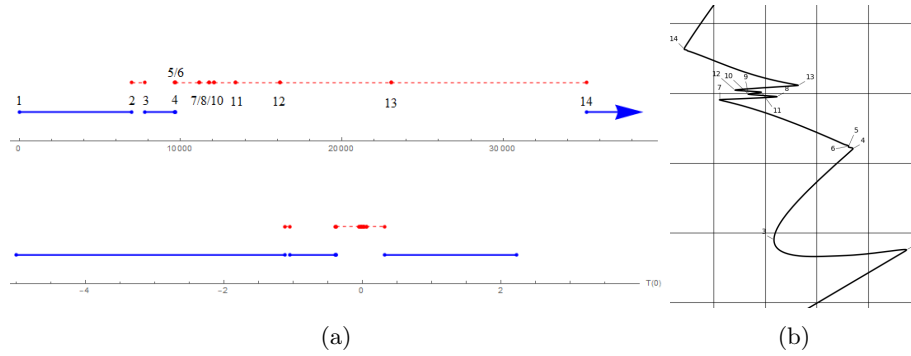


Figure 34: The stability data from the fort.7 file for $N = 400$, $c_{tanh} = 100$. Red... unstable, Blue - stable. Upper (a) by data points, lower (a) by $T(0)$.

Before reaching the first fold, and after the last fold, we have stability. But also in the area between label 3 and 4. There is a small zone of stability between 5 and 6, as can be seen in [33\(e\)](#), but this is most likely a numerical error. As expected, the multiple snow zone solutions seem to all be unstable. The same goes for the middle situations previously found as unstable in section [6.1](#), while the snowball(SI), ice edge (LWI) and *upper* snow edge solution (SWI) are still stable.

The overall stability is the same as before, in the sense that only the SI, LWI and SWI solutions are stable in the area with multiple solutions. In the interval with a SWI solution we do not have bistability, but instead three possible stable solutions.

9 Stability and feedback discussion

As has been observed, the introduction of continents and its consequence of including several feedbacks, not just the ice-albedo but an additional snow-albedo feedback inside a separated area, has resulted in an increase in the number of possible states of the system for a single value of the solar constant Q in certain areas. It was also found that less difference in incoming radiation over the surface resulted in an occurrence of even more possible states, with more feedback areas. By examining the bifurcation diagrams we can see how the now existing *intermediary* stable solutions could change the dynamic of having sudden tipping points in varying the solar constant, to a more gradual decrease. The initial simple ice-albedo model had stable solutions that were far removed in the values of their temperature distributions. In changing Q across the threshold of existing solutions for either, there would be a large jump or tipping point.

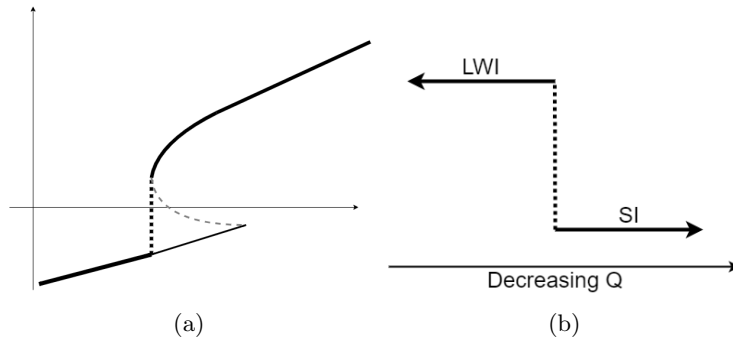


Figure 35: Drop in stationary solution from LWI to SI, no continents.

From the intermediary stationary solutions resulting from the additional feedback, the gap is split. If these solutions are placed in such a way that the stationary solutions are consecutive along values of Q , they could serve as a middle step between the upper and lower stable solutions. We get *more* tipping points, but each drop in temperature is smaller, *less drastic*. For our parameters, this seems to be the case for a continent shifted towards the pole, but not too far removed from the equator. Diagrams can be viewed in appendix [A.2](#) and [A.3](#). Considering the case of one continent with $l = \pi/4$, $\epsilon = 0.41$ for instance, there is a clear middle "step" in the drop of.

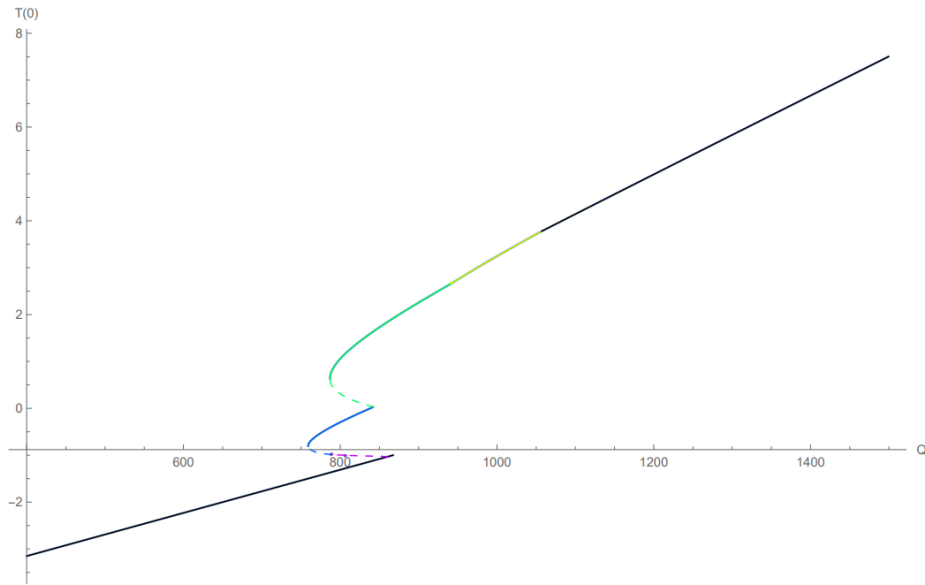


Figure 36: The bifurcation diagram for $\epsilon = 0.41$.

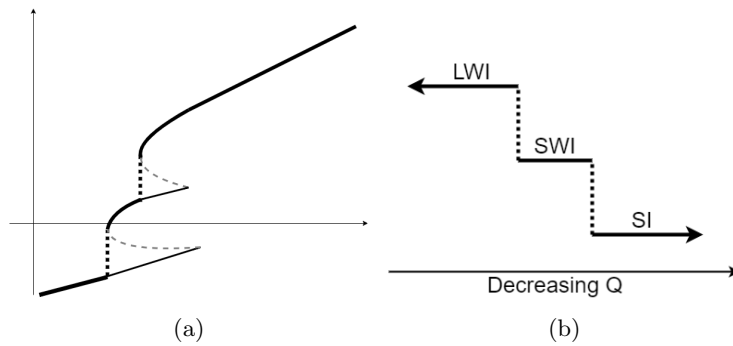


Figure 37: Drop in stationary solution from LWI, to SWI, to SI, one continent.

Building on a simple model and introducing more feedbacks could be something that avoids a large drop in state temperature, and instead causes a small step by step drop off. Removing the possibility of an abrupt transition to an ice covered planet with a small decrease in Q that was initially seen in the simplest North-like case.

The results of varying the radiation distribution function showed that a less concentrated $S(\theta)$ causes more intermediary solutions which, while unlikely to be relevant themselves for a realistic system, suggest that a planet with a more evenly distributed radiation, from rotation or otherwise, is more inclined to exhibit a bifurcation with several possible simultaneous states. This is in tune

with the results by Checlair^[9], in which tidally locked planets will not necessarily exhibit even the snowball bifurcation in a realistic setting. We also here see a connection between number of folds and more areas of feedback.

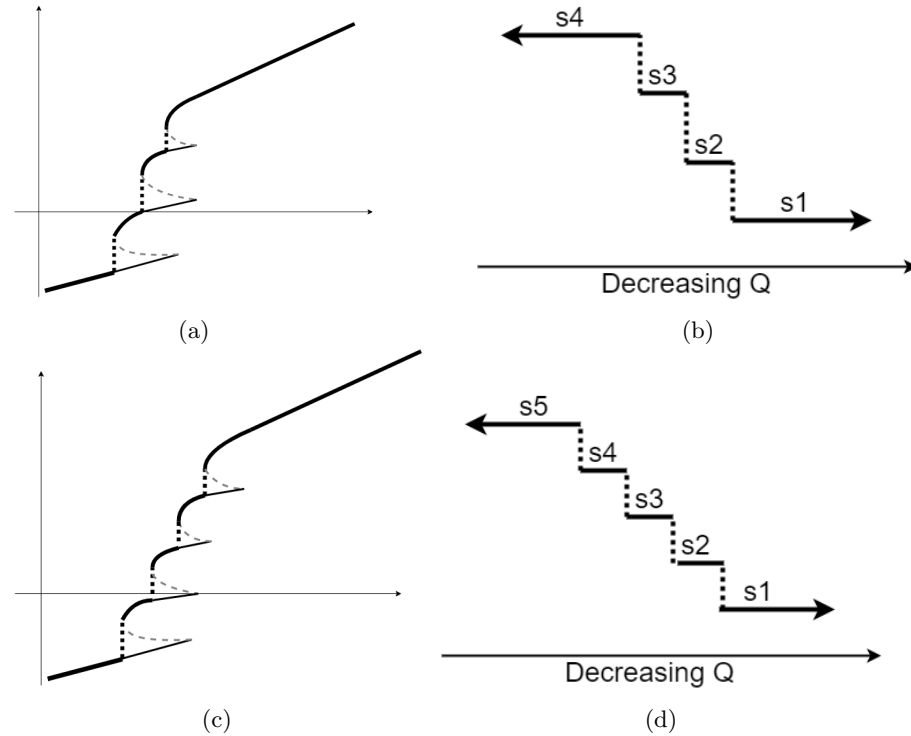


Figure 38: Possible structure of a drop in stationary solutions s_1 - s_4/s_5 .

Considering the earth, it has a larger concentration of landmass on the upper hemisphere, which would fit with a moderately pole shifted continent for which we have observed steps, it rotates, which gives a less concentrated $S(\theta)$, and it will have a myriad of feedbacks based on its actual complexity. Larger, more complex climate models consider a wide range of feedbacks. Our result gives an idea that the effects of those feedback mechanisms could contribute to the models having a more continuous range of stationary solutions for different solar constants.

10 Symmetry breaking

We have in cases of symmetric continent distribution restricted to solutions that are symmetric around $\theta = 0$ in finding the stationary solutions. If there was only *one* solution to the problem there would be no question about if a solution on the other interval maps to a given solution on the other interval, as there

is only one solution. This meaning if $T(\theta)$ is a solution to the energy balance model

$$C\partial_t T - D_i\partial_{\theta\theta}T + BT = QS(\theta)(1 - a_i(T)) - A, \quad (184)$$

and $T(-\theta)$ is also a solution, then $T(\theta) = T(-\theta)$ because there is only one solution in the solution space.

But, since we have seen there can be *three*, *five*, and even *ten* and above possible solutions for certain values of Q , this is not necessarily true. There could be solutions where $T(\theta) \neq T(-\theta)$, where one solution maps into one of the other possible solutions across $\theta = 0$. If there were two possible solutions $T_1(\theta)$ and $T_2(\theta)$ we could have

$$T(\theta) = T_1(\theta), \quad T(-\theta) = T_2(-\theta) \quad (185)$$

If so the ice and snow edges would have different positions on the upper and lower half circle of the planet. We would have symmetry breaking.

During the investigation of the effects of continent size and the multiple snow zone solutions, the full circle was included in the calculations along side the upper half circle consideration. Both in *Mathematica* and *Auto-07p*. In these calculations, there was no obvious discrepancy to be observed in the results. A symmetry breaking solution could still be possible, but no such situation was discovered.

11 Conclusion

Introducing continents to the circle model has let us investigate what effects they can have on the bistability of the system and the stationary states available, based on their configuration and the incoming radiation.

Continents were introduced to the circle model (23) by letting the heat conductivity $K(\theta)$ take different constant values in different regions i , along with having different sets of albedos $a_i(T)$. The transitional temperature was also given different values for the ocean ice and the continent snow. These additions created a more complex partial differential equation, but it simply had to be split into more segments for a boundary formulation solution. The general solution method for stationary solutions was to use the segments and boundary conditions that applied in the general formulae (82), (83) to get the *equations*, and the solved equations and the general integral identity (81) to get the *solutions*.

We considered the case of one symmetric continent of a set size, solved the boundary equations to find stationary solutions, and constructed the bifurcation diagram 3. It was found that there were up to 5 possible solutions, 3 in the range $Q_a < Q < Q_c$ and 5 in range the $Q_c < Q < Q_b$.

Designing the finite difference code to work with and without continents gave us the scheme (156). It was tested against the pseudo-spectral solution, (135) with (137), for the case of no continents giving the result in figure 6, and then with an artificial source (163), giving the result in figure 7. Both validated the

implementation. Checking its behaviour at a stationary solution, as seen in [8](#), also strengthened our faith in both the finite difference code and the analytical solutions.

The finite difference scheme was used to test the stability of the stationary solutions for one symmetric continent. All the solutions between the snowball solution at the bottom and the ice cap solution at the top were unstable, except for the upper snow edge solution. The unstable solutions transitioned to the two exterior, seemingly stable, solutions depending on the direction of perturbation. This was shown in figures [9](#) - [13](#). With three possible stable solutions, there was *tristability* in the small area containing the intermediary stable solution.

Varying the size and position of one continent we found the relations in figures [15](#), [16](#) and [17](#), [18](#) for the dimensions of the bifurcation area. We concluded that the bifurcation area was largest, while still retaining its interesting qualities, with $\epsilon \approx 0$ and $l \approx 1$. A large continent symmetric around the equator.

Varying the radiation distribution function $S(\theta)$ from the "tent" shaped ([29](#)) to a North-like slope ([171](#)) with $c = 1/2$ we discovered new possible situations where the assumption of absolute decrease of temperature from the substellar point ([104](#)) was no longer valid. A snow edge with snow on the innermost part of the continent and a situation with three disjoint segments of snow, which gives the bifurcation diagram in figures [19](#) and [20](#). Flattening the slope further with $c = 1/10$ we found several, seemingly endless, multiple snow zone solutions. Giving the rapidly folding bifurcation diagram seen in figures [22](#) and [23](#). By analysing the placements of the snow edges for the areas of Q where the solutions exist, plotted in figures [24](#) and [25](#), we found that the size of the snow/land intervals both remains the approximately same for the different values of Q , and of equal size to each other. The positions all moving to or from the substellar point, depending on if the situation has land or snow at the equator. The temperature distribution thus forms a wave shape on the continent, propagating with Q .

Using Auto-07p we replicated the bifurcation diagram with multiple snow zones, in figure [28](#), verifying the existence of these solutions. Although, the number of folds were less than we found analytically. By increasing the sharpness of the hyperbolic tangent approximation to the albedo ([157](#)) we observed an increase in the amounts of folds. Expecting that a realistic situation would have at least some gradient in the transition, the zones would be very unlikely. At least a large number of them. We could also see from AUTOs stability feature that the multiple snow zone solutions were predictably unstable, while the same situations as previously were stable. Those three being the snowball, ice edge and snow cover solutions.

In conclusion, the $S(\theta)$ variation showed that a less concentrated $S(\theta)$ causes more intermediary solutions which suggest that a planet with a more evenly distributed radiation, from rotation or other factors, is more inclined to have several possible simultaneous states, and showed a link between the amount of folds and more areas of feedback.

Studying the shapes and stability properties of the bifurcation diagram for different continent placements, we found cases where an intermediary stable solu-

tion was situated in a way that the stationary solutions were consecutive along values of Q , and we had a "step" between the tipping point and the ice planet solution. This suggest that with introduction of more feedback mechanisms we get more tipping points, but each drop in temperature is less drastic. Resulting in a more gradual step by step process, and removing the possibility of an abrupt transition to an ice covered planet with a small decrease in Q , that was initially seen in the simplest North-like case.

The model is overall quite simple, especially considering the complexity of climate, and has several limitations. The only surface parameters affecting the outward energy flux is the ice and snow edge positions, and the atmosphere phenomena are all simply parameterized by surface temperature with assumed homogeneous cloud cover. Spatial heat transport is determined by diffusion with a piecewise constant thermal diffusivity, and we assume a homogeneous heat capacity for the planet. We use a time averaged incoming solar radiation, and this and our limited interval of consideration means we are constrained to a certain time scale. We also assume symmetry for the solutions in symmetric cases. When solving with the full circle, no signs of symmetry breaking were discovered for the symmetric configurations. It is still possible that such solutions exist.

We have observed how an introduction of continents changed the bistability, and how varying the placement and the radiation distribution function affected the bifurcation area's dimension and shape. We found by considering these changes, and their stability properties, that increasing the number of feedbacks could possibly have an effect on mitigating the temperature steady state drop off. Although we derived a simple energy balance model on a circle, that we could actually solve analytically with boundary formulations due to linearity when not crossing critical points, we have found some surprisingly complicated results. While also giving a satisfactory description of the phenomena of interest, although there are limitations to its accuracy.

A Appendix

A.1 Python DFT

We will be implementing the pseudo-spectral code in Python. To be able to use Python's DFT to approximate (143) we must find the transformation between the conventions. Python (numpy) convention for DFT is

$$\begin{aligned} u_r &= \sum_{s=0}^{n-1} v_s e^{-i2\pi \frac{rs}{n}}, \quad r = 0, \dots, n-1 \quad (DFT) \\ v_s &= \frac{1}{n} \sum_{r=0}^{n-1} u_r e^{i2\pi \frac{rs}{n}}, \quad s = 0, \dots, n-1 \quad (IDFT) \end{aligned} \quad (186)$$

To begin transforming (143) into (186), we shift the indices

$$\begin{aligned} r &= N + j, \\ s &= N + l. \end{aligned} \quad (187)$$

When substituted into (143) this gives

$$\begin{aligned} F_{s-N} &= \frac{\Delta x}{\sqrt{2\pi}} \sum_{r=0}^{2N-1} f_{r-N} e^{i\pi \frac{(r-N)(s-N)}{N}}, \\ f_{r-N} &= \frac{\Delta \lambda}{\sqrt{2\pi}} \sum_{s=0}^{2N-1} F_{s-N} e^{-i\pi \frac{(r-N)(s-N)}{N}}. \end{aligned} \quad (188)$$

We have

$$e^{i\pi \frac{(r-N)(s-N)}{N}} = e^{-i\pi r} e^{-i\pi s} e^{i\pi N} e^{i\pi \frac{rs}{N}}, \quad (189)$$

and we introduce the scaling

$$\begin{aligned} F_{s-N} &= \alpha_s v_s, \\ f_{r-N} &= \beta_r u_r, \end{aligned} \quad (190)$$

which when substituted into (190) then gives

$$\begin{aligned}
\alpha_s v_s &= \frac{\Delta x}{\sqrt{2\pi}} \sum_{r=0}^{2N-1} \beta_r u_r e^{-i\pi r} e^{-i\pi s} e^{i\pi N} e^{i\pi \frac{rs}{N}} \\
\beta_r u_r &= \frac{\Delta \lambda}{\sqrt{2\pi}} \sum_{s=0}^{2N-1} \alpha_s v_s e^{i\pi r} e^{i\pi s} e^{-i\pi N} e^{-i\pi \frac{rs}{N}} \\
&\quad \Downarrow \\
v_s &= \frac{\Delta x}{\sqrt{2\pi}} \sum_{r=0}^{2N-1} \frac{\beta_r}{\alpha_s} u_r e^{-i\pi r} e^{-i\pi s} e^{i\pi N} e^{i\pi \frac{rs}{N}} \\
u_r &= \frac{\Delta \lambda}{\sqrt{2\pi}} \sum_{s=0}^{2N-1} \frac{\alpha_s}{\beta_r} v_s e^{i\pi r} e^{i\pi s} e^{-i\pi N} e^{-i\pi \frac{rs}{N}}
\end{aligned} \tag{191}$$

we must choose α_s , β_r and n/N in such a way as to get these expressions on the form (186). We choose

$$\begin{aligned}
\alpha_s &= \alpha_0 e^{-i\pi s} \\
\beta_r &= \beta_0 e^{i\pi r} e^{-i\pi N} \\
n &= 2N
\end{aligned} \tag{192}$$

and must have

$$\begin{aligned}
\frac{\Delta x}{\sqrt{2\pi}} \frac{\beta_0}{\alpha_0} &= \frac{1}{2N} \\
\frac{\Delta \lambda}{\sqrt{2\pi}} \frac{\alpha_0}{\beta_0} &= 1
\end{aligned} \tag{193}$$

using (144) we can see that only need to impose one. Considering the first fraction and choosing

$$\begin{aligned}
\alpha_0 &= \Delta x \frac{\sqrt{2N}}{\sqrt{\pi}} \\
\beta_0 &= 1
\end{aligned} \tag{194}$$

we get the transformations

$$\begin{aligned}
v_s &= \frac{1}{\Delta x} \frac{\sqrt{\pi}}{\sqrt{2N}} e^{i\pi s} F_{s-N}, \quad s = 0, \dots, n-1 \\
u_r &= e^{-i\pi r} e^{i\pi N} f_{r-N}, \quad r = 0, \dots, n-1
\end{aligned} \tag{195}$$

$$\begin{aligned}
F_l &= \Delta x \frac{\sqrt{2N}}{\sqrt{\pi}} e^{-i\pi(N+l)} v_{N+l}, \quad l = -N, \dots, N-1 \\
f_j &= e^{i\pi(N+j)} e^{-i\pi N} u_{N+j}, \quad j = -N, \dots, N-1
\end{aligned} \tag{196}$$

where the python DFT corresponds to the IDFT, and vice versa.

A.2 Symmetric continent size variation

Bifurcation diagrams from the variation of size l for one symmetric continent, using the radiation distribution (29). The colour coding is as follows:

LWI	ice cap	Red
LSWI	ice and snow edge	Green
SWI	snow cover	Cyan
LSI	ice cover	Blue
SI	snowball	Purple

Stable
 Unstable

Selected cases for l is shown in figures (39) - (47).

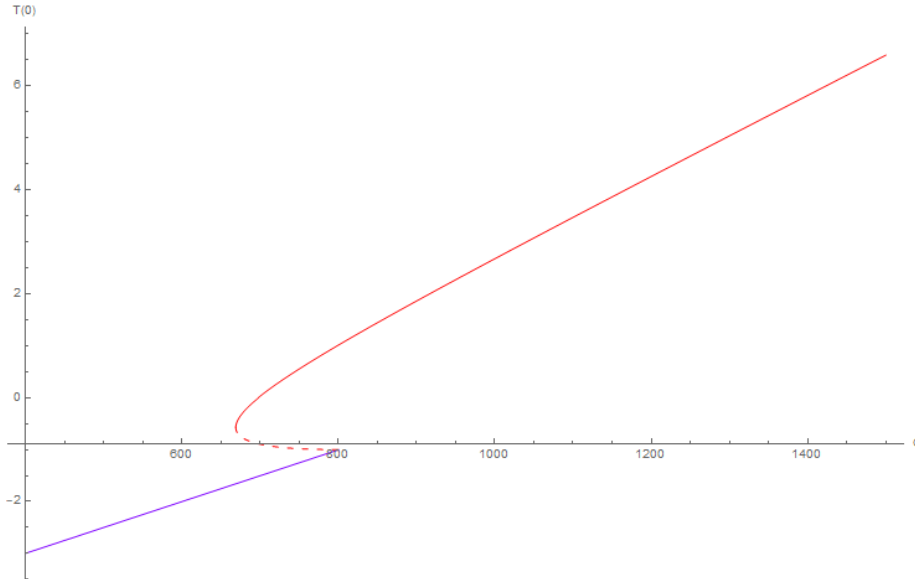


Figure 39: The bifurcation diagram for $l = 0$. No continent.

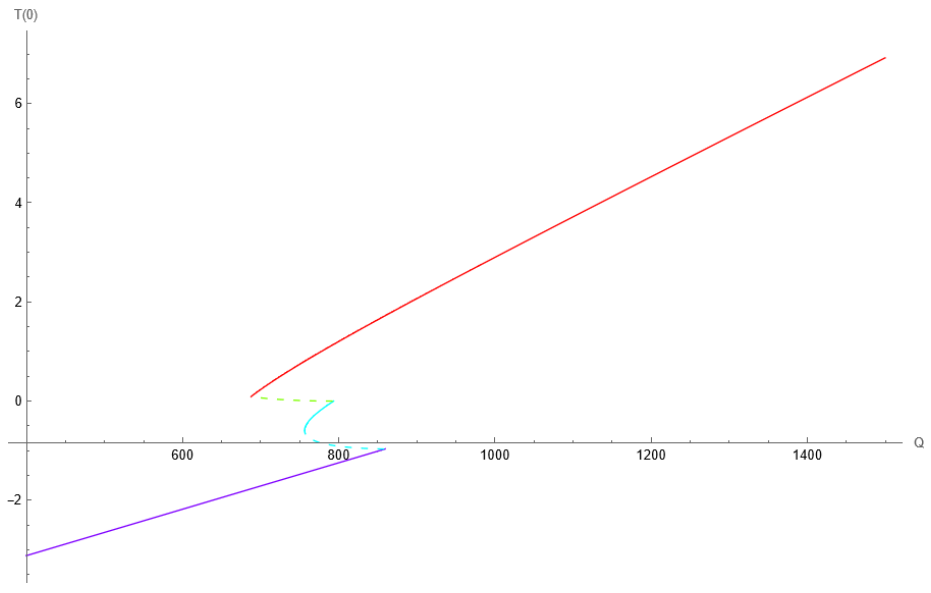


Figure 40: The bifurcation diagram for $l = 0.2$.

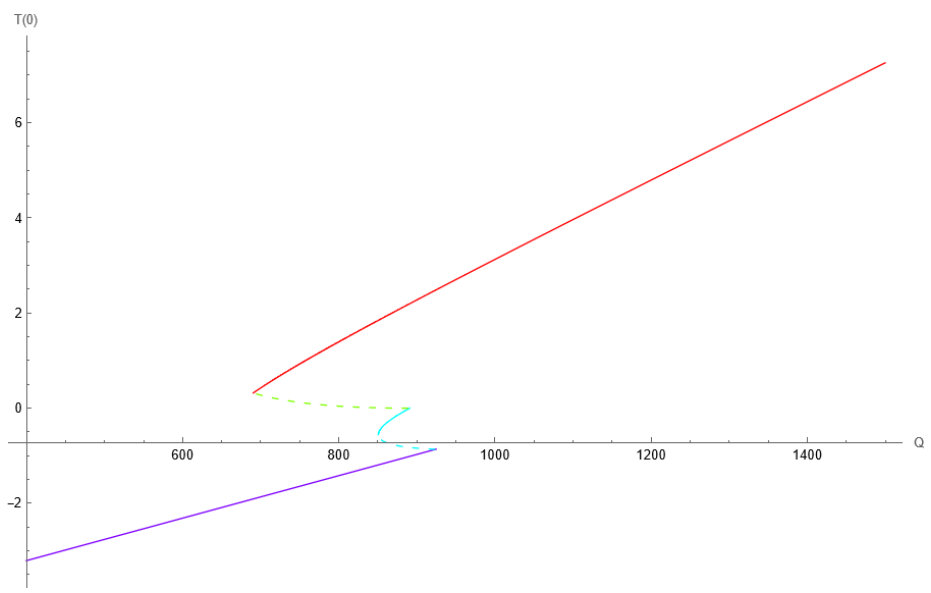


Figure 41: The bifurcation diagram for $l = 0.4$.

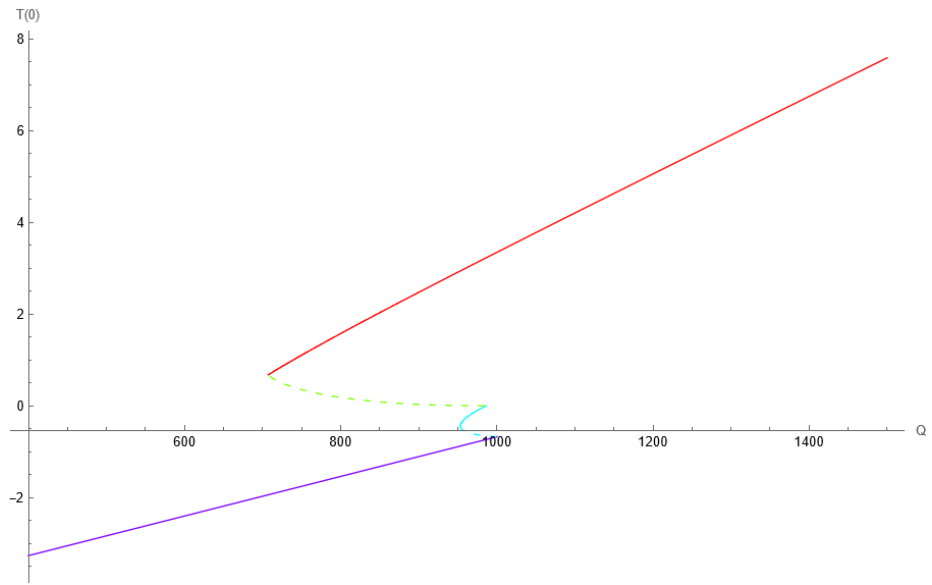


Figure 42: The bifurcation diagram for $l = 0.6$.

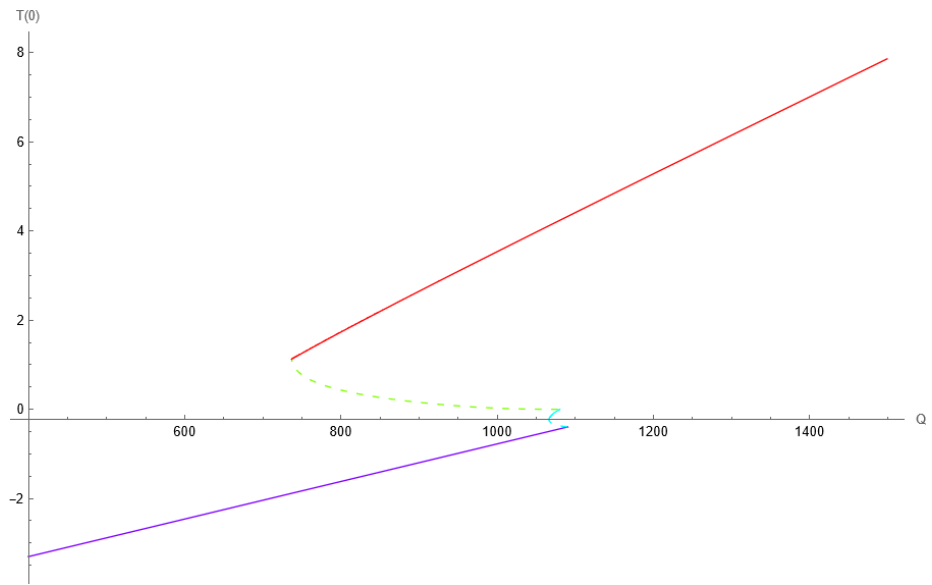


Figure 43: The bifurcation diagram for $l = 0.8$.

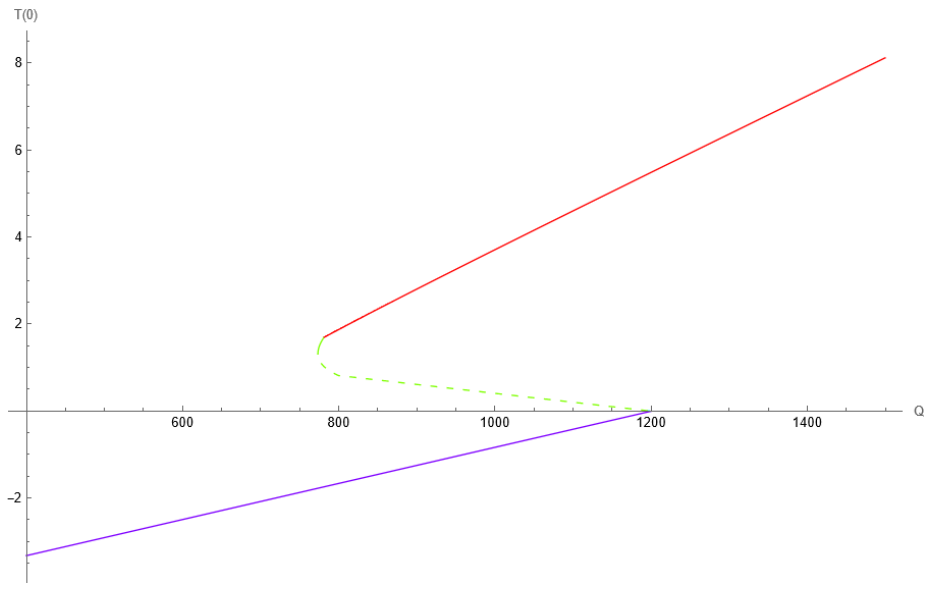


Figure 44: The bifurcation diagram for $l = 1$.

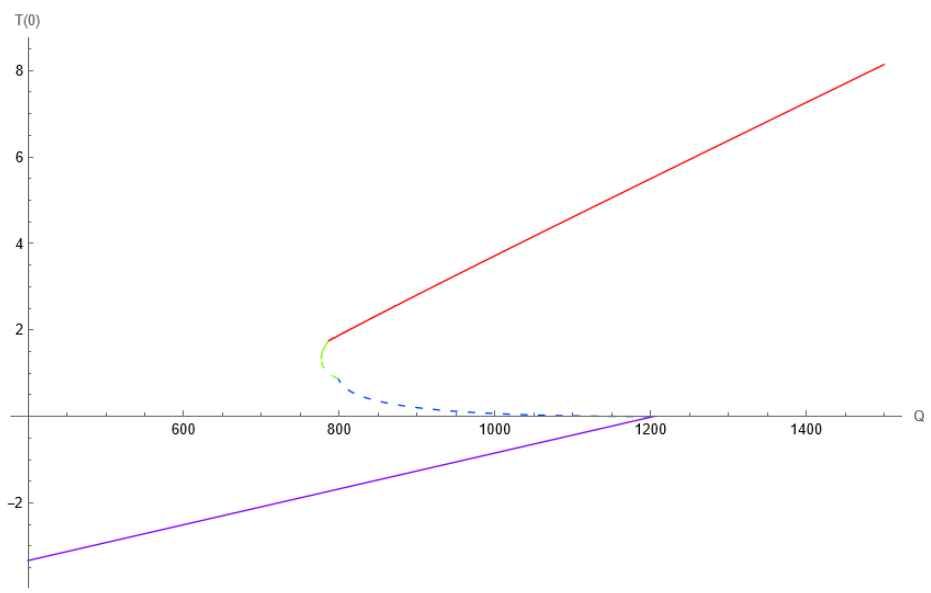


Figure 45: The bifurcation diagram for $l = 1.02$.

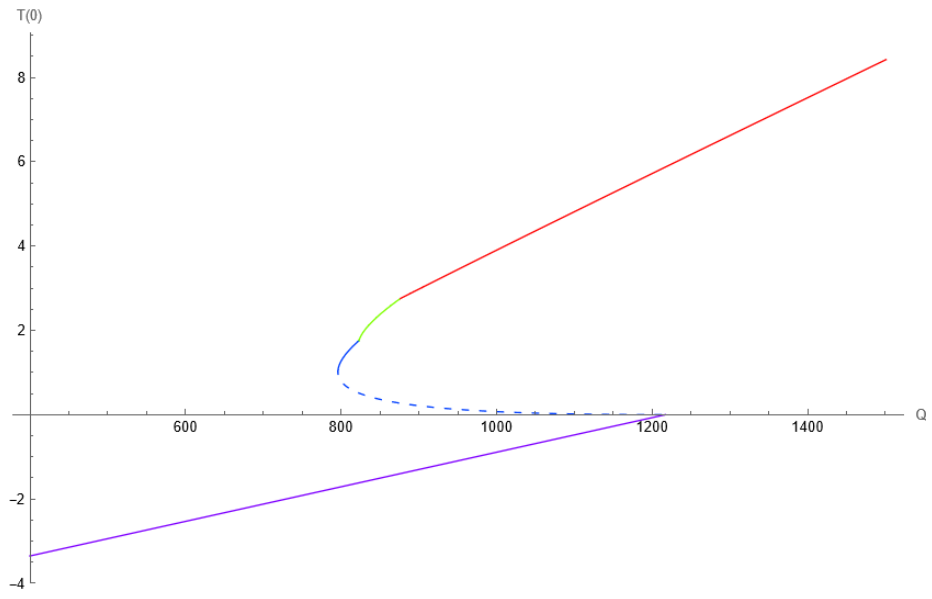


Figure 46: The bifurcation diagram for $l = 1.3$.

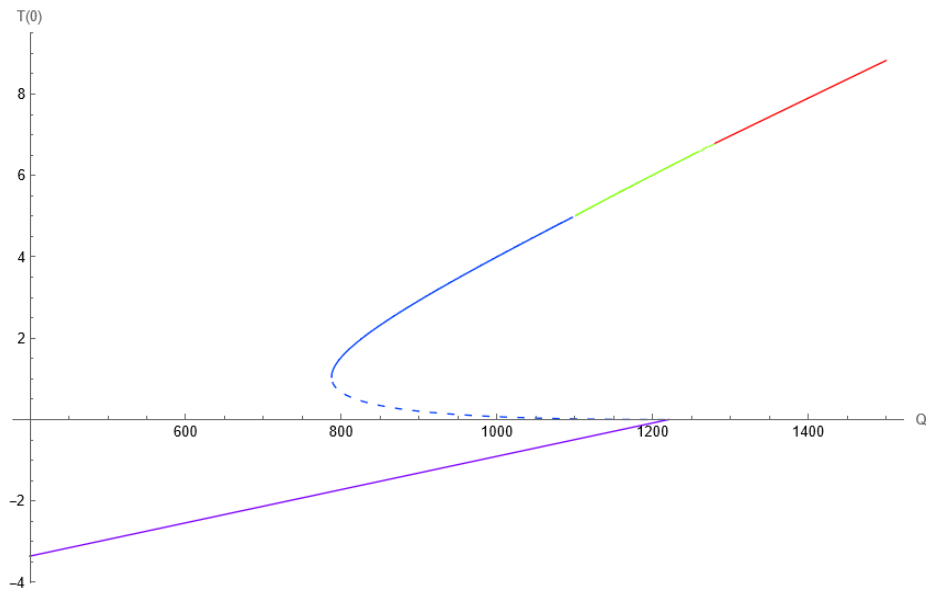


Figure 47: The bifurcation diagram for $l = 2$.

A.3 Continent of set size position variation

Bifurcation diagrams from the variation of position ϵ for one continent, using the radiation distribution (29). The colour coding is as follows:

IWLWI	Black
IWSLSWI	Red
IWSWI	Orange
IWLSWI	Yellow
IWLSI	Green
IWSLSI	Cyan
IWSI	Blue
IWISI	Purple
ISI	Black

Selected cases for ϵ is shown in figures (48) - (55).

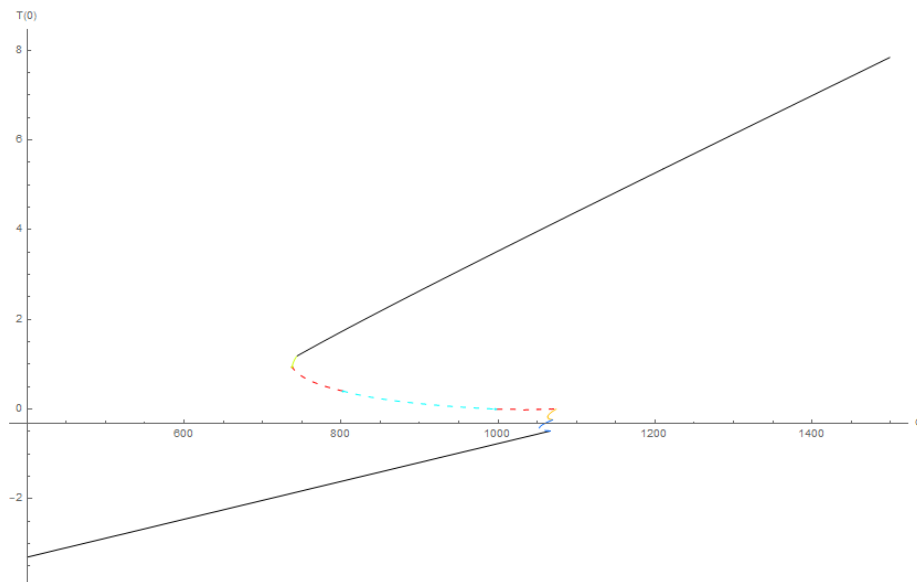


Figure 48: The bifurcation diagram for $\epsilon = 0.02$.

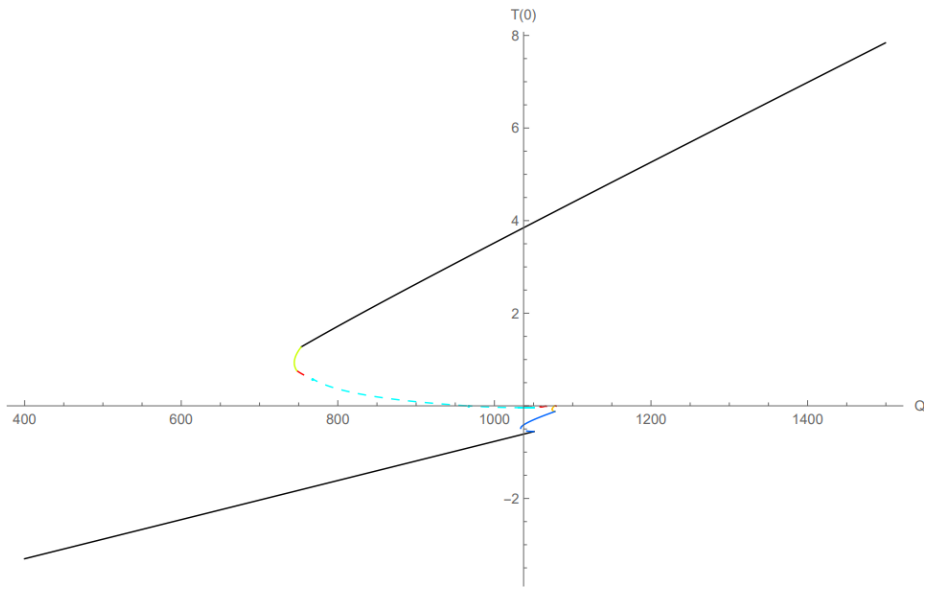


Figure 49: The bifurcation diagram for $\epsilon = 0.04$.

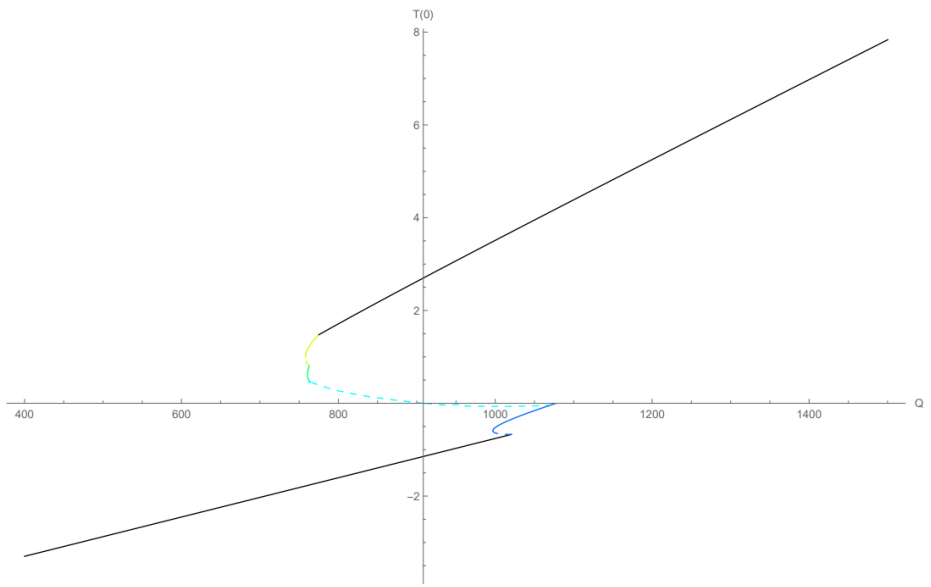


Figure 50: The bifurcation diagram for $\epsilon = 0.08$.

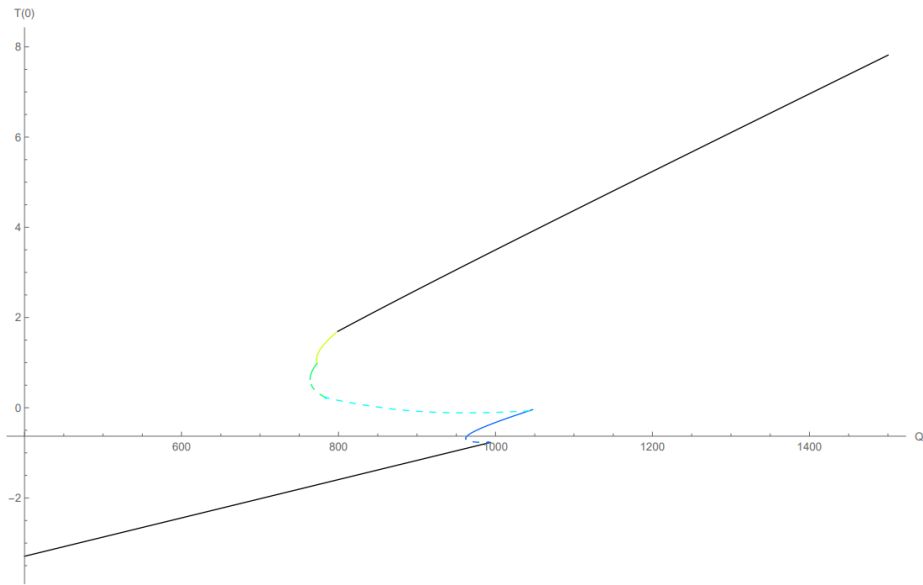


Figure 51: The bifurcation diagram for $\epsilon = 0.12$.

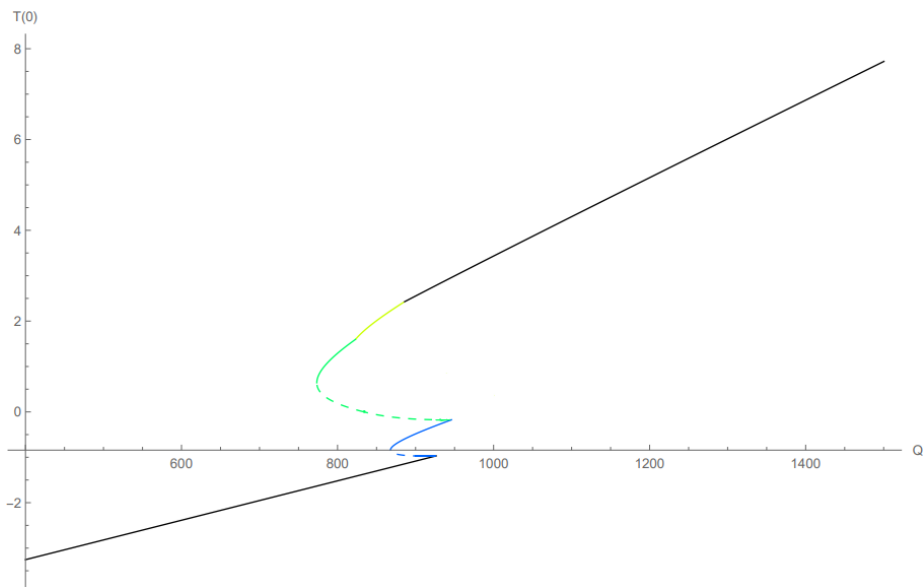


Figure 52: The bifurcation diagram for $\epsilon = 0.24$.

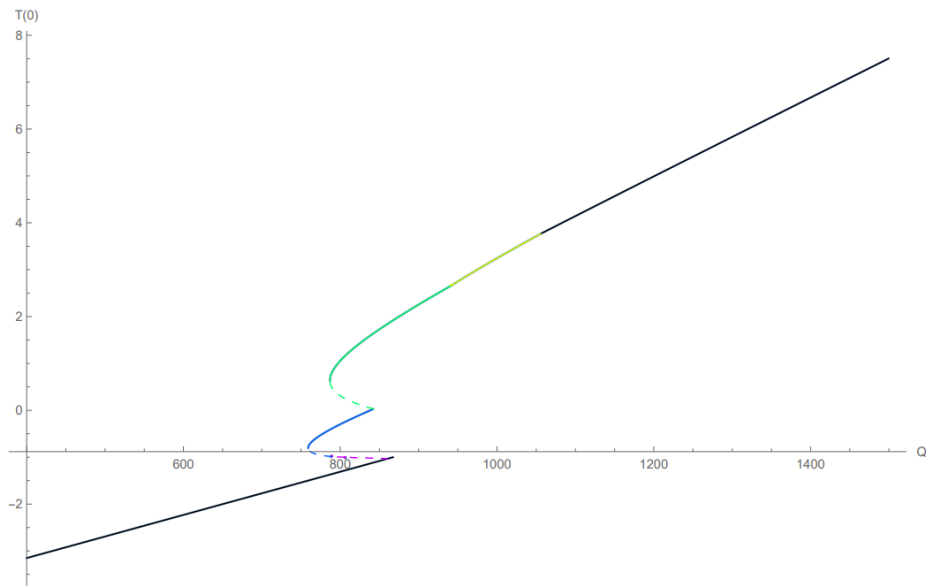


Figure 53: The bifurcation diagram for $\epsilon = 0.41$.

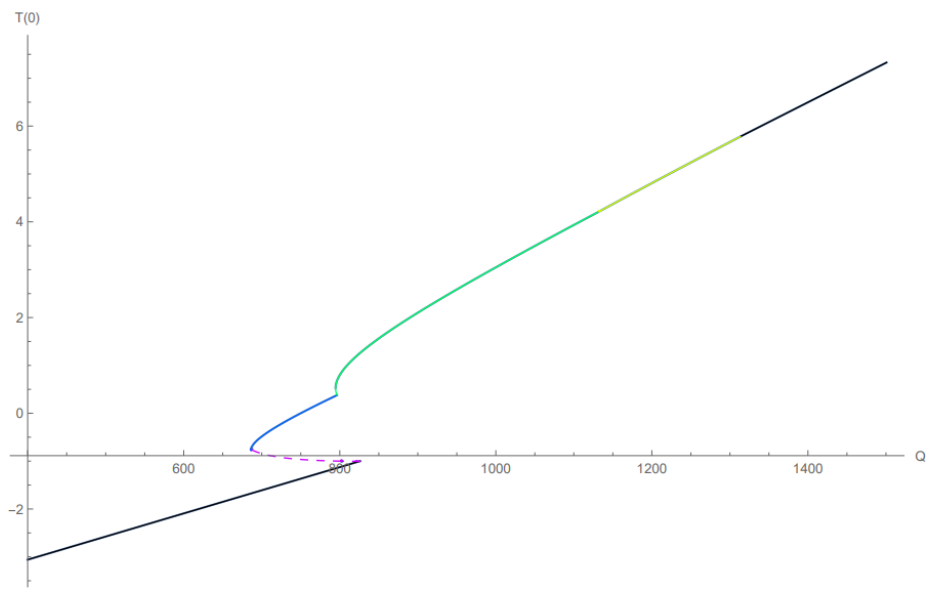


Figure 54: The bifurcation diagram for $\epsilon = 0.59$.

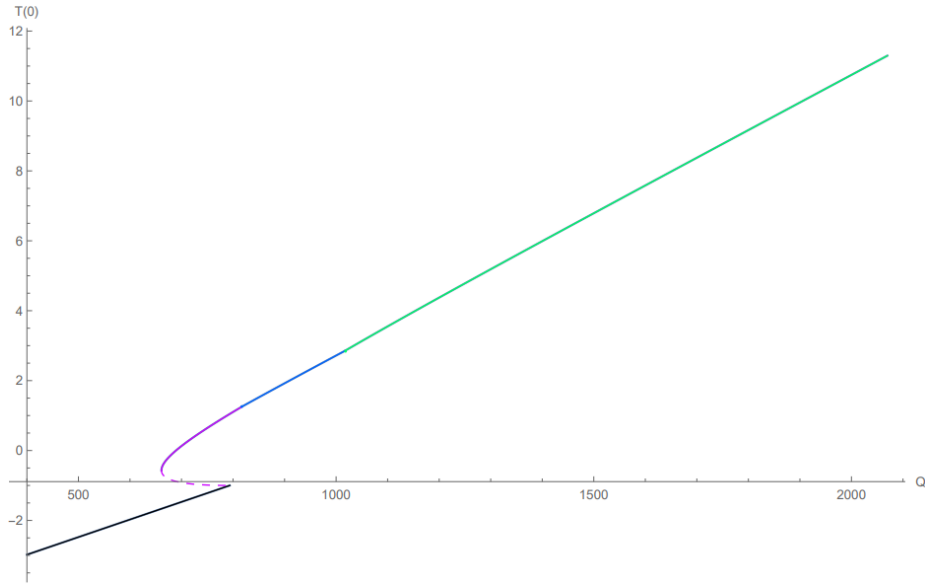


Figure 55: The bifurcation diagram for $\epsilon = 1.2$.

A.4 Multiple snow zones distribution

We considered the case of a symmetric continent with radiation distribution function (171) with $c = 1/10$, and a continent size $l = 1$. A collection of plots of where the snow edges are situated in relation to each other, and the lengths of the land and snow intervals, for the situations of multiple snow zones is presented in this section. figures 56, 57, 58, 59 and 61 show the cases of 2-4 snow edges for the values of Q where a solution exists. We denote the snow edges $\theta_{s0}, \theta_{s1}, \dots$, on the upper half circle.

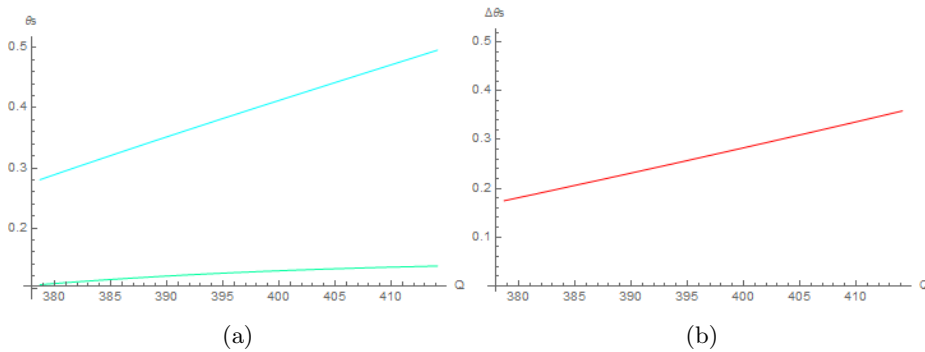


Figure 56: The angles $\theta_{s0}, \theta_{s1}, \dots$, in blues, and the differences $\theta_{s1} - \theta_{s0}, \dots$, in reds, for LSLWI.

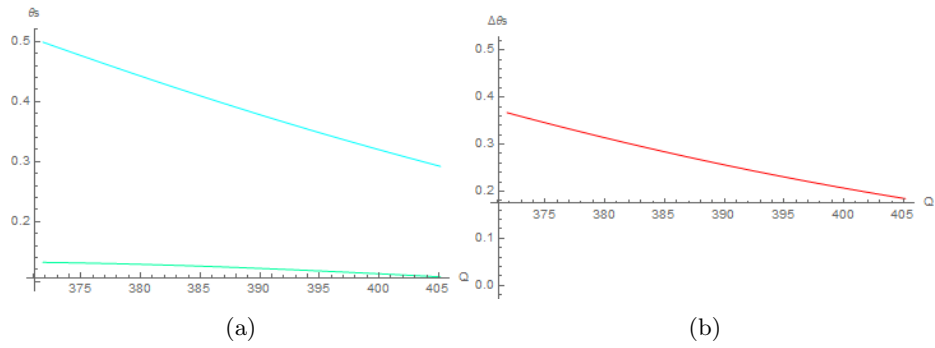


Figure 57: The angles $\theta_{s0}, \theta_{s1}, \dots$, in blues, and the differences $\theta_{s1} - \theta_{s0}, \dots$, in reds, for SLSWI.

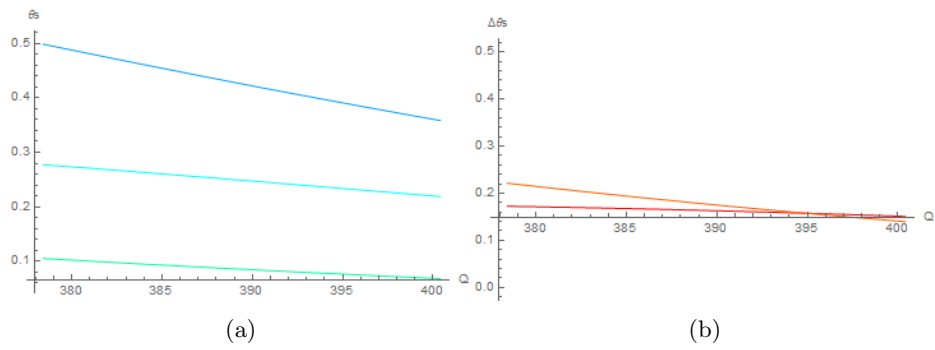


Figure 58: The angles $\theta_{s0}, \theta_{s1}, \dots$, in blues, and the differences $\theta_{s1} - \theta_{s0}, \dots$, in reds, for LLSWI.

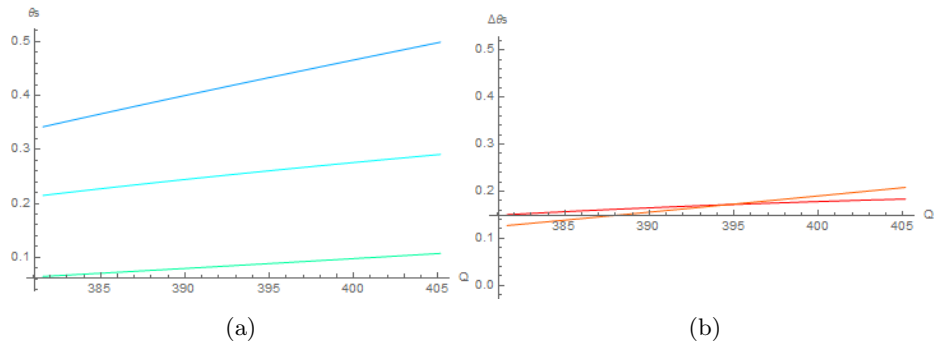


Figure 59: The angles $\theta_{s0}, \theta_{s1}, \dots$, in blues, and the differences $\theta_{s1} - \theta_{s0}, \dots$, in reds, for SLSLWI.

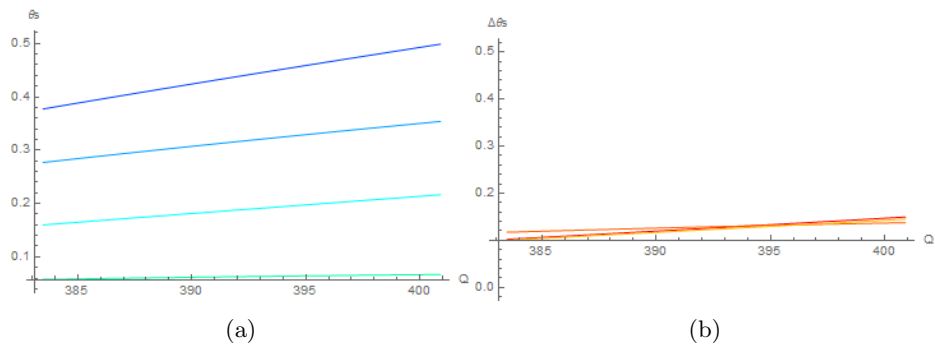


Figure 60: The angles $\theta_{s0}, \theta_{s1}, \dots$, in blues, and the differences $\theta_{s1} - \theta_{s0}, \dots$, in reds, for LSLSLWI.

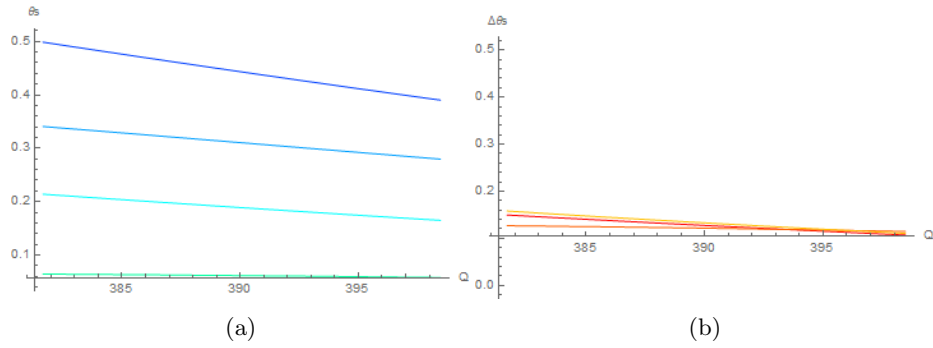


Figure 61: The angles $\theta_{s0}, \theta_{s1}, \dots$, in blues, and the differences $\theta_{s1} - \theta_{s0}, \dots$, in reds, for SLSLWI.

A.5 Multiple snow zones temperature distributions

A selection of temperature distributions for the case of a symmetric continent with radiation distribution function (171) with $c = 1/10$ and a continent size $l = 1$, is shown in figures 62, 70. The solar constant is set to $Q \approx 390$. Colour coding follows table 3.

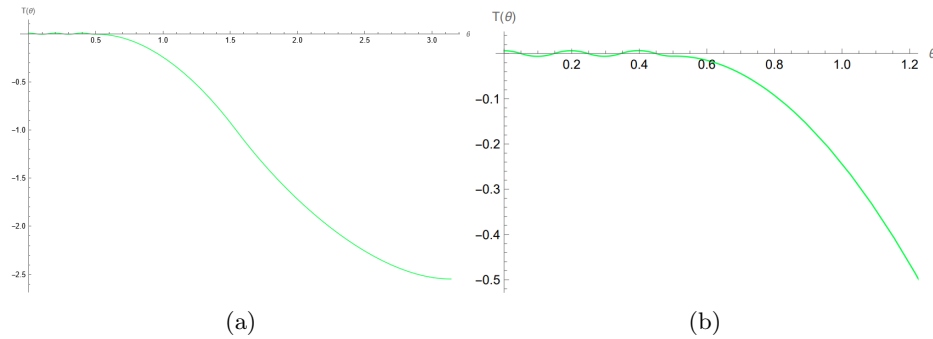


Figure 62: The LSLSLWI temperature distribution.

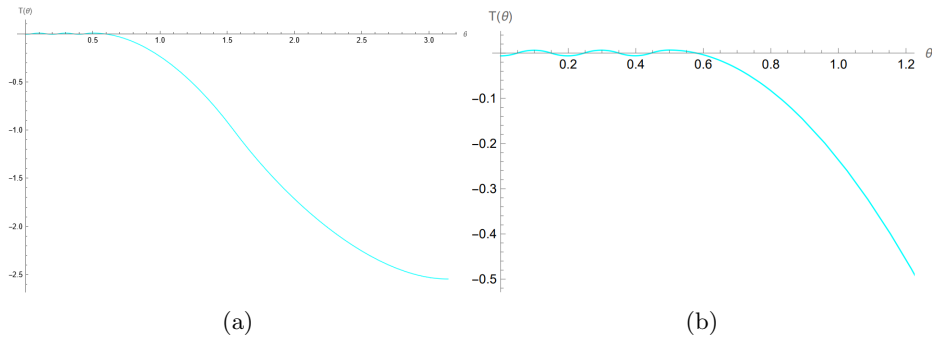


Figure 63: The SLSLWI temperature distribution.

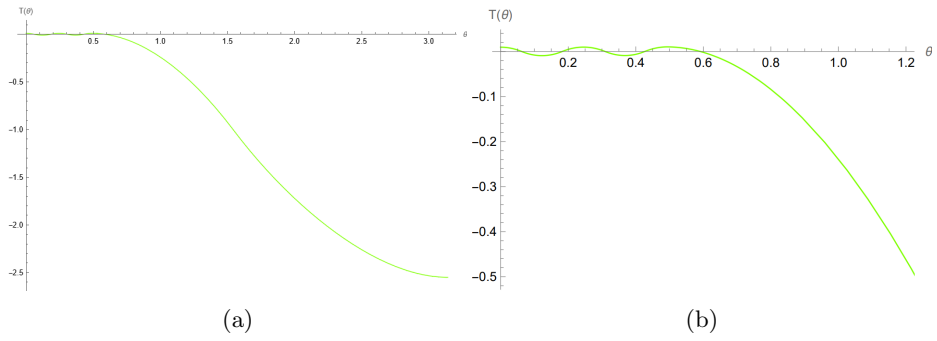


Figure 64: The LSLSLWI temperature distribution.

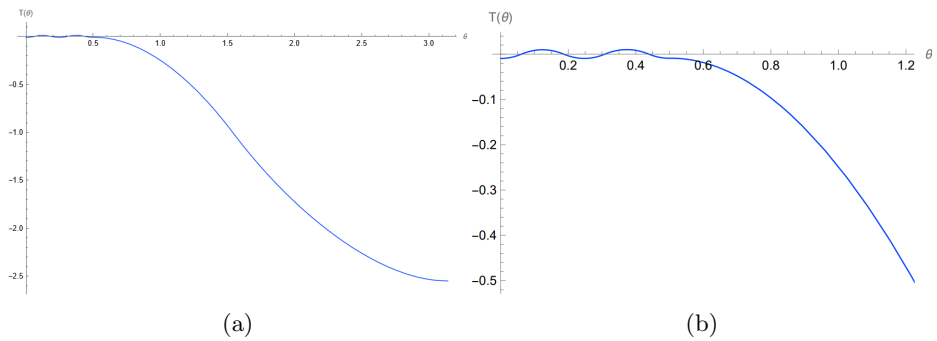


Figure 65: The SLSLWI temperature distribution.

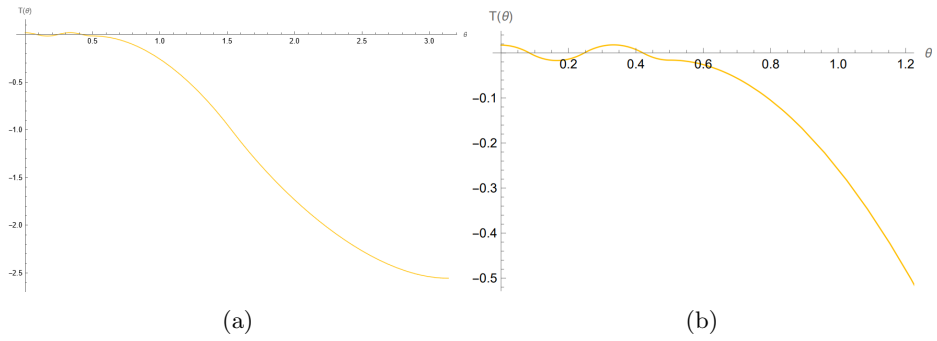


Figure 66: The LSLSWI temperature distribution.

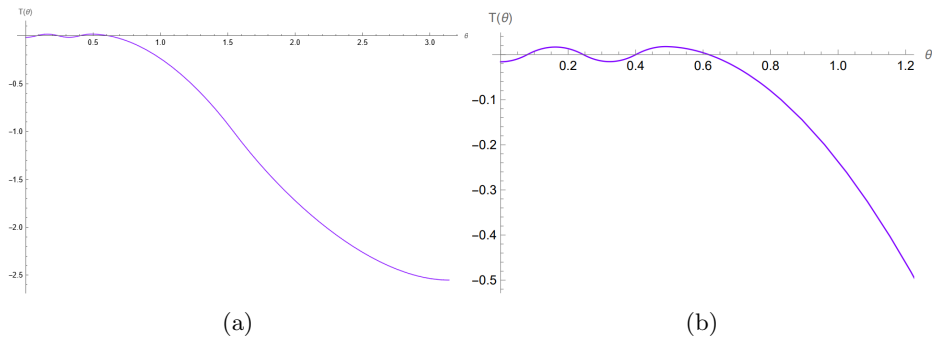


Figure 67: The SLSLWI temperature distribution.

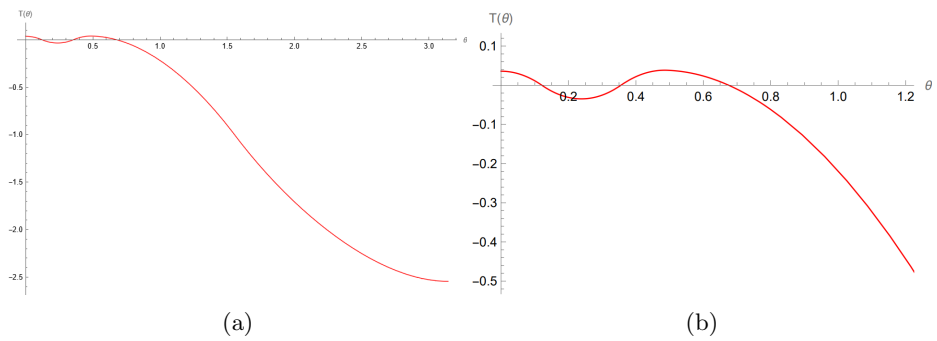


Figure 68: The LSLWI temperature distribution.

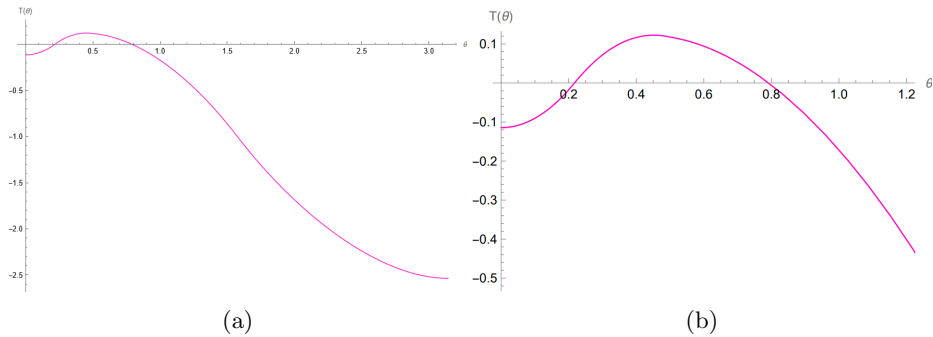


Figure 69: The SLSWI temperature distribution.

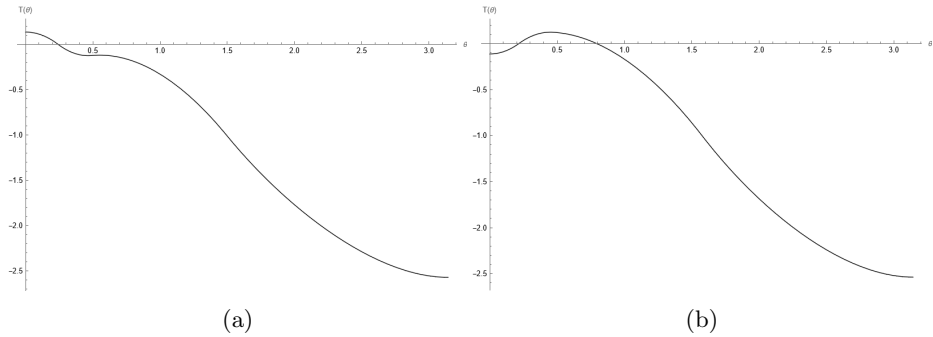


Figure 70: (a) The LSWI temperature distribution. (b) The SLWI temperature distribution.

A.6 Installation and basic use guide for AUTO-07p on Windows

To successfully set up AUTO-07p on your Windows computer you must in addition to the program itself install an Unix-like environment to run AUTO, and you should have a version of *Python* of at least version 2.3. It is also strongly recommended to install *NumPy* and *Matplotlib*.

A.6.1 Unix-like environment MSYS

The recommended environment to run AUTO is *MSYS2*, which can be downloaded from <https://www.msys2.org>. After installing using the wizard defaults, start *MSYS2* using *MinGW 64bit*. Update the package database and base packages by running

```
pacman -Syu,
```

then, start *MSYS MSYS* from the start menu and run again

```
pacman -Syu.
```

Now, install at least the the packages

- gcc-fortran
- mingw-w64-x86_64-python-matplotlib
- make

by using `pacman -S <name>`. Now we proceed with setting up AUTO.

A.6.2 AUTO file configuration

The AUTO file `auto-07p-master.zip` is available via <https://github.com/auto-07p/auto-07p>.

When unzipped, rename the folder `07p`, and wrap it in another folder `auto`. This is to conform with AUTOs expected file tree. Then place this folder named `auto` under in the directory `MSYS/home/username`, where *username* is your username. (can also be unzipped with `gunzip` in `MSYS`, after placing in `username` folder). Now you should be able to run `configure` and `make` to compile AUTO. In *MinGW 64bit*, move from `home` to the sub-directory of `auto/07p` by using the command

```
cd auto/07p,
```

then type

```
./configure,
```

which checks your system for required compilers and libraries. When finished, type

```
make
```

to compile AUTO and its ancillary software. After compilation, you may type

```
make clean
```

to remove unnecessary files.

A.6.3 File manipulation

AUTO is still not completely ready for use, although this is the end of the manual. The files require a bit of tinkering to work on a windows computer. In the home directory, which you can reach by typing

```
cd ../../ or cd $HOME,
```

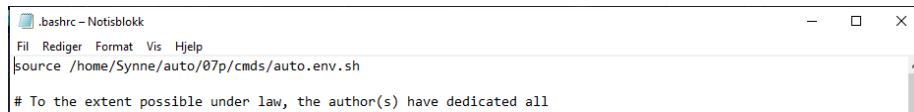
create a hidden file named `.bashrc` by typing the command `touch`

```
touch .bashrc,
```

which is an empty file where you will write (using Notepad, ect.) the string:

```
source /home/username/auto/07p/cmds/auto.env.sh
```

(instead of *username*, you will write your specific user name. If there are spaces, you could be in trouble.) Note that a file `.bashrc` may already exist. In that case, you can just type the string in this file.



```
.bashrc - Notisblokk
Fil Rediger Format Vis Hjelp
source /home/Synne/auto/07p/cmds/auto.env.sh
# To the extent possible under law, the author(s) have dedicated all
```

Figure 71: The file *.bashrc* edited.

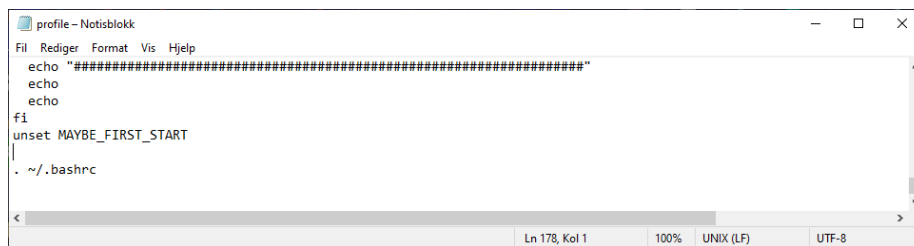
Under the Windows environment, edit the file named *profile* which is in the folder:

`C:\msys64\ect`

adding the following string at the end of the file

`. ~/.bashrc`

This allows the *.bashrc* file to be correctly invoked.



```
profile - Notisblokk
Fil Rediger Format Vis Hjelp
echo "#####"
echo
echo
fi
unset MAYBE_FIRST_START
|
. ~/.bashrc
Ln 178, Kol 1 100% UNIX (LF) UTF-8
```

Figure 72: The file *profile* edited.

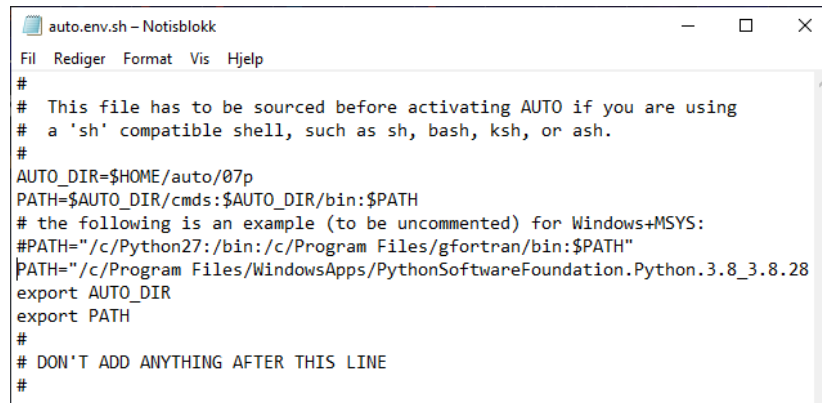
Now we will be editing the AUTO source file. Under Windows, in the directory:

`C:\msys64\home\username\auto\07p\cmds`

edit the file *auto.env.sh*. You should un-comment line 9 (i.e. remove the character ‘#’ at the beginning of the row). The line gives the path to python on your computer, edit it so it is correct. For the case of installation via Windows store it will look like

```
PATH="/c/Program Files/WindowsApps/PythonSoftwareFoundation.
Python.3.8_3.8.2800.0_x64__qbz5n2kfra8p0/python3.8:/
bin:/c/Program Files/gfortran/bin:$PATH"
```

The file should look something like this



```
auto.env.sh - Notisblokk
Fil Rediger Format Vis Hjelp
#
# This file has to be sourced before activating AUTO if you are using
# a 'sh' compatible shell, such as sh, bash, ksh, or ash.
#
AUTO_DIR=$HOME/auto/07p
PATH=$AUTO_DIR/cmds:$AUTO_DIR/bin:$PATH
# the following is an example (to be uncommented) for Windows+MSYS:
#PATH="/c/Python27:/bin:/c/Program Files/gfortran/bin:$PATH"
PATH="/c/Program Files/WindowsApps/PythonSoftwareFoundation.Python.3.8_3.8.28
export AUTO_DIR
export PATH
#
# DON'T ADD ANYTHING AFTER THIS LINE
#
```

Figure 73: The file *auto.env.sh* edited.

The set-up is now finished, and if you are lucky, AUTO should run just fine. You should exit from the MinGW-Shell in order to reboot the environment variables. You can do that by typing:

```
exit
```

You can test if it worked by trying to run one of the AUTO demos.

A.6.4 Running AUTO

AUTO can be run from *MSYS2* using *MinGW 64bit*. You can either type just `auto`

to enter the AUTO command line user interface (CLUI), or

```
auto name.auto
```

to run an auto file with name *name*. Running

```
auto clean.auto
```

cleans the directory of output files, if the directory you are working in contains this auto file. Every demo has a clean file, and an auto file with the demo name. The file runs a python script that can instruct auto to run the given problem one or several times, and change parameters between runs, ect. This will be illustrated by running a demo file.

Assuming that you are in your home directory, type:

```
cd auto/07p/demos/ab
```

to access the demo *ab*. To run the auto file, containing instructions for auto on runs to perform, you type

```
auto ab.auto
```

When the run is finished, the easiest way to plot the result is to just enter AUTO CLUI, by typing `auto`, and then in the CLUI giving the command

```
plot('ab')
```

This should give you what is shown in figure [74](#).

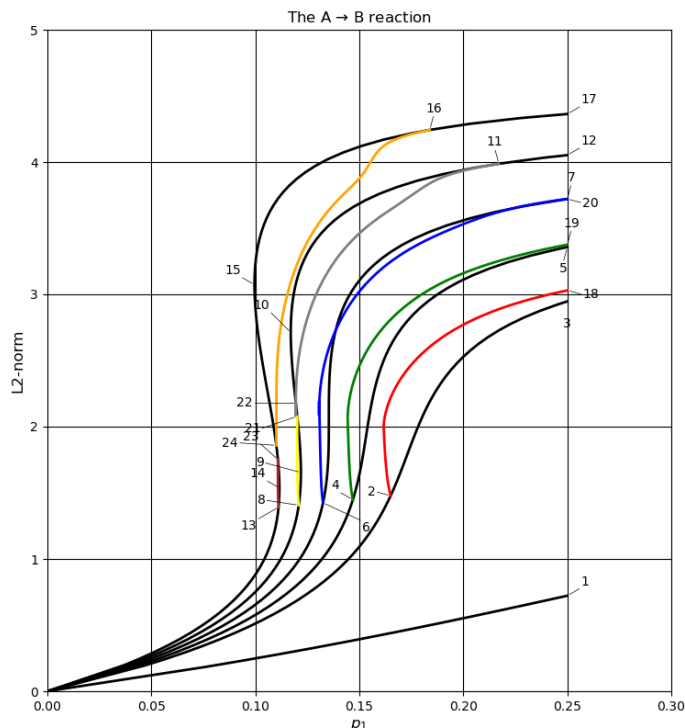


Figure 74: The result of AUTOs ab demo.

To start using AUTO on your own problem the easiest way is to copy an appropriate demo file, and change it as required. You need to supply the equations file `name.f90`, which defines the problem, and the constants file `c.name`, which gives the parameters. You can supply your own equations file `name.c` written in C if you prefer, an example in c can be found in the python demo file `python/n-body/3d.c`. But if you are equally unfamiliar with the languages you'll have an easier time learning a little free-form Fortran (`.f90`), as most demos use this.

In the `name.f90` file the most important component is the FUNC subroutine, where $F(i)$ gives the derivative of variable i . Figure 75 shows the `ab` demo FUNC. The ordinary differential equations for the problem are

$$\begin{aligned} u_1' &= -u_1 + p_1(1 - u_1)e^{u_2}, \\ u_2' &= -u_2 + p_1p_2(1 - u_1)e^{u_2} - p_3u_2. \end{aligned} \quad (197)$$

So you write $F(1) = u_1'$ and $F(2) = u_2'$. Something important to remember in Fortran is to give the type of every variable you define, generally as *integer* or *double precision*.

```

      SUBROUTINE FUNC(NDIM,U,ICP,PAR,IJAC,F,DFDU,DFDP)
! -----
! Evaluates the algebraic equations or ODE right hand side
! Input arguments :
!   NDIM   : Dimension of the ODE system
!   U      : State variables
!   ICP    : Array indicating the free parameter(s)
!   PAR    : Equation parameters
! Values to be returned :
!   F      : ODE right hand side values
! Normally unused Jacobian arguments : IJAC, DFDU, DFDP (see manual)
      IMPLICIT NONE
      INTEGER NDIM, IJAC, ICP(*)
      DOUBLE PRECISION U(NDIM), PAR(*), F(NDIM), DFDU(*), DFDP(*)
      DOUBLE PRECISION U1,U2,E
      U1=U(1)
      U2=U(2)
      E=EXP(U2)
      F(1)=-U1 + PAR(1)*(1-U1)*E
      F(2)=-U2 + PAR(1)*PAR(2)*(1-U1)*E - PAR(3)*U2
      END SUBROUTINE FUNC

```

Figure 75: FUNC subroutine in the *ab* demo.

The second component you will always have to include is the STPNT subroutine. This is where you initialize the solution. You give an initial solution for the ODE, and define the parameters. Figure 76 shows the *ab* demo STPNT. You can name the parameters, like variables, but it will only be defined in the subroutine. The $PAR(i)$ definition is global. $U(i)$ in the *ab* demo gives the initial solution

$$\begin{aligned}
 u_1 &= 0, \\
 u_2 &= 0.
 \end{aligned}
 \tag{198}$$

It is **VERY important** to give a good approximation of a solution, preferably analytic, if you want AUTO to find the continuation. AUTO can be particular about it. The parameters can be set or be allowed to vary. This is done in the constants file. Figure 77 shows the file for the *ab* demo. ICP is a list of parameters that are allowed to vary. In demo *ab* this is $PAR(2)$, initially set to be $PAR(2) = 8.$

In order to set a limit to values you want it to take, you can use $UZSTOP$. In the demo file we can see the computation is set to stop if the parameter reaches the value $PAR(2) = 18.0$.

You must also tell AUTO how many parameters the problem has, using $NPAR$.

```

      SUBROUTINE STPNT(NDIM,U,PAR,T)
! -----

! Input arguments :
!   NDIM   :   Dimension of the ODE system

! Values to be returned :
!   U      :   A starting solution vector
!   PAR    :   The corresponding equation-parameter values
!   T      :   Not used here

      IMPLICIT NONE
      INTEGER NDIM
      DOUBLE PRECISION U(NDIM), PAR(*), T

! Initialize the equation parameters
      PAR(1)=0.
      PAR(2)=8.
      PAR(3)=3.

! Initialize the solution
      U(1)=0.
      U(2)=0.

      END SUBROUTINE STPNT

```

Figure 76: STPNT subroutine in the *ab* demo.

```

c.ab.1 - Notisblokk
Fil Rediger Format Vis Hjelp
NDIM= 2, IPS = 1, IRS = 0, ILP = 1
ICP = [2]
NTST= 50, NCOL= 4, IAD = 3, ISP = 1, ISW = 1, IPLT= 0, NBC= 0, NINT= 0
NMX= 200, NPR= 200, MXBF= 10, IID = 2, ITMX= 8, ITNW= 5, NWTN= 3, JAC= 0
EPSL= 1e-07, EPSU = 1e-07, EPSS = 1e-05
DS = 0.1, DSMIN= 0.001, DSMAX= 0.2, IADS= 1
NPAR= 3, THL = {11: 0.0}, THU = {}
UZR = {2: [14.0, 15.0, 16.0, 17.0]}
UZSTOP={2: 18.0}

```

Figure 77: The constants file for the *ab* demo.

AUTO uses pseudo-arclength continuation for following solution families. The pseudo-arclength stepsize (DS) is the distance between the current solution and the next solution on a family. This is the parameter that controls computation the most, and you will need to experiment with it to find the best setting for your problem. DS gives the step size, but if $IADS > 0$ AUTO is set to adapt the pseudo-arclength stepsize after every $IADS$ steps. Then $DSMIN$ and $DSMAX$ controls the range DS may take. It is **important** to remember that if DS is too large, AUTO might not find the branching points/folds. But, the smaller the DS , the longer the computation will take. Other important parameters are as follows.

$NDIM$ gives the dimension of the ODE, for *ab* it is 2.

IPS gives the type of problem AUTO should solve. $IPS = 1$ is stationary solutions of ODEs with detection of Hopf bifurcations, including stability analysis. *NTST* and *NCOL* controls the time discretization AUTO does automatically. *NMX* gives the maximum number of steps to be taken along any family, and can cut the computation just like the limit on the parameter *UZSTOP*.

The last thing we will touch on, is the `name.auto` file. You can do separate runs and merge them to one data set, most easily using an auto file with directions.

```
print "\n***Compute stationary solution families***"
ab =run(e='ab',c='ab.1')

print "\n***Compute stationary solution families***"
ab = ab + run(ab("MX1"),c='ab.2')
```

Figure 78: The auto file with a split run.

You could do two different runs *ab1* with one constant file, *ab2* with another, and put them together $ab = ab1 + ab2$. For instance in positive and negative direction of some starting value ($DS > 0$, $DS < 0$). You can also, as shown in figure [78](#), run until AUTO stops, either by reaching maximum number of iterations *NMX* or stopping by *UZSTOP*, and continuing from that point with different parameters.

If the stopping cause is *NMX*, you start from equation $e = ab("MX1")$. The number 1 giving the run number.

If the stopping cause is *UZSTOP*, you start from equation $e = ab("UZ1")$. This will let you save on computation time, by having a smaller DS up to a certain point for instance.

For more detailed and in depth overview of commands and functions, please consult the AUTO manual.

References

- [1] M. I. Budyko. *The effect of solar radiation variations on the climate of the earth*. Tellus XXI, 21:5:611–619, 1969.
- [2] W. D. Sellers. *A global climate model based on the energy balance of the earth-atmosphere system*. Journal of applied meteorology, 8:392–400, 1969.
- [3] Gerald R. North. *Analytical solution to a simple climate model with diffusive heat transport*. Journal of the atmospherical sciences, 32(7):1301–1307, 1975.
- [4] Gerald R. North. *Theory of energy-balance models*. Journal of the atmospherical sciences, 32(11):2033–2043, 1975.

- [5] Per Kristen Jakobsen. *1d energy balance model for a tidally locked exoplanet*. Technical report, Department of Mathematics and Statistics, The Arctic University of Norway, 2021.
- [6] Per Kristen Jakobsen. *The energy balance model on a spherical planet; the north model*. Technical report, Department of Mathematics and Statistics, The Arctic University of Norway, 2021.
- [7] Per Kristen Jakobsen. *Energy balance models and their boundary formulations*. Technical report, Department of Mathematics and Statistics, The Arctic University of Norway, 2021.
- [8] Per Kristen Jakobsen. *An introduction to greens functions and boundary formulations*. Technical report, Department of Mathematics and Statistics, The Arctic University of Norway, 2021.
- [9] Jade Checlair with Kristen Menou and Dorian S. Abbot. *NO SNOWBALL ON HABITABLE TIDALLY LOCKED PLANETS*. arXiv:1705.08904v2 [astro-ph.EP], 2017.
- [10] Cameron R. Taylor. Finite difference coefficients calculator. <https://web.media.mit.edu/~crtaylor/calculator.html>, 2016.

